W boson physics at hadron colliders

Randy M. Thurman-Keup
Argonne National Laboratory, Argonne, Illinois 60439

Ashutosh V. Kotwal
Duke University, Durham, North Carolina 27708

Monica Tecchio
University of Michigan, Ann Arbor, Michigan 48109

Aesook Byon-Wagner
Fermi National Accelerator Laboratory, Batavia, Illinois 60510

(Published 12 April 2001)

The use of hadron colliders to investigate the properties of the W bosons started in 1982 at the CERN $Sp\overline{p}S$ collider. Since then, the Tevatron experiments at Fermilab have recorded a large sample of W events which allowed precision measurements of the properties of W bosons. In this paper the authors review W gauge boson physics at hadron colliders from 1982 to 2000. They first discuss the production mechanism and detection of W bosons in $p\overline{p}$ collisions. After a brief review of the early studies, W boson physics at the Tevatron collider are thoroughly examined. Finally, possible future directions of W boson physics at hadron colliders are discussed.

CONTENTS

I. Introduction 267
A. Role of the W boson in electroweak physics 268
B. Role of the W boson in quantum chromodynamics 270
C. Role of the W boson in nonstandard-model physics 270
II. W Production in $p\overline{p}$ Collisions 271
A. W and Z boson production and decay 272
B. Underlying event 273
C. Modeling of W boson production 273
1. Event generation 273
2. Detector simulation 274
III. Detection of W Bosons in $p\overline{p}$ Collisions 275
A. Triggering of W boson events 276
B. Electron and photon detection 276
C. Muon detection 276
D. Neutrino detection 277
E. Jet detection 277
IV. Early Studies of the W Boson at Hadron Colliders 277
A. $Sp\overline{p}S$ experiments: UA1 and UA2 277
B. CDF at the Tevatron collider: 1985–1990 278
V. Properties of the W Boson 278
A. Mass 278
1. Mass measurement strategy 279
2. Electron response and resolution 279
3. Muon response and resolution 281
4. Recoil response and resolution 281
5. Production and decay dynamics 282
6. Backgrounds 282
7. Mass fit results and uncertainties 283
B. Width 285
1. Direct Γ_W measurement 285
C. Cross section 286
1. Electron measurement 287
2. Muon measurement 288
3. Extraction of $B(W\rightarrow l\nu)$ and $\Gamma(W)$ 289
4. τ measurement 289
D. Lepton charge asymmetry 289
E. Transverse momentum and jets 291
1. W and Z boson transverse momentum 291
2. Properties of W and Z boson+jet events 292
F. Heavy and right-handed W bosons 294
1. Search for heavy W' bosons 294
2. Search for right-handed W bosons 295
G. Rare decays 296
1. $W\rightarrow\pi\gamma$ 296
2. $W\rightarrow D_s\gamma$ 297
H. Trilinear gauge couplings 298
1. $W\gamma\rightarrow l\nu\gamma$ analysis 298
2. $WW\rightarrow l\nu l\nu$ analysis 300
3. $WW/WZ\rightarrow l\nu jj$ and $WZ\rightarrow jjl^+l^-$ analysis 300
4. $WZ\rightarrow l\nu l^+l^-$ analysis 300
5. DØ combined WWV analysis 301
VI. Future Prospects 301
A. W mass and width 302
B. W charge asymmetry and QCD studies 303
C. Rare W decays and heavy W' bosons 303
D. Anomalous vector-boson couplings 303
VII. Conclusions 304
Acknowledgments 304
References 304

I. INTRODUCTION

The massive charged $W^{\pm}$ and neutral Z^0 bosons were proposed in the 1960s as the mediators of the weak currents in the unified model of electromagnetic and weak interactions developed by Glashow (1961), Weinberg (1967), and Salam (1969). This model, now known as the ''standard'' model, reconciles under a unified theory the pure $V-A$ nature of the charged weak currents with the predominant $V-A$ nature of neutral weak currents by including the electromagnetic current and imposing

local gauge invariance under the $SU(2)_L \times U(1)_Y$ symmetry group. The requirement of local gauge invariance and its "spontaneous" breaking via the Higgs mechanism (Higgs, 1966) ensures that the theory remains renormalizable, i.e., it prevents the divergences in the high-energy limit that had plagued previous models of the weak currents ('t Hooft, 1971a, 1971b).

While the phenomenology of the charged weak currents was well established at the time, the neutral weak currents had not yet been observed. Their discovery in $\nu_\mu N \to \nu_\mu X$ scattering at the CERN Gargamelle bubble chamber in 1973 (Hasert *et al.*) was the first success of the standard model. But its most spectacular confirmation came with the discovery in 1983 of the W and Z bosons by the UA1 and UA2 experiments at the CERN $Sp\bar{p}S$ collider at the masses predicted from neutrino-scattering data and the muon lifetime. The 1990s saw increasingly precise experimental tests of the standard-model predictions. Studies at the Z resonance by the LEP and SLC detectors tested the theory of weak neutral currents to higher orders in perturbation theory (see Grünewald, 1999 for a recent review). In this paper we shall review the direct measurements of the properties of the W boson in charged weak interactions at the Tevatron $p\bar{p}$ collider.

A. Role of the *W* boson in electroweak physics

In the standard model (SM), the intermediate vector bosons arise as combinations of the isotriplet of vector fields $W_\mu^i (i=1,2,3)$ and the neutral vector field B_μ which couple to the weak current $\vec{J}^\mu = (J_1^\mu, J_2^\mu, J_3^\mu)$ and to the hypercharge current j_Y^μ, respectively. The two basic interactions of the electroweak Lagrangian are

$$-ig\vec{J}^\mu \cdot \vec{W}_\mu = -ig\bar{\chi}_L \gamma^\mu \vec{T} \cdot \vec{W}_\mu \chi_L ,$$
$$-ig' j_Y^\mu B_\mu = -ig' \bar{\psi} \gamma^\mu Y \psi, \tag{1}$$

where g and g' are the coupling constants, and $\vec{T}$ and Y are the generators of the $SU(2)_L$ and $U(1)_Y$ groups of gauge transformations. The γ^μ's are the Dirac matrices. The χ_L's are isospin doublets of left-handed fermions while the ψ's are isospin singlets. The electromagnetic interaction appears as the combination of two neutral currents $j_{em}^\mu = J_3^\mu + 1/2 j_Y^\mu$. With the introduction in the electroweak Lagrangian of a single Higgs field $\phi(x)$ as a complex scalar doublet of weak hypercharge $Y=1$, with vacuum expectation value $\phi_0 = \sqrt{1/2}\binom{0}{v}$, the gauge-field mass eigenstates become

$$W^\pm = \frac{1}{\sqrt{2}}(W_1^\mu + W_2^\mu), \quad M_W = \frac{gv}{2}$$
$$Z^0 = \cos\theta_W W_3^\mu - \sin\theta_W B^\mu, \quad M_Z = \frac{v(\sqrt{g^2+g'^2})}{2}$$
$$A^\mu = \sin\theta_W W_3^\mu + \cos\theta_W B^\mu, \quad m_\gamma = 0, \tag{2}$$

where θ_W is the weak angle. The weak angle relates the strengths of the weak interactions to the electromagnetic coupling e via

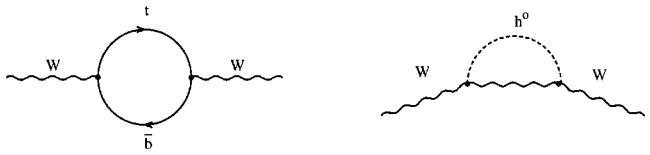

FIG. 1. Loop diagrams contributing radiative corrections to the W boson mass.

$$g \sin\theta_W = g' \cos\theta_W = e. \tag{3}$$

It also relates the masses of the charged and neutral weak bosons via

$$\cos\theta_W = \frac{M_W}{M_Z}, \tag{4}$$

which is a definite prediction of the SM given the particular "minimal" choice for the Higgs field.

Another prediction of the SM is that the $W^\pm$ boson has a single, universal coupling constant g to all leptons. This was true also of the G_F constant in the Fermi effective theory of electroweak interactions. The two constants are related by $g^2 = (8/\sqrt{2}) G_F M_W^2$. By inserting Eq. (3) into the above relation, one obtains the SM prediction for the W boson mass in terms of other model parameters:

$$M_W = \left(\frac{\pi\alpha}{\sqrt{2}G_F}\right)^{1/2} \frac{1}{\sin\theta_W \sqrt{1-\Delta r}}, \tag{5}$$

where $\alpha = e^2/4\pi$ and Δr parametrizes the effects of radiative corrections to the W propagator.

The W mass measurement provides a test of the standard model and a probe for new physics. We reproduce this discussion from Abbott *et al.* (1998c, 1998d). In the "on-shell" renormalization scheme (Marciano and Sirlin, 1980; Sirlin, 1980), which promotes the use of Eq. (4) for all orders in perturbation theory, the W mass can be computed at tree level from three precisely measured quantities: the mass[1] of the Z boson M_Z (Particle Data Group, 1998, p. 231), the Fermi constant G_F (Particle Data Group, 1998, p. 69), and the electromagnetic coupling constant α evaluated at $Q = M_Z$ (Particle Data Group, 1998):

$$M_Z = 91.1867 \pm 0.0020 \ \text{GeV},$$
$$G_F = (1.16639 \pm 0.00001) \times 10^{-5} \ \text{GeV}^{-2},$$
$$\alpha = (128.88 \pm 0.09)^{-1}. \tag{6}$$

From the measured W mass, one can derive the size of the radiative corrections Δr. The SM predicts the corrections arising from fermion loops and the Higgs boson loop (see Fig. 1). The correction due to fermion loops depends on the difference in the squared fermion masses, hence the correction from the $t\bar{b}$ loop dominates. Since m_t has been measured (Particle Data Group, 1998, p. 347), its contribution can be calculated within the SM. For a large Higgs mass, m_H, the correc-

[1]Throughout this paper we use $c=1$ and $\hbar=1$.

tion from the Higgs loop is proportional to the logarithm of m_H. A measurement of the W mass therefore constitutes a test of the SM. Together with a measurement of the top-quark mass, the SM predicts M_W within a range of 200 MeV depending on the assumed Higgs mass. By comparing the calculation to the measured value of the W mass, one can constrain the mass of the Higgs boson, which has not yet been detected experimentally.

A discrepancy with the range allowed by the SM could indicate new physics. The W mass is sensitive to the properties of new particles which can populate the loops in the W propagator. In the minimal supersymmetric extension of the standard model (MSSM), for example, additional corrections can increase the predicted W mass by up to 250 MeV (Chankowski *et al.*, 1994; Garcia and Sola, 1994; Dabelstein *et al.*, 1995; Pierce *et al.*, 1997). The experimental challenge is to measure the W mass to sufficient precision, about 0.05%, to be sensitive to these corrections. The CDF and DØ experiments at the Tevatron Collider have recently performed direct measurements of the W mass approaching this level of precision, as we shall see in Sec. V.A.

The W width Γ_W is predicted in the SM in terms of the mass and coupling of the W boson. Its value at hadron colliders is extracted from the ratio $\Gamma_W = \Gamma(W \to l\nu)/B(W \to l\nu)$ where $\Gamma(W \to l\nu)$ is the leptonic partial width and $B(W \to l\nu)$ the leptonic branching ratio ($l = e$ or μ). The former can be expressed in the SM as

$$\Gamma(W \to l\nu) = \frac{G_F M_W^3}{6\sqrt{2}\pi(1+\delta)}, \tag{7}$$

where δ is the electroweak radiative correction to the Born-level calculation and is less than 0.5%. The latter is

$$B(W \to l\nu) = \frac{1}{3 + 6[1 + \alpha_s(M_W)/\pi] + \mathcal{O}(\alpha_s^2)} \tag{8}$$

to first order in the strong-coupling constant α_s evaluated at the renormalization scale $Q = M_W$. The first term in the denominator is due to the three ($e\nu$, $\mu\nu$, and $\tau\nu$) leptonic decay modes, assuming lepton universality and ignoring small phase-space effects. The second term is due to the hadronic decay to the first two generations of quarks $u\bar{d}$ and $c\bar{s}$, with a quantum chromodynamic (QCD) color factor of 3 and the first-order QCD gluon radiative correction. From Eqs. (7) and (8), the SM numerical prediction for the total W width is $\Gamma_W = 2.093 \pm 0.002$ GeV. The consistency of early measurements of Γ_W with this SM prediction was used to prove that if the top quark was the weak isospin partner of the bottom quark, then the absence of the $W \to t\bar{b}$ partial width implied a lower limit on the top mass m_t.

The W width can also be determined indirectly by using the ratio

$$R \equiv \frac{\sigma_W \cdot B(W \to l\nu)}{\sigma_Z \cdot B(Z \to l^+ l^-)}, \tag{9}$$

where σ_W and σ_Z are the inclusive cross sections for W and Z production, and B are the respective leptonic

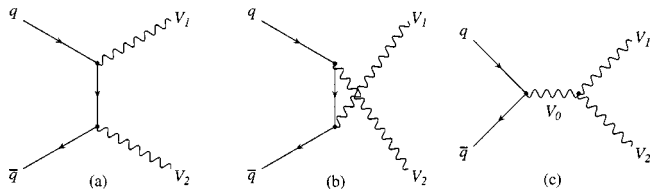

FIG. 2. Tree-level Feynman diagrams for vector-boson pair production: (a) t-channel diagram; (b) u-channel diagram; (c) s-channel diagram. For $W\gamma$ production $V_0 = V_1 = W$ and $V_2 = \gamma$. For WW production $V_0 = \gamma$ or Z, $V_1 = W^+$, and $V_2 = W^-$. For WZ production $V_0 = V_1 = W$ and $V_2 = Z$.

branching ratios. By measuring R, one can extract the branching ratio $B(W \to l\nu)$ as

$$B(W \to l\nu) = R \frac{\sigma_Z}{\sigma_W} B(Z \to l^+ l^-), \tag{10}$$

where σ_Z/σ_W can be calculated theoretically, and $B(Z \to l^+ l^-)$ has been measured precisely at LEP. The total W width is then derived by using the SM calculation of $\Gamma(W \to l\nu)$. Sections V.B and V.C will review the Tevatron results on Γ_W and the limits on the W partial width into new decay modes.

The measurements of $\sigma_W \cdot B(W \to \tau\nu)$ and $\sigma_W \cdot B(W \to e\nu)$ provide a test of lepton universality, since their ratio can be expressed as

$$\frac{\sigma_W \cdot B(W \to \tau\nu)}{\sigma_W \cdot B(W \to e\nu)} = \left(\frac{g_\tau}{g_e}\right)^2. \tag{11}$$

The universality of the leptonic couplings to the weak charged current is a direct consequence of the assumption that the leptons transform as $SU(2)_L$ doublets. While muons have also been used, tests involving the τ lepton are more interesting because of their larger mass.

Another important prediction of the SM, due to the non-Abelian character of the $SU(2)_L$ isospin symmetry group, is the existence of three- and four-vector boson vertices. Gauge invariance uniquely determines the structure of these W, Z, and γ boson self-coupling terms. In the SM, only $WW\gamma$ and WWZ vertices are predicted to be nonzero at tree level. The other possible triboson combinations, $ZZ\gamma$, $Z\gamma\gamma$, and ZZZ, are not allowed because the couplings of particles to the Z boson depend on their electric charge and weak isospin, both of which are zero for the neutral bosons. Studies at $p\bar{p}$ machines of $W\gamma$, WW, and WZ production rates and kinematical distributions provide a direct measurement of the trilinear W couplings via the s-channel W, γ, and Z exchange interactions (see Fig. 2). Even a small deviation of the trilinear couplings from their predicted values will affect the subtle cancellation among the three contributions of Fig. 2 that is needed to control the unitarity of the process.

In studying possible deviations from the SM predictions one assumes that the new physics manifests itself at an energy scale Λ not yet reached by present accelerators. New particles will affect the triboson vertices via loop-diagram contributions and can be studied by introducing an effective Lagrangian formalism which param-

etrizes the contributions of new physics via a set of unknown constants.

The most general effective Lagrangian for WWV couplings ($V=Z$ or γ) consistent with Lorentz invariance can be expressed in terms of 14 dimensionless coupling parameters (Hagiwara *et al.*, 1993), g_1^V, κ_V, λ_V, g_4^V, g_5^V, $\tilde{\kappa}_V$, and $\tilde{\lambda}_V$. After imposing *P, C*, and *CP* symmetry, only the g_1^V, κ_V, and λ_V parameters are nonzero. Furthermore $g_1^\gamma=1$ due to the gauge invariance of the electromagnetic interaction. To regain the SM Lagrangian, one must set $g_1^Z=1$, $\Delta\kappa_V\equiv\kappa_V-1=0$, and $\lambda_V=0$. Any deviation from these "effective" couplings will be an indication of anomalies in the WWV vertex, such as the case that the γ couples only to the electric charge of the W boson [called the minimal $U(1)_{EM}$ coupling]. For the present bounds from theoretical estimates of the coupling parameters see the review by Ellison and Wudka (1998).

The effective Lagrangian violates unitarity at energies approaching the scale of new physics, Λ. To avoid it, the anomalous couplings are modified by a form factor dependent on the scale Λ. A commonly used expression for such a form factor is $c(\hat{s})=c_0/(1+\hat{s}/\Lambda^2)^2$ where $\hat{s}$ is the squared center-of-mass energy of the scattering process and c_0 represents any of the deviations of the WWV coupling parameters from their SM values. This choice, unlike the rest of the effective Lagrangian formalism, is model dependent. Experimentally Λ is chosen to be close to the maximum value allowed by unitarity constraints. In Sec. V.H we present limits on anomalous couplings obtained by the CDF and DØ experiments at the Tevatron.

B. Role of the *W* boson in quantum chromodynamics

W bosons offer a way to study QCD through measurements of their production properties. Unlike quarks and gluons, *W* (and *Z*) bosons are colorless and do not hadronize. Thus their decays into leptons act as direct probes of the hard partonic processes. In addition, their large mass allows most of their production properties to be calculated perturbatively in QCD.

The total production cross section of *W* and *Z* bosons is typically expressed as the leading-order Born cross section times a multiplicative *K* factor. The *K* factor embodies the effect of next-to-leading-order QCD processes involving initial-state quark and gluon radiation [see Eq. (12)]. As discussed in Sec. V.C, comparisons of measurements with calculations show good agreement.

The p_T spectrum of the bosons can be calculated reliably at high p_T using perturbative QCD. At low boson p_T, resummation and nonperturbative techniques are needed to adequately describe the data, as discussed in Sec. II.A. The value of the strong-coupling constant α_s enters the calculation of the number of jets produced in *W* and *Z* events. Next-to-leading-order QCD predictions (Giele *et al.*, 1993) for *W* plus ≥ 0 jet or ≥ 1 jet allow a parametrization of the cross section as $\alpha_s^n(A_n+\alpha_s B_n)$ where *n* is 0 or 1. By using the ratio of these cross sections, one can cancel many uncertainties in the experimental measurements and theoretical predictions. The data can be compared to the predictions for different values of the renormalization scale. The colorless nature of the gauge bosons can be exploited to study QCD color coherence in $W+$jet events. These measurements are discussed in Sec. V.E.

Another approach to studying QCD is to use the angular distributions of the jets in *W* or *Z* events. In $W+1$ jet events, where the production matrix elements are dominated by quark propagators, the *W* boson or the jet is expected to have a polar angle distribution of $dN/d\cos\theta^* \sim (1-|\cos\theta^*|)^{-1}$ due to the spin-1/2 propagator. In comparison, in gluon-propagated dijet events, the integral spin of the gluon results in an inverse-square dependence of the angular distribution.

Nonperturbative QCD in the form of the parton distribution functions can also be studied. The parton distribution functions are probability densities for a given parton to be carrying a given fraction of the proton's momentum. They are measured mostly from deep-inelastic scattering, Drell-Yan and direct photon measurements, with an important contribution from the *W* charge asymmetry measurement (see Sec. V.D). Every process that occurs at a hadron collider is subject to the influence of the parton distribution functions. The uncertainties in these distribution functions affect every analysis and, in the case of the measurement of the *W* mass, play a significant role in the total uncertainty. Since the rapidity distribution of the *W* boson is sensitive to the product of the quark and antiquark distribution functions, a measurement of *W* rapidity helps to constrain them, in particular the ratio of the *d* quark to *u* quark distributions, d/u (Berger *et al.*, 1989; Martin *et al.*, 1989), in a complementary fashion to deep-inelastic scattering and Drell-Yan measurements. Unfortunately, one cannot reliably reconstruct the rapidity of the *W* because of the presence of the neutrino in the decay. The experimental observable used is the lepton forward-backward charge asymmetry, usually just referred to as the *W* charge asymmetry, which is a convolution of the true *W* forward-backward charge asymmetry and the forward-backward charge asymmetry of the $V-A$ leptonic decay of the *W* boson. The latter is understood very well from muon decay experiments. Figure 3 shows the lepton forward-backward charge asymmetry, and the contribution from just the *W* forward-backward asymmetry, versus the *W* rapidity $|y|$. The two asymmetry contributions (*W* and $V-A$ decay) are of opposite sign. The $V-A$ asymmetry is small at low rapidity but increases with *y* and tends to cancel the *W* asymmetry at the highest values of rapidity accessible to the detector. The measurement of the *W* asymmetry is described in Sec. V.D.

C. Role of the *W* boson in nonstandard-model physics

Measurements of the *W* and *Z* production properties provide a means of searching for new heavy particles decaying to these bosons. For instance, if a new heavy particle were to decay to a *W* or *Z* boson and anything

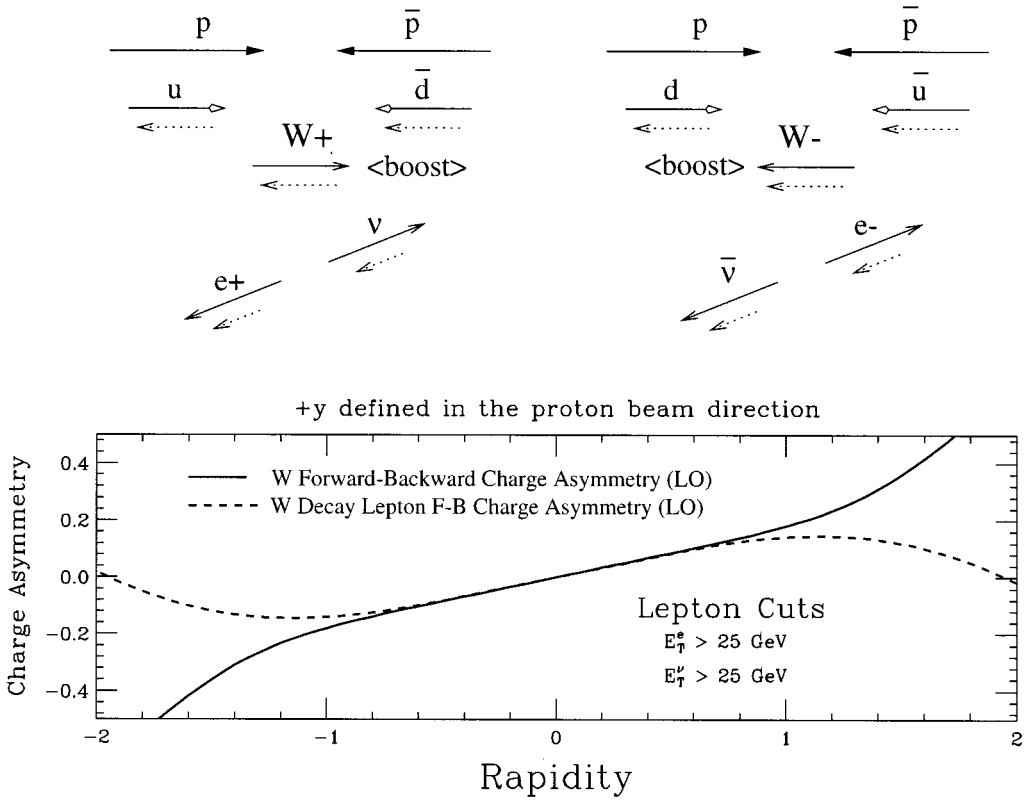

FIG. 3. *W* boson charge asymmetry: top, lowest-order production diagram for the kinematics of *W* production showing components relevant to the *W* forward-backward asymmetry measurement. The solid lines indicate momentum flow and the dashed lines indicate spin. The parton distribution functions cause the $W^+(W^-)$ to be boosted in the direction of the $p(\overline{p})$. Bottom, solid curve, the true *W* asymmetry; dashed curve, the sum of *W* and $V-A$ asymmetries.

else, the boson p_T distribution would show an excess above the QCD prediction. *W* and *Z* have similar production dynamics but different decay modes, so they provide complementary measurements. Other studies, for example, of production of $W/Z+$jets, are important in understanding the backgrounds in Higgs searches or other new physics processes.

Section V.F will report on direct searches for additional heavy gauge bosons, which arise in extensions of the SM aimed at restoring the left-right symmetry of the electroweak Lagrangian (Mohapatra, 1992). Such models replace the $SU(2)_L\times U(1)_Y$ symmetry group with an extended $SU(2)_R\times SU(2)_L\times U(1)_Y$, thus introducing two new charged $W_R^{\pm}$ and one neutral Z' gauge bosons along with massive right-handed neutrinos ν_R. The decay of a right-handed W_R into WZ will be suppressed by the left-right mixing angle $\xi\sim(M_W/M_{W_R})^2$ (Ramond, 1983). If the W_R is heavy enough, its decay into right-handed $l_R\nu_R$ pairs is dominant. The coupling of the W_R to fermions is not known. But in models with manifest left-right symmetry the strength of the coupling of the right-handed bosons to left- and right-handed fermions is the same and equal to the SM values. This is also referred to as the "standard coupling" scenario.

The study of rare *W* decays also provides a window on new physics. Physics beyond the SM often brings with it the existence of new particles that, while too heavy to be observed as real particles, appear as virtual particles in lower-energy processes, thus altering cross sections and decay rates. In searches for rare *W* decays at the Tevatron, one concentrates on easily identifiable low-background final states and looks for the enhancement of decay rates to observable levels well above those predicted by the SM. The present status of these searches is reviewed in Sec. V.G.

II. *W* PRODUCTION IN $p\bar{p}$ COLLISIONS

In $p\overline{p}$ collisions at the energy of the S$p\overline{p}$S or the Tevatron collider, *W* and *Z* boson production requires fairly large values of the parton momentum fraction. Hence they are produced mainly through quark-antiquark annihilation. Figure 4 shows the lowest-order diagrams.

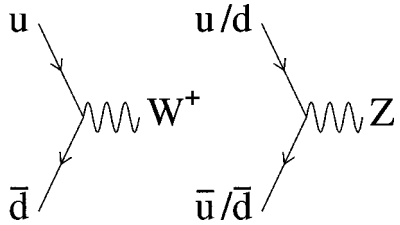

FIG. 4. Lowest-order production diagrams for *W* and *Z* bosons in a hadron-hadron collision.

A. *W* and *Z* boson production and decay

Due to the large mass of the W and Z bosons, QCD factorization can be employed to calculate their production cross sections in hadron collisions. The lowest-order cross section can be written as

$$\frac{d^2\sigma}{dp_T^2 dy} \propto \sum_{q,\bar{q}} \int dx_q \int dx_{\bar{q}} f_q(x_q,\hat{s}) f_{\bar{q}}(x_{\bar{q}},\hat{s}) \times \delta(s x_q x_{\bar{q}} - \hat{s}) \frac{d^2\hat{\sigma}_{q,\bar{q}}}{dp_T^2 dy}, \tag{12}$$

where $\hat{\sigma}$ is the partonic cross section for $q\bar{q} \to W \to X$ integrated over the W decay angular distribution, and f_q, $f_{\bar{q}}$ are the parton distribution functions for the annihilating quarks. p_T and y are the transverse momentum and rapidity of the vector boson, respectively. x_q and $x_{\bar{q}}$ are the proton momentum fractions carried by the annihilating quarks, and $\hat{s}$ is the partonic center-of-mass energy squared. $\hat{\sigma}$ is given by the relativistic Breit-Wigner line shape with $\hat{s}$-dependent width,

$$\frac{d\hat{\sigma}}{d\sqrt{\hat{s}}} \propto \frac{\hat{s}}{(\hat{s}-M_W^2)^2 + \left(\frac{\hat{s}\Gamma_W}{M_W}\right)^2}. \tag{13}$$

The convolution over the parton distribution functions indicated in Eq. (12) results in an $\hat{s}$-dependent parton flux which is referred to as parton luminosity.

Due to the $V-A$ nature of the weak interaction, the W spin is aligned with the direction of the incoming antiquark at lowest order. At the Tevatron energy, a valence quark from the proton or a valence antiquark from the antiproton is involved in the reaction approximately 80% of the time. This means that for roughly 80% of the time the W spin is aligned with the antiproton direction of motion (see Fig. 3). The remaining 20% of the time, the W boson is produced from two sea quarks, and the boson's spin is equally likely to be parallel or antiparallel to the proton's direction. This leads to a significant experimentally observable forward-backward asymmetry between W^+ and W^- production, as discussed in Sec. I.B.

The decay channels open to the W boson are the three lepton channels ($e\nu_e$, $\mu\nu_\mu$, and $\tau\nu_\tau$) and two hadronic channels ($u\bar{d}$ and $c\bar{s}$).[2] Due to the threefold color degeneracy of the quarks, the hadronic channels account for two-thirds of the W decay branching ratio, and each leptonic channel accounts for one-ninth of the branching ratio, neglecting small quark and lepton mass corrections.

Inclusive production of W bosons and their subsequent decay into quarks is dwarfed in production cross section by inclusive QCD dijet production. Hence an inclusive W signal in the dijet channel is extremely difficult to identify. This is particularly true of the Tevatron, where dijet production through initial-state gluons has a large contribution for dijet mass near the W mass. At the $Sp\bar{p}S$ the gluon contribution was lower, allowing the dijet mass "bump" due to W (and Z) decay to be visible (Ansari *et al.*, 1987b; Alitti *et al.*, 1991).

If the W decay axis is perpendicular to the beam axis (which occurs a large fraction of the time since the phase space is maximized in the perpendicular direction), the decay leptons have large transverse momentum due to the large W mass. Most particles produced in the interaction of the proton (and antiproton) remnants have relatively low transverse momentum. Hence one expects low transverse energy flow in the immediate vicinity of the lepton, a property often referred to as energy isolation. The neutrino from the W decay interacts only through the weak interaction and therefore for practical purposes is invisible to the detectors. The remnants of the beam particles are emitted at very small angles and typically travel down the beam pipe undetected, thereby producing an inherent longitudinal momentum imbalance. However, most of the energy emitted at larger angles is detected by building detectors with extensive coverage of the total solid angle. Hence, by measuring the total detected transverse momentum and requiring conservation of total transverse momentum, one can infer the neutrino transverse momentum.

At lowest order, the angular distribution of the lepton from the W decay is governed by the $V-A$ interaction

$$\frac{d\sigma}{d\cos\theta^*} \propto (1 - \lambda q \cos\theta^*)^2, \tag{14}$$

where λ is the helicity of the W boson with respect to the proton direction, q is the charge of the lepton, and θ^* is the angle between the charged lepton and proton beam direction in the W rest frame. Quark and gluon radiation in the initial state has two effects on the W polarization in the laboratory frame. First, there is a kinematic effect because the W spin axis is no longer the beam axis; rather it is now rotated with respect to the beam axis. Second, there is a dynamical effect on the initial-state angular momentum because the radiated partons are spin-1/2 quarks and spin-1 gluons. These effects modify the W decay angular distribution with respect to Eq. (14) in a way that depends on the W transverse momentum (p_T^W),

$$\frac{d\sigma}{d\cos\theta_{\rm CS}} \propto (1 - \lambda q \alpha_1 \cos\theta_{\rm CS} + \alpha_2 \cos^2\theta_{\rm CS}), \tag{15}$$

where the coefficients α are functions of p_T^W. A QCD calculation of these coefficients has been carried out (Mirkes, 1992) at order α_s^2. These calculations are performed in the Collins-Soper frame (Collins and Soper, 1981), and $\theta_{\rm CS}$ is the W decay angle in this frame. A measurement of α_2 as a function of p_T^W can be found in Abbott *et al.* (1999a).

The leading-order QCD processes that generate p_T^W are shown in Fig. 5. When p_T^W is large, i.e., comparable to the W mass, the perturbative QCD calculation can be expressed as a power series in α_s. The differential cross

[2]Here we are referring to the weak-interaction eigenstates rather than the Cabibbo-rotated mass eigenstates.

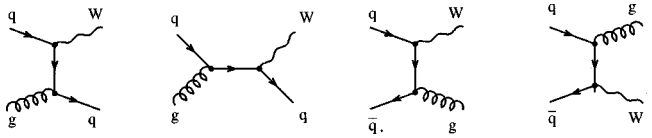

FIG. 5. The leading-order QCD diagrams for initial-state gluon radiation accompanying *W* production.

section in p_T^W has been computed by Arnold and Reno (1989) and Gonsalves *et al.* (1990).

The fixed-order (in α_s) perturbative QCD calculation becomes invalid at low values of p_T^W. This can be understood as follows. The virtuality of the internal propagator is of order p_T^W. As p_T^W reduces, the propagator tends to diverge. Multiple initial-state parton radiation becomes favorable because the reduction in the cross section due to each power of α_s is more than compensated by the divergence of the additional propagator. The divergence of the propagators is manifest in the perturbative calculation as terms of the form $\ln(M_W/p_T^W)$. By rearranging the terms of the perturbative expansion, one can express the cross section as a power series in n of the form $\alpha_s^n[\Sigma_{m=0}^{2n-1} C_{nm} \ln^m(M_W/p_T^W)]$. This technique is called resummation (Collins *et al.*, 1985), and the collection of the leading logarithmic divergence at each order leads to the leading-logarithmic approximation, or LLA. Physically, this corresponds to the summing over the most important contributions from multiple gluon emission diagrams.

The resummed form of the differential cross section in p_T^W is often expressed as a Fourier transform in the space of the impact parameter b,

$$\frac{d^2\hat{\sigma}}{dp_T^2 dy} \approx Y(b,Q) + \int_0^\infty d^2b e^{i\vec{p}_T\cdot\vec{b}} W(b,Q), \tag{16}$$

where W is the resummed piece and Y is a correction based on the fixed-order perturbative result. Y attempts to correct for terms present in the fixed-order calculation which were left out in the resummation procedure. W can be expressed as $W(b,Q) \sim e^{S(b,Q)}$, where $S(b,Q)$ is called the Sudakov form factor.

The resummation technique is a reformulation of the perturbative QCD expansion and extends the applicability to lower p_T^W values. While Nature makes a smooth transition from the high-p_T regime (where fixed-order calculations are most valid) to the intermediate-p_T range where resummation calculations are more valid, this transition has not yet been fully described by rigorous QCD calculations. The transition is approximated in the p_T^W range of 30–50 GeV.

At very low p_T^W values, i.e., below ~10 GeV, the perturbative expansion itself becomes invalid, and nonperturbative phenomenological models need to be applied. These models introduce a nonperturbative form factor to cut off the divergence in the QCD calculation as $p_T \to 0$:

$$W(b,Q) \to W(b^*,Q) e^{-S_{NP}(b,Q)}, \tag{17}$$

where

$$b^* = \frac{b}{\sqrt{1+(b/b_{max})^2}} \tag{18}$$

and b_{max} is chosen in the range 0.5/GeV. S_{NP} is a nonperturbative function with the properties $S \to 0$ as $b \to 0$ and $S \to \infty$ as $b \to \infty$. It has been shown to have the form

$$S_{NP}(b,Q) = h_1(b,x_q) + h_1(b,x_{\bar{q}}) + h_2(b)\ln\left(\frac{Q}{2Q_0}\right), \tag{19}$$

where x_q and $x_{\bar{q}}$ are the momentum fractions of the annihilating quarks, Q_0 is an arbitrary momentum scale, and $h_1(b,x_q)$, $h_1(b,x_{\bar{q}})$ and $h_2(b)$ are empirical functions to be determined from experiment. In the model of Ladinsky and Yuan (1994), these functions are given by

$$\begin{aligned} h_2(b) &= g_2 b^2 \\ h_1(b,x_q) + h_1(b,x_{\bar{q}}) &= g_1 b^2 + g_1 g_3 b \ln(100 x_q x_{\bar{q}}). \end{aligned} \tag{20}$$

These functions provide Gaussian smearing of the transverse momentum. The g parameters are determined by fitting Drell-Yan data.

B. Underlying event

The hard scattering of two partons in a $p\bar{p}$ collision leaves behind the remnants of the proton and the antiproton to form one component of the underlying event. These remnants, as explained in Sec. II.A, are mostly directed forward and backward along the beam line, although a few follow a transverse course, resulting in a low-level background of particles in all events. The charged-particle multiplicity per unit pseudorapidity is ~4 at Tevatron energies and logarithmically increases with center-of-mass energy (Abe *et al.*, 1990a).

Another component of the underlying event results from additional $p\bar{p}$ interactions occurring during the same bunch crossing as the hard scatter. In each crossing, the number of $p\bar{p}$ interactions follows a Poisson distribution, of which the mean, $\bar{N}$, is a function of the instantaneous luminosity ($\mathcal{L}$) and the number of bunches (N_b): $\bar{N} = \mathcal{L}\sigma T/N_b$ (where T is the time for the bunches to travel around the collider, and σ is the $p\bar{p}$ cross section). For a given $\mathcal{L}$, the larger N_b is, the less dense each bunch is and the fewer the number of additional interactions that will occur.

C. Modeling of *W* boson production

Processes involving W bosons are modeled using a Monte Carlo simulation which varies in detail depending on the species and precision of the measurement. There are two principal parts to the modeling: an event generator and a detector simulation.

1. Event generation

Event generators come in two kinds: leading-order, which may or may not attempt some form of next-to-

leading-order QCD and/or quantum-electrodynamic (QED) corrections; and next-to-leading order. A complete next-to-leading-order calculation that is reliable over the broad range of *W* boson physics at hadron colliders does not exist. However, there are a number of partial calculations and various other techniques that can be used to achieve the required precision for any given measurement.

All flavors of event generator use a matrix element calculation convoluted with parton distribution functions [Eq. (12)]. The matrix element depends on the generator. Leading-order generators start with the tree-level *s*-channel subprocess [Eq. (13)] and add next-to-leading-order effects afterward. The next-to-leading-order generators start with a matrix element, which is usually not true next-to-leading-order. Instead, it contains certain next-to-leading-order features of relevance for the particular generator. For example, a next-to-leading-order QED generator may not contain any QCD effects and in fact it may have only parts of the complete next-to-leading-order QED corrections. This leads to many different event generators, each of which deals with certain specific cases.

As stated above, leading-order generators need two corrections: QCD corrections corresponding to initial-state radiation off the incoming partons (and for a few analyses off the outgoing quarks as well), and QED corrections dealing mostly with radiation off the final-state leptons. Initial-state QCD radiation causes transverse momentum (p_T^W) to be imparted to the *W* boson and appears as "jet(s)" of hadrons descending from the radiated parton(s) (see Fig. 5). The initial-state radiation is calculated in a variety of ways. The popular event generators ISAJET (Paige and Protopopescu, 1986), PYTHIA (Sjostrand, 1985; Sjostrand and van Zijl, 1987), and HERWIG (Marchesini and Webber, 1988) introduce radiation off the incoming partons using the QCD Altarelli-Parisi splitting function (Altarelli and Parisi, 1977) and then "hadronize" the resulting parton shower into observable particles. The low-energy cutoff for the radiated partons in these generators is around 1 GeV (6 GeV for ISAJET), where perturbative QCD begins to fail. At lower p_T^W values, nonperturbative parameters such as the intrinsic p_T of initial-state partons are introduced.

Another option is to use either a measured p_T^W distribution or a calculation of p_T^W and simply boost the *W* decay products by hand. The recoiling hadrons are not generated in this case. Several p_T^W calculations have been published (Altarelli *et al.*, 1984; Ladinsky and Yuan, 1994; Ellis and Veseli, 1998), as well as a calculation of the ratio of p_T^W to p_T^Z distributions (Giele and Keller, 1998). These calculations are doubly differential in p_T^W and rapidity. The absolute p_T^W calculations utilize the technique of matching perturbative QCD at large p_T^W to a resummation calculation coupled with a nonperturbative form factor at low p_T^W. For the nonperturbative form factor, Ladinsky and Yuan integrate over impact-parameter space while Ellis and Veseli integrate over momentum space. Both calculations yield similar results. The nonperturbative part involves an *ad hoc* parametrization with parameters that need to be determined from collider and lower-energy data. Some of these parameters vary with the choice of PDF. In the ratio of the p_T^W to the p_T^Z distribution, large contributions from the nonperturbative and resummation regions cancel.

The second correction needed for a leading-order subprocess is a QED correction involving three possibilities: photon radiation off the initial-state partons, the final-state lepton, and the *W* propagator. The PHOTOS Monte Carlo simulation (Barberio and Was, 1994) can generate multiple photon emissions (using LLA) off the final-state lepton and is often is used in conjunction with other generators. It does not compute initial-state radiation or radiation off the propagator.

As with QCD corrections, next-to-leading-order QED calculations also exist which include all or parts of the relevant diagrams. The calculation by Berends and Kleiss (1985) includes the final-state radiation and the half of the propagator radiation that cancels the divergences in the final-state radiation. This corresponds essentially to corrections to *W* decay and is especially useful in the mass measurement, where the final-state radiation changes the measured mass.

The calculation by Baur and Berger (1990) includes all the diagrams but treats the initial- and final-state particles as massless using an energy cutoff to control divergences. Recently, an improved true next-to-leading-order electroweak calculation (Baur *et al.*, 1999) has become available including diagrams to $\mathcal{O}(\alpha^3)$.

2. Detector simulation

The second half of modeling involves the effect of the detector on the event. Usually this consists of some combination of detailed traces through the detector of every particle in the event and parametrizations of the salient features of the event.

Detailed trace simulations such as GEANT (Brun *et al.*, 1978) follow every particle, including any daughters from decays and material interactions, through the detector, accounting for energy losses in the material and simulating the detector signals. This process continues until the particles annihilate or reach some minimum energy. The conversion from energy losses to the simulated data is usually tuned to agree with real data. This form of detector simulation is generally slow and is sometimes sped up by the inclusion of parametrizations of certain aspects. For example, a particle's momentum is obtained not from fitting hits from the tracking chamber, but from smearing the momentum delivered by the generator. In analyses where speed is critical, such as the *W* mass measurement, nearly all parts of the simulation are parametrized.

Among the parametrizations, the most complicated to constrain is the detector response to the "recoil jets" of hadronized particles from initial-state radiation. Since the p_T of the initial-state radiation is relatively low

(mean of 5–10 GeV), the particle p_T in the recoil are often only hundreds of MeV. This results in a poor response in the calorimeter, which is usually calibrated for much-higher-energy particles. For experiments with a central magnetic field, some of these particles are lost as they orbit in the magnetic field at a radius smaller than the calorimeter.

Typically, the parametrization of the recoil, $\vec{u}_T$, is separated into response and resolution components, both of which may be a function of the boson p_T,

$$\vec{u}_T = -\vec{p}_T^{\,W} \cdot \mathcal{R}(p_T^W) \oplus \vec{\sigma}(p_T^W). \tag{21}$$

The exact form of $\mathcal{R}$, which incorporates the mean response, and of σ, which provides the resolution fluctuations, depends on details of the detector.

Both the response and resolution functions may be constrained by using jet, direct-photon, and/or Z events. With a magnetic tracker, reconstructed tracks can be used to calibrate the calorimeter response. Direct-photon and Z events can also be used to constrain the hadronic response and resolution by comparing the measured recoil with the transverse energy of the photon and the transverse momentum of the daughter leptons of the Z boson, respectively. This technique carries two assumptions: that there is no true missing energy in these events, and that the initial-state radiation hadronizes in the same manner, independently of the species of vector boson produced in association with it.

Another simulated element related to the recoil is the underlying event. This is usually parametrized as a function of the instantaneous luminosity by using soft inelastic collisions called minimum-bias events.[3] The effect of these soft collisions is to degrade the resolution and shift the mean of the recoil measurement. It also alters the energy measurement of electrons and decreases the efficiency of any lepton identification requiring energy isolation, since there is more energy everywhere in the event, including near the lepton.

Electron energy measurements are simulated using a parametrization obtained mostly from test-beam data. Depending on the measurement, the electron simulation may also include the effects of the underlying event and additional constraints from physics data, such as an energy scale constraint from known mass resonances.

III. DETECTION OF *W* BOSONS IN $p\bar{p}$ COLLISIONS

The challenge for detectors at $p\bar{p}$ colliders is to extract physics signatures with typical cross sections as small as a few nanobarns, or even picobarns, from the total $p\bar{p}$ cross section, which is many orders of magnitude larger. To set the scale, during the 1990–1996 run of the Fermilab Tevatron accelerator (Run 1), protons and antiprotons were colliding at a center-of-mass energy of 1.8 TeV, resulting in a $p\bar{p}$ inelastic cross section of about 50 mb (Particle Data Group, 1998, p. 206). At this energy, W bosons are produced with a cross section of approximately 20 nb, i.e., once every 250 000 $p\bar{p}$ collisions. To achieve these large rejection factors, the detectors must be designed with sophisticated multilevel trigger systems.

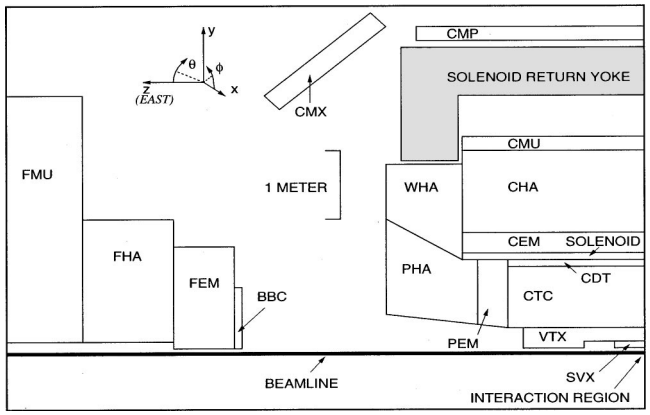

FIG. 6. Cross-section view of the CDF detector. The tracking system comprises SVX, silicon vertex tracker, VTX, vertex tracking chamber, CTC, central tracking chamber, and CDT, central drift tubes. The calorimeter system consists of CEM, central electromagnetic calorimeter, CHA, central hadronic calorimeter, PEM, plug electromagnetic calorimeter, PHA+WHA, plug hadronic calorimeter, FEM, forward electromagnetic calorimeter, and FHA, forward hadronic calorimeter. The muon system is comprised of CMU, central muon chamber, CMP, central muon counter, CMX, central muon extension, and FMU, forward muon chamber.

Two detectors were run in parallel during Run 1 of the Tevatron: CDF (Abe *et al.*, 1988) and DØ (Abachi *et al.*, 1994), whose schematic views can be found in Figs. 6 and 7, respectively. Both detectors aimed at identifying particles coming out of the interaction region over the largest possible $\eta \times \phi$ region.[4] During Run 1 the spread of the interaction vertex was about ± 35 μm (rms) in radius and ± 33 cm (rms) in length along the beam axis. CDF measured the p_T of charged particles, such as muons, with a resolution of $\sigma(p_T)/p_T \approx \sqrt{(0.9p_T)^2 + (6.6)^2} \times 10^{-3}$ (p_T in GeV) in the region of $|\eta| < 1.1$ due to a system of tracking chambers immersed in a magnetic field of $B = 1.4$ T. Outside the solenoid were electromagnetic and hadronic sampling calorimeters divided into central ($|\eta| < 1.1$), endcap ($1.1 < |\eta| < 2.4$), and far-forward regions ($2.2 < |\eta| < 4.2$). They provided an energy resolution of $\sigma(E)/E \approx \sqrt{(14\%)^2/E_T + (1.5\%)^2}$ for central electrons and $[\sigma(E)/E] \approx (50\%)/\sqrt{E_T}$ for central pions (E in GeV). The outermost instrumented area was designed to detect muons using a combination of drift chambers and scintillators.

[3]The term "minimum bias" is used because of the minimal trigger and selection requirements placed on the event, usually a coincidence of hits from scintillators placed near the beamline to catch the remnants of the proton and the antiproton.

[4]The pseudorapidity η is defined as $\eta = -\ln[\tan \theta/2]$, where θ is the polar angle with respect to the beam axis. The azimuthal angle ϕ is measured in the plane perpendicular to the beam axis.

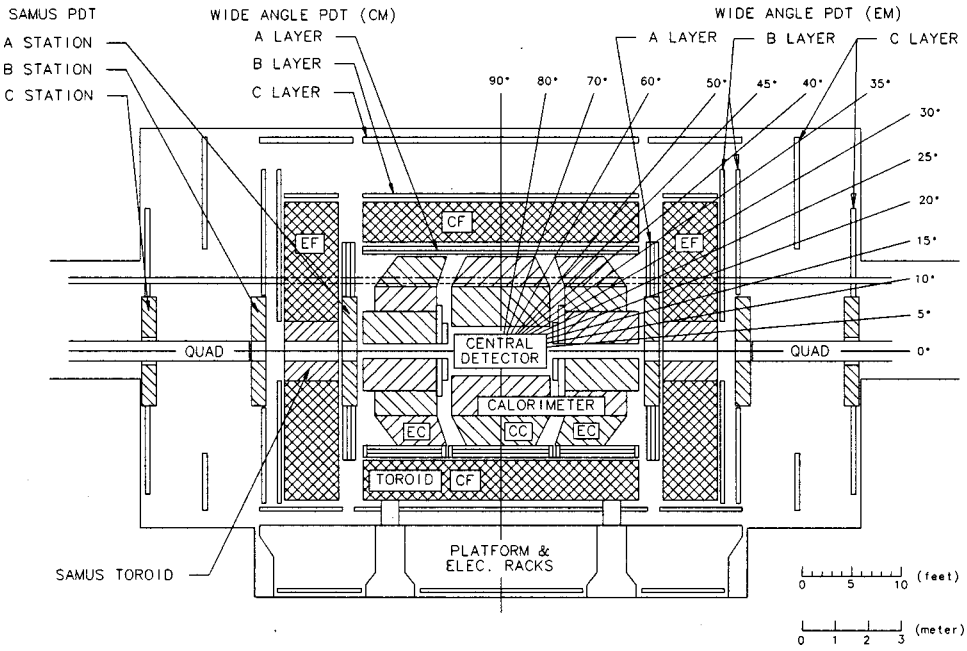

FIG. 7. Cross-section view of the DØ detector. The tracking is done in the central detector. CC, central calorimeter; EC, endplug calorimeter. The muon system consists of CF, central iron magnet, EF, end iron magnet, and SAMUS, small-angle muon system, proportional drift tube (PDT) systems.

The DØ inner tracking chamber was divided into central and forward portions and covered the region $|\eta|<3.2$. Lacking an inner magnetic spectrometer, DØ relied upon calorimetric information for electron and jet energies. Its uranium liquid-argon calorimeter was designed to have better hermiticity and stability and finer segmentation than CDF in the region $|\eta|<4.4$ and provided an energy resolution of $\sigma(E)/E \approx \sqrt{(13.5\%)^2/E_T+(1.1\%)^2}$ for central electrons, $\sigma(E)/E \approx \sqrt{(15.7\%)^2/E_T+(1.0\%)^2}$ for forward electrons, and $\sigma(E)/E \approx 50\%/\sqrt{E_T}$ for pions. The muon system consisted of toroid magnets between layers of drift tubes and was able to measure the muon momentum with a resolution of $\sigma(1/p) = \sqrt{(0.18)^2(p-2)^2/p^4+(0.003)^2}$ over the region $|\eta|<3.3$.

A. Triggering of *W* boson events

In $p\bar{p}$ machines the W boson is triggered using its leptonic decays, which are characterized by a single, isolated, high-p_T lepton, either an electron or a muon, and large missing energy indicative of the decay neutrino. The decays into τ leptons are less commonly pursued because of the additional complications of having to reconstruct the τ through its decay products and the presence of neutrinos among them. The Z boson is widely used to provide control samples in studies of W properties. As with W decays, the Z hadronic decays are difficult to disentangle from the QCD background on an event-by-event basis. But decays into a pair of charged leptons are relatively easy to identify by requiring two isolated high-p_T leptons. Studies involving diboson production and rare W decays benefit from the identification of a photon, a jet, or additional leptons in the event. In the following sections we shall present the strategies used by the Tevatron experiments for triggering and reconstructing the W and Z decay products.

B. Electron and photon detection

Electrons are identified as clusters of adjacent cells in the electromagnetic calorimeter with significant energy deposits. The lateral segmentation of the calorimeter is such that the electron usually deposits most of its energy in a single calorimeter tower. In DØ, for example, clusters with at least 90% of their energy in the electromagnetic section and at least 60% of their energy in the most energetic tower of the cluster are considered as electron candidates. Any sample of events selected solely on the basis of the above criteria will contain a sizable fraction of events with isolated high-energy photons, including those from π^0 decays. The additional requirement of a track pointing to the calorimeter cluster very effectively separates the electron from the photon contribution.

The electron identification can be further refined by comparing the transverse and longitudinal energy deposition profile in the calorimeter to typical shower shapes obtained from test-beam studies with electrons and Monte Carlo simulations of the detector material. Limiting the amount of energy that leaks into the hadronic calorimeter and requiring a track matching the cluster in position reduces the probability of a hadron's being misidentified as an electron. Isolation quantities such as the amount of energy detected in areas surrounding the electron shower are helpful in rejecting events with electrons, photons, and photon conversions inside a jet. To further reduce the main remaining background coming from jets, CDF requires that the energy deposited in the calorimeter match the momentum of the pointing track. DØ cannot measure the momentum of the track but compensates with the higher granularity of its electromagnetic calorimeter.

C. Muon detection

Muons typically interact with small energy loss in the detector, whereas most other particles lose more energy

and are stopped in the calorimeter. A muon signature is therefore a charged track in the central tracking chamber pointing to hits in dedicated chambers placed outside the calorimeter, coupled with an energy deposition in the calorimeter consistent with a minimum ionizing particle.

By constraining the track to come from the beam interaction point, which is inferred from the common origin of all the tracks in the event, one substantially improves the muon momentum resolution and rejects cosmic rays. To reject misidentified backgrounds from energetic punchthrough pions, which deposit only a small fraction of their energy in the calorimeter before escaping, one can increase the isolation of the muon beyond its immediate vicinity, since punch-through pions are generally part of a nonisolated jet environment. Real muons from pion decay in flight or *b*-quark and *c*-quark semileptonic decays are also part of a nonisolated jet environment and rejected by similar cuts.

D. Neutrino detection

Neutrinos undergo only weak interactions and do not leave any direct signs of their passage in the detector. Their transverse energy is inferred from the transverse momentum of all particles recoiling against the *W* boson. The recoil transverse energy $\vec{u}_T$ is calculated as the vector sum of the transverse energies deposited over all the calorimeter towers, except for the ones that contain energy coming from the lepton in *W* decays. Such $\vec{u}_T$ is a measure of the transverse energy of the partons recoiling against the *W* boson in processes shown in Fig. 5. The underlying event is expected to be distributed symmetrically in the transverse plane and therefore its contribution to $\vec{u}_T$ should be zero on average. By momentum conservation, the neutrino transverse energy $\vec{\not{E}}_T$ is the opposite of the vectorial sum of the lepton and the recoil energy: $\vec{\not{E}}_T = -(\vec{u}_T + \vec{E}_T^l)$. A nonzero magnitude for this vector can be found in events without neutrinos due to cracks in the calorimeters or mismeasurements. The recoil energy $\vec{u}_T$ has to be corrected for any underlying event energy that was deposited in the towers associated with the lepton. This contribution is estimated from the energy detected in calorimeter towers away from the lepton.

E. Jet detection

Jet reconstruction is the most commonly used tool to detect the presence of quarks or gluons in the event. The nature of the strong force governing the parton interactions makes it energetically favorable to pull $q\bar{q}$ pairs from the vacuum as the quark or the gluon fly away from the production point. These additional $q\bar{q}$ pairs recombine to form a collimated shower of lower-energy hadrons whose spatial distribution is highly correlated with the direction of the originating quarks and gluons. The ensemble of particles produced by this ''hadronization process'' is called a jet.

A jet is normally reconstructed with a fixed-cone clustering algorithm of radius $\Delta R = \sqrt{\Delta\eta^2 + \Delta\phi^2}$. The jet is seeded by the highest-energy calorimeter tower in the event chosen as the axis of the cone. Any tower found in a cone of radius ΔR is vectorially added to the jet, whose energy and direction are recursively calculated after any addition until no more towers are added. Typical cone sizes range from $\Delta R = 0.3$ to $\Delta R = 0.7$. Smaller or bigger cone sizes usually result in poorer energy resolution because of leakage of particles produced in the fragmentation or increased contribution of energy from the underlying event. Also, as ΔR increases, the jets from two distinct original partons can merge, resulting in lower detection efficiencies.

IV. EARLY STUDIES OF THE *W* BOSON AT HADRON COLLIDERS

The use of hadron colliders to investigate the weak interaction directly was first proposed in 1976, shortly after the first neutral-current results provided a useful measurement of $\sin^2\theta_W$ and hence a strong indication that the *W* and *Z* masses were in the range of 50 to 100 GeV. The proposal to create a proton-antiproton collider was based on the advantage of using a single ring to contain both beams, as well as the desire to have valence antiquarks in order to produce the gauge bosons with the largest possible cross sections. The proposal to convert the CERN SPS into a proton-antiproton collider was approved in 1978, and first collisions at $\sqrt{s} = 546$ GeV were produced in 1981.

A. *Sp$\bar{p}$S* EXPERIMENTS: UA1 AND UA2

The production and decay of the charged boson $W \to l\nu$ was first observed by the two general-purpose experiments UA1 and UA2 in 1982 (Arnison *et al.*, 1983a; Banner *et al.*, 1983). The observation of the neutral boson $Z \to l^+l^-$ followed in early 1983 (Arnison *et al.*, 1983b; Bagnaia *et al.*, 1983). The analysis of these early data showed that

- the masses of *W* and *Z* bosons are in the range expected from the SM prediction (Marciano and Sirlin, 1980; Sirlin, 1980; Llewellyn Smith and Wheater, 1981);
- the production properties are consistent with the Drell-Yan mechanism (Drell and Yan, 1970);
- the decay properties of the *W* and *Z* bosons are consistent with the SM expectations (Weinberg, 1967).

In the following years, the energy of the machine grew to $\sqrt{s} = 630$ GeV, and the data samples reached several hundred *W* bosons and several dozen *Z* bosons by the end of 1985. During this period, 0.7 and 0.9 pb^{-1} of integrated luminosity were accumulated by the UA1 and UA2 experiments, respectively. These data samples allowed the first precision studies of electroweak interactions at hadron colliders. The production and decay properties of the *W* and *Z* bosons were measured (Arni-

son *et al.*, 1985, 1986; Appel *et al.*, 1986; Ansari *et al.*, 1987a; Albajar *et al.*, 1989). The SM parameters derived from the W and Z masses were found to be in good agreement with those obtained in deep-inelastic neutrino interactions. The cross sections, the longitudinal and transverse momentum distributions, and the characteristics of the rest of the event, including the associated production of high-p_T jets, showed good agreement with the QCD improved Drell-Yan model expectations. There was no evidence for any exotic process leading to heavier intermediate vector bosons, heavy leptons, or supersymmetric particles.

In the following five years, high-luminosity CERN $Sp\overline{p}S$ runs with the improved antiproton source allowed the UA2 experiment (Alitti *et al.*, 1990, 1992a, 1992b) to collect an additional ~ 14 pb^{-1} of data (~ 4000 W's).

B. CDF at the Tevatron collider: 1985–1990

After the initial engineering run of the Tevatron collider in 1985, the CDF detector was commissioned and collected ~ 25 nb^{-1} of integrated luminosity at $\sqrt{s} = 1800$ GeV in 1987. The energy increase at the Tevatron collider resulted in a significant increase in the W production cross section and initiated a new era of precision studies of electroweak interactions at hadron colliders by delivering ~ 4 pb^{-1} to the CDF detector during the 1988–1989 period, corresponding to ~ 2700 W candidates. Measurement of the W production and decay properties (Abe *et al.*, 1989, 1991a, 1991b, 1992a) and searches for heavier intermediate vector bosons (Abe *et al.*, 1991c) continued with no evidence of deviations from the SM predictions.

V. PROPERTIES OF THE *W* BOSON

In this section we discuss the measurements of the W mass, width, and production cross section, the lepton charge asymmetry in W decays, p_T^W and jets accompanying W production, and searches for additional charged gauge bosons, rare W decays, and anomalous gauge couplings.

The recent Tevatron run is divided into three periods, usually denoted Run 1A (1992–1993), Run 1B (1994–1995), and Run 1C (1995–1996). During these periods, the CDF and DØ experiments each collected samples of over 200 000 W candidates coming from ~ 20 pb^{-1} in Run 1A, ~ 90 pb^{-1} in Run 1B, and ~ 20 pb^{-1} in Run 1C.

CDF is able to trigger on and measure the momentum of electron and muon tracks in the central pseudorapidity region ($|\eta|<1$) with good precision. Central electrons are required to have an associated track with a momentum comparable to the energy deposition in the calorimeter. The muons must be detected by a track in the central tracking chamber matching hits in either the central muon system, which covers the region $|\eta|<0.6$, or by the central muon extension system, which extends the muon coverage to $|\eta|<1$. Forward electrons ($1.1<|\eta|<2.4$) and muons ($1.9<|\eta|<2.5$) are also selected, but without the requirement of a matching track. The W candidate events are further required to have a neutrino by requiring significant neutrino transverse energy $\not\!\!E_T$, typically $\not\!\!E_T > 25$ GeV. The CDF central electron and muon samples consist of $\sim 61\,000$ and $\sim 34\,000$ W candidates, respectively. The combined forward rapidity electron and muon samples have $\sim 26\,000$ W candidates.

DØ relies on its stable calorimeter response to measure the electron energy. By exploiting its forward coverage, DØ measures both central ($|\eta|<1$) and forward ($1.5|\eta|<2.5$) electrons. Events are selected by requiring $E_T^e > 25$ GeV and $\not\!\!E_T > 25$ GeV. The DØ central and forward rapidity electron samples consist of 49 000 and 19 000 W candidates, respectively. About 11 000 $W \rightarrow \mu\nu$ candidates are identified by detecting muons in the muon system and requiring large $\not\!\!E_T$ in the event.

A. Mass

The most common kinematic variable used to measure the W mass is the transverse mass, analogous to the invariant mass but computed using only the transverse components of the lepton momenta. The transverse mass is given by

$$m_T = \sqrt{[E_T(l)+E_T(\nu)]^2-[\vec{p}_T(l)+\vec{p}_T(\nu)]^2} = \sqrt{2p_T(l)p_T(\nu)\{1-\cos[\phi(l)-\phi(\nu)]\}}. \quad (22)$$

Since the lepton momentum is bounded by the mass of the decaying W boson, and the phase space is maximized in the direction perpendicular to the reference axis in the W rest frame, the $p_T(l)$ and m_T distributions have the characteristic Jacobian shape (see Fig. 8). Much of the W mass information is extracted from the location of the Jacobian edge in the m_T and $p_T(l)$ distributions.

There are two effects (in addition to detector resolution) that smear the Jacobian edge of the $p_T(l)$ distribution at $M_W/2$ and of the m_T distribution at M_W. First, the finite W width causes the mass to be distributed according to the Breit-Wigner line shape about the pole mass. Second, these variables are not invariant under transverse boosts of the W boson. But while the $p_T(l)$ spectrum receives a correction to first order in $\vec{p}_T^{\,W}\cdot\hat{p}_T(l)$, where $\hat{p}_T(l)$ is the unit transverse vector in the lepton direction, the leading correction to the m_T spectrum is $\mathcal{O}[(p_T^W/M_W)^2]$. As explained by Abbott *et al.* (1998c, 1998d), the main advantage of the m_T spectrum in extracting the W mass is that it is less sensitive to our prior knowledge of the p_T^W distribution. However, since the recoil particles are used to measure p_T^W for the computation of m_T, the m_T spectrum is sensitive to the modeling of the recoil response. The charged-lepton p_T is measured with better resolution, but its distribution is more sensitive to p_T^W. These complementary sensitivities are illustrated in Fig. 8, which shows the changes to the shapes of the m_T and $p_T(e)$ spectra induced by p_T^W and the detector resolutions. We observe that the shape of the m_T spectrum is dominated by detector resolutions and the shape of the $p_T(e)$ spectrum by p_T^W.

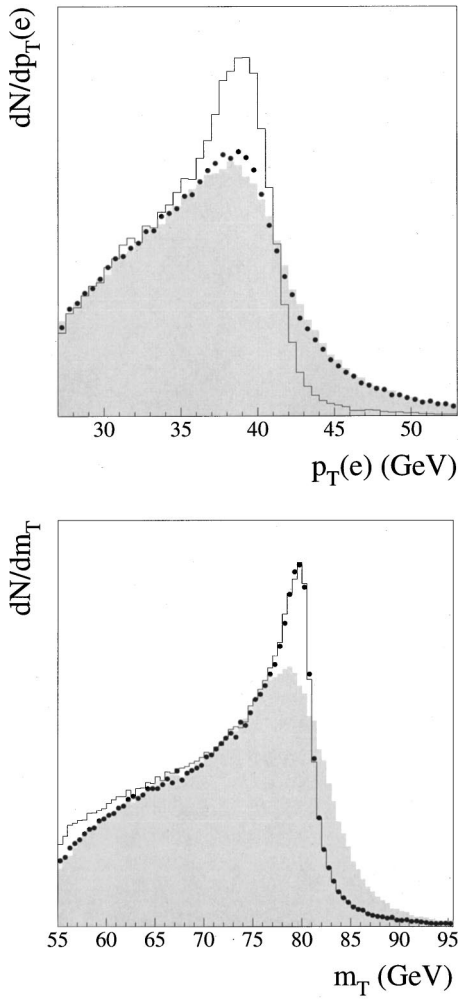

FIG. 8. Kinematic distributions of W bosons: top, the $p_T(e)$ spectrum; bottom: the m_T spectrum; solid line, with $p_T^W=0$; with the correct p_T^W distribution; shaded, with DØ detector resolutions. Figures are from Abbott *et al.* (1998c and 1998d).

A third variable that contains W mass information is the neutrino p_T. The shape of the neutrino p_T spectrum is sensitive to both the p_T^W spectrum and the recoil momentum measurement. Thus the measurement of the W mass from the $p_T(\nu)$ spectrum has the largest systematic uncertainty associated with it. DØ has exploited the complementarity of the measurements from the three spectra by combining them into a single final result.

1. Mass measurement strategy

DØ performs a maximum-likelihood fit to the m_T, $p_T(e)$, and $p_T(\nu)$ spectra, while CDF uses the $p_T(l)$ and $p_T(\nu)$ spectra as a cross check of the transverse mass result. Both experiments use a fast parametric Monte Carlo simulation program that can predict the shape of the spectra as a function of the W mass with high statistical precision.

Using the data collected during Run 1B, CDF performs the W mass measurement with central electrons and muons (Affolder *et al.*, 2000b). DØ exploits its forward tracking coverage to perform the measurement using both central and forward electrons (Abbott *et al.*, 1998c, 1998d, 1999b, 2000c). The DØ muon momentum measurement is not sufficiently precise to measure the W mass effectively.

CDF (Abe *et al.*, 1995b, 1995g) and DØ (Abachi *et al.*, 1996b; Abbott *et al.*, 1998a) also published W mass results with data collected during Run 1A. CDF performed its first W mass measurement using Run 0 data (Abe *et al.*, 1990b, 1991a) when it was the only detector installed along the Tevatron ring.

2. Electron response and resolution

CDF and DØ use different strategies to measure the W mass with electrons, because CDF has a very stable and linear magnetic tracker, while DØ has a very stable and linear electromagnetic calorimeter.

CDF derives the absolute energy scale of the calorimeter from the momentum scale calibration of the central tracking chamber. Therefore the central tracking chamber must be understood very well, and its calibration proceeds as follows. First, the electron tracks in $W\rightarrow e\nu$ decays are used to align the tracking chamber. Any first-order correction to the track curvature causes a difference in the momentum measurement of electrons and positrons because they bend in opposite directions. On the other hand, the calorimeter energy measurement is indifferent to the charge. Thus the calorimeter energy measurement of electrons and positrons is used to measure and correct for curvature errors in the central tracking chamber.

The amount of detector material traversed by the electron is studied using conversion photons. The distribution of the photon conversion radius, after correcting for radius-dependent trigger and conversion-finding efficiency, maps out the radial distribution of the material in radiation lengths. The absolute amount of material is referenced to the known thickness of the central tracking chambers's inner wall.

The effects of this material on electron track parameters is cross checked by studying the ratio of electron calorimeter energy E to the measured track momentum p (E/p ratio). The bremsstrahlung photon is merged with the electron in the calorimeter, hence E is not very sensitive to bremsstrahlung energy loss. The E/p ratio is thus a measure of the effect of bremsstrahlung on p. The tail of the E/p distribution at high values of E/p is particularly sensitive to bremsstrahlung. The E/p ratio measured in W decays is compared with the prediction of a simulation based on the material distribution extracted from the conversion electron analysis. The comparison shows consistency between the two methods (see Fig. 9).

The $J/\psi\rightarrow\mu\mu$ invariant mass is used to set the overall momentum scale of the tracker. Residual corrections are made based on the polar angle dependence of the measured J/ψ mass, and ϕ dependence of the E/p ratio in W events. Further cross checks are made with the $\Upsilon\rightarrow\mu\mu$ invariant mass (see Fig. 10) and the $Z\rightarrow\mu\mu$ invariant mass. Finally, the linearity of the tracker is checked by

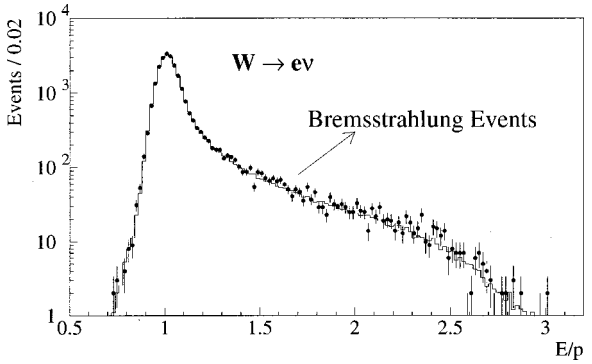

FIG. 9. The E/p spectrum for CDF $W \to e\nu$ candidates (●) compared with the simulation (solid curve).

studying the dependence of the measured J/ψ and Υ masses on the curvature of the tracks.

For the typical momentum of electrons from W decay, the calorimeter resolution is better than the tracker resolution. Therefore the calorimeter E measurement is used to obtain the final electron four-momentum for the W mass fit. The track momentum calibration is transferred to the calorimeter using the peak of the E/p distribution measured in W events. Uniformity corrections are made to the calorimeter to equalize the individual tower responses, remove the response variation within the tower, and remove the time dependence of the response, before setting the absolute calorimeter energy scale.

This extensive and detailed calibration procedure provides a statistically precise, absolute calibration of the tracker and the calorimeter energy scale. The absolute energy scale was used for the Run 1A measurement of the W mass. However, the absolute energy scale derived for Run 1B resulted in a measured value for the $Z \to e^+e^-$ invariant mass incompatible with the extremely precise measurement of the Z mass performed at LEP. At this point, CDF abandoned the absolute measurement and set the electron energy scale to agree with the LEP value for the Z mass. In effect, the CDF Run 1B measurement is based on the ratio of the W mass to the Z mass, as is the case with DØ as described in the following.

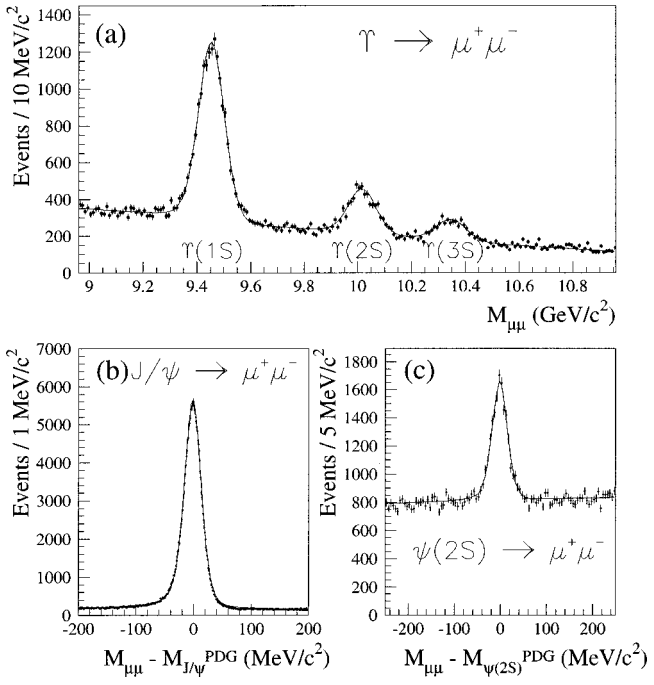

FIG. 10. The ψ and Υ mass fits (solid curves) to the CDF data (●).

In DØ the energy scale calibration is performed directly, using known resonance masses. The linearity of the central and forward calorimeters was measured extensively in beam tests. The sampling fractions for the calorimeter layers were extracted from test-beam data. The calorimeter response measured in beam tests is consistent with the linear parametrization $E_{meas} = \alpha_{EM} \cdot p_{true} + \delta_{EM}$, with indication of deviation from the straight-line response at low energy.

The electromagnetic calorimeter offset parameter δ_{EM} is measured using low-mass resonances, π^0 and $J/\psi \to ee$, which are sensitive to δ_{EM}. The π^0 is reconstructed by identifying candidates in which both photons convert. In the absence of a central magnetic field, the tracks from the conversion electron-positron pair overlap and are detected as a single doubly ionizing track, which gives the direction of the converted photon. The energy of each converted photon cannot be measured separately because the two clusters merge in the calorimeter. By splitting the total π^0 energy equally between the two photons, one can reconstruct a quantity called symmetric mass. The symmetric mass distribution is simulated based on the knowledge of the π^0 momentum spectrum and the calorimeter energy response. The latter is constrained by comparing the measured and simulated symmetric mass distributions (see Fig. 11).

The electromagnetic calorimeter offset parameter can also be measured *in situ* using $Z \to e^+e^-$ decays. The electrons from Z decays are not monoenergetic and therefore one can make use of their energy spread to constrain δ_{EM}. When both electrons are in the central calorimeter, or both in the forward calorimeter, one can write $m_{ee} = \alpha_{EM} \cdot M_Z + f_Z \cdot \delta_{EM}$ for $\delta_{EM} \ll E(e_1) + E(e_2)$. Here f_Z is a kinematic function related to the boost of the Z and is given by $f_Z = [E(e_1) + E(e_2)](1 - \cos\omega)/m(ee)$, where ω is the opening angle between the two electrons. A similar expression can be derived when one electron is central and one is forward. Using these relations, DØ extracts a joint constraint on α_{EM} and δ_{EM} (see Fig. 11). The final δ_{EM} for the central calorimeter is extracted from a combined analysis of the Z, J/ψ, and π^0 information. The δ_{EM} for the end calorimeter is measured using Z data alone.

The electromagnetic calorimeter offset measurement from the low-mass resonances is sensitive to the deviation of the calorimeter response from the straight-line ansatz. This low-energy nonlinearity is constrained by the test-beam data and determines the dominant systematic error on the low-mass resonance determination of the electromagnetic offset.

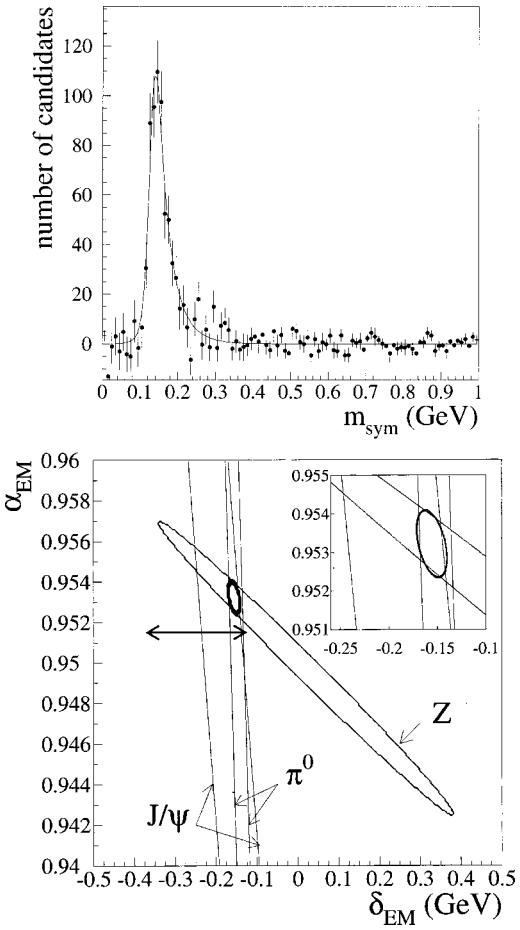

FIG. 11. Response of the DØ electromagnetic central calorimeter: top, the π^0 symmetric mass fit; bottom, the combined $\alpha_{EM}-\delta_{EM}$ constraint. The horizontal arrow in the bottom figure indicates the systematic uncertainty on δ_{EM}.

After correcting the data for the measured central and end calorimeter offsets, DØ determines α_{EM} so that the position of the Z peak predicted by the Monte Carlo simulation agrees with the data, by performing a maximum-likelihood fit to the $m(ee)$ spectrum (see Fig. 12). The data have been reconstructed using the calorimeter energy scale derived from beam tests, which is about 5% below unity. Since the measured W mass is proportional to the energy scale parameter α_{EM}, DØ measures the ratio of the W and Z masses.

The functional form of the electron-energy resolution is given by

$$\left(\frac{\sigma_E}{E}\right)^2 = C^2 + \left(\frac{S}{\sqrt{E_T}}\right)^2 + \left(\frac{N}{E}\right)^2. \tag{23}$$

CDF and DØ take the intrinsic resolution of the calorimeter, which is given by the sampling term S, from the test-beam measurements. The noise term N is represented by the width of the electron underlying event energy distribution (and contains electronic and uranium noise in the case of the DØ calorimeter), which is measured from the data and used in the simulation. The constant term C is measured from the Z line shape of the data, since the true Z width is known well from LEP measurements.

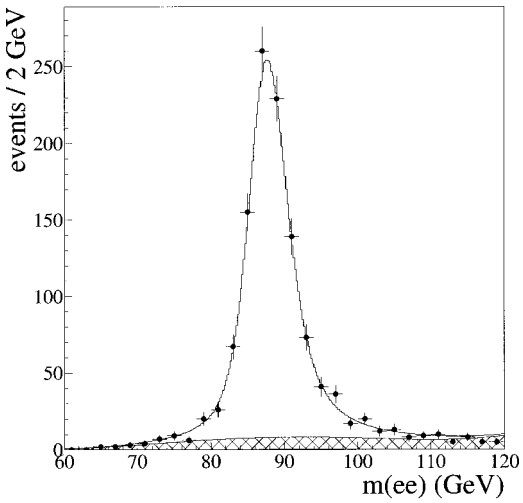

FIG. 12. The DØ dielectron mass spectrum from the Z sample of the central and end calorimeters. The superimposed curve shows the maximum-likelihood fit and the shaded region the fitted background.

3. Muon response and resolution

CDF uses the $Z\to\mu^+\mu^-$ events to set the tracker momentum scale for muons. All of the central tracking chamber alignment, calibration, and material studies are performed and used jointly for the electron and muon channel analyses. Samples of $J/\psi\to\mu\mu$ and $\Upsilon\to\mu\mu$ events are used to check the momentum scale and possible nonlinearity. The momentum of each muon is corrected for energy loss in the material traversed by the muon. The high-statistics Υ and ψ samples were also used to check for possible time dependence in the momentum scale; none was found. The final momentum scale was set with the $Z\to\mu^+\mu^-$ events alone in order to have a procedure consistent with the electron channel analysis.

CDF determines the muon momentum resolution from the W and Z data. The wire hit patterns from W data are used to determine the track covariance matrix, which is then used to smear the muon track in the simulation. The covariance matrix is scaled by an overall resolution parameter. The resolution parameter is then extracted by fitting the $Z\to\mu^+\mu^-$ data line shape with Monte Carlo templates. The momentum scale and resolution measurements are largely uncorrelated.

4. Recoil response and resolution

The $Z\to l^+l^-$ events are used to measure the detector response and resolution to the recoil particles, using the method discussed in Sec. II.C.2. The transverse momentum of the Z boson is measured using the leptons and the recoil particles separately. By requiring that there be p_T balance in these events, one can calibrate the recoil response relative to the lepton response.

The widths of the p_T balance distributions in two orthogonal transverse directions are sensitive to the recoil resolution. The recoil resolution receives contributions from the "hard" recoil of particles causing the boson p_T

and from the "soft" component due to the underlying event. The former component is measured by studying the p_T dependence of the balance width in $Z \to l^+ l^-$ events. The latter is independent of the boson p_T and is derived from the measured p_T imbalance in minimum-bias events. The parameters in the overall recoil resolution parametrization are then measured by fitting the $Z \to l^+ l^-$ data. Since the W mass analysis samples are restricted to low measured boson p_T [$p_T(W) < 15$ GeV for DØ and $p_T(W) < 20$ GeV for CDF], the resolution on the "soft" component of the hadronic activity dominates the total recoil resolution. The events with low boson p_T provide more kinematic information on the W mass and also have lower contamination from misidentification backgrounds, as compared to events with high boson p_T.

As described above, the detector response model in both CDF and DØ W mass analyses is tuned largely on the $Z \to l^+ l^-$ collider data. As a cross check, various distributions measured in the W data are compared with the predictions of the Monte Carlo simulation. These checks provide important confirmation that the detector response is well understood.

5. Production and decay dynamics

As described in Sec. V.A and below, the production and decay dynamics of the W influence the kinematics of the decay leptons, thus affecting the fitted value of the W mass. The relevant aspects of the W production and decay dynamics are the transverse momentum and longitudinal boost distributions, the parton luminosity, the decay angular distribution, and QED radiative effects.

Both CDF and DØ use the Z events to understand the p_T^W distribution, since the production dynamics are very similar. While the recoil resolution is too poor to enable the direct measurement of the true p_T^W at low p_T, the decay leptons from the Z boson can be measured well and the true p_T^Z can be inferred from them. CDF uses an empirical fit to the p_T^Z distribution from the leptons as the input to the Monte Carlo simulation. The p_T^W distribution is derived from this fit by using the theoretical prediction for the ratio of p_T^W and p_T^Z distributions. The calculation is based on the model described in Sec. II.A with perturbative, nonperturbative, and resummed components of the boson p_T spectra. DØ uses the same calculation to predict the p_T^W and p_T^Z spectra and tunes the parameters in the model to fit the Z data. In either technique, the statistics of the Z data dominate the uncertainty in the predicted p_T^W spectrum.

In principle, if the acceptance for the W decays were complete, the transverse mass distribution or the lepton p_T distributions would be independent of the W rapidity. However, cuts on the lepton angle in the laboratory frame cause the observed distributions of the transverse momenta to depend on the W rapidity. Hence a measurement of the W rapidity distribution is useful in limiting the impact of the production model uncertainty on the W mass.

CDF has used the lepton charge asymmetry from W decays to constrain PDF's (see next section), which in turn control the W rapidity distribution. The DØ measurement is less sensitive to PDF's, since the combined central and forward electron measurements imply a more complete rapidity coverage. DØ has also checked that the rapidity spectrum of the decay electron, which is correlated with the W rapidity, agrees with the Monte Carlo prediction when corrected with the rapidity-dependent efficiency and background.

CDF and DØ use the calculation of Mirkes (1992) described in Sec. II.A to predict the W decay angular distribution. DØ has made a preliminary measurement of the α_2 parameter as a function of p_T^W (Abbott *et al.*, 1999a). The measurement is consistent with the calculation of Mirkes (1992).

Both experiments use the Berends and Kleiss (1985) calculation to simulate QED radiative decays of the W boson (see Sec. II.C). The Monte Carlo simulation includes the detector response to the radiated photon, including the merging of collinear photons with the electron in the calorimeter.

6. Backgrounds

Backgrounds in the W candidate sample arise from physics sources which have the same final state and from detector-related causes such as misidentification or acceptance losses. The dominant physics background is $W \to \tau\nu \to l\nu\bar{\nu}\nu$, which is kinematically suppressed because of the significantly lower lepton p_T. This background amounts to approximately 1% of the selected W sample. Other sources of physics background, such as $Z \to \tau^+\tau^-$, WW, and $t\bar{t}$, are negligible.

Detector-related backgrounds arise from QCD jet events in which a jet mimics a lepton and there is sufficient energy mismeasurement to produce significant $\not\!\!E_T$, from $Z \to l^+ l^-$ events where the second lepton is not detected, and from cosmic rays. Both experiments extract the shape of the "QCD" background from data by inverting the lepton identification cuts, thus rejecting true leptons and selecting a subsample of the misidentified leptons. The normalization of the QCD background is obtained by applying the same lepton selection and antilepton selection cuts to a predominantly QCD jet sample. CDF uses an inclusive sample with low m_T, while DØ uses a similar sample with low $\not\!\!E_T$ (see Fig. 13). The QCD background fraction in the DØ central and forward electron samples are 1.6% and 3.6%, respectively. In the CDF electron and muon W samples this background contributes about 0.4% within the W mass fitting window.

Monte Carlo predictions are used to estimate the background from $Z \to l^+ l^-$ with a missed lepton. This source contributes less than 0.5% in the DØ samples and the CDF electron sample, and 3.6% in the CDF muon sample due to the more limited detector coverage for muons than for electrons. Cosmic rays contribute 0.1% to the CDF muon sample, most of them having

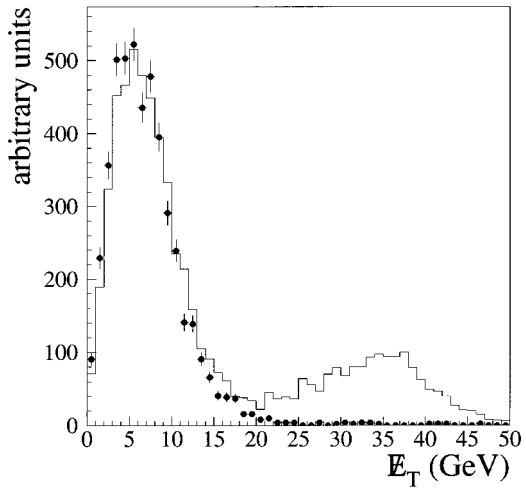

FIG. 13. The neutrino transverse energy ($\not\!\!E_T$) spectra of a sample of events from DØ: solid line, events that pass the electron-identification cuts; ●, events that fail the cuts.

been removed by the rejection of back-to-back tracks and an impact-parameter cut.

7. Mass fit results and uncertainties

The distributions of m_T, $p_T(e)$, and $p_T(\nu)$ from the data are compared to the predictions of the fast Monte Carlo program to obtain the best estimate of the *W* mass. For a given value of the true *W* mass, the Monte Carlo program is used to predict the observed spectrum, including the background with the measured shape and normalization. The predicted spectrum is treated as a probability distribution function by normalizing its integral to the number of data events. Over the range of the data spectrum used for the fit, the likelihood $L(m)$ of observing the data distribution given the chosen value of the true *W* mass m is computed as $L(m) = \Pi_{i=1}^{N} p_i^{n_i}(m)$, where $p_i(m)$ is the value of the predicted probability for bin i, and n_i is the number of data entries in bin i. The product runs over the N bins inside the fit region. $L(m)$ is computed for a range of m, and a quadratic fit to $-\ln[L(m)]$ is used to extract the maximum-likelihood estimate for the *W* mass, i.e., the value of m for which $-\ln[L(m)]$ is minimized. The 68% confidence level interval in m is defined by the values of m at which $-\ln[L(m)]$ increases by half a unit from its minimum. The fits to the Run 1B data are shown in Figs. 14 and 15. Table I summarizes the results.

Extensive consistency checks are performed, including χ^2 and Kolmogorov-Smirnov probability tests between the data and the best-fit Monte Carlo spectra, deviations in the signed χ distributions (where χ is the residual between the data and the Monte Carlo expectation normalized by its error), and stability of the fit results under changes in the fitting region. The samples are split into subsamples in bins of p_T^W and lepton p_T and the corresponding best-fit Monte Carlo distributions are compared for consistency. DØ also checks the variation of the fitted *W* mass when the data are binned in the

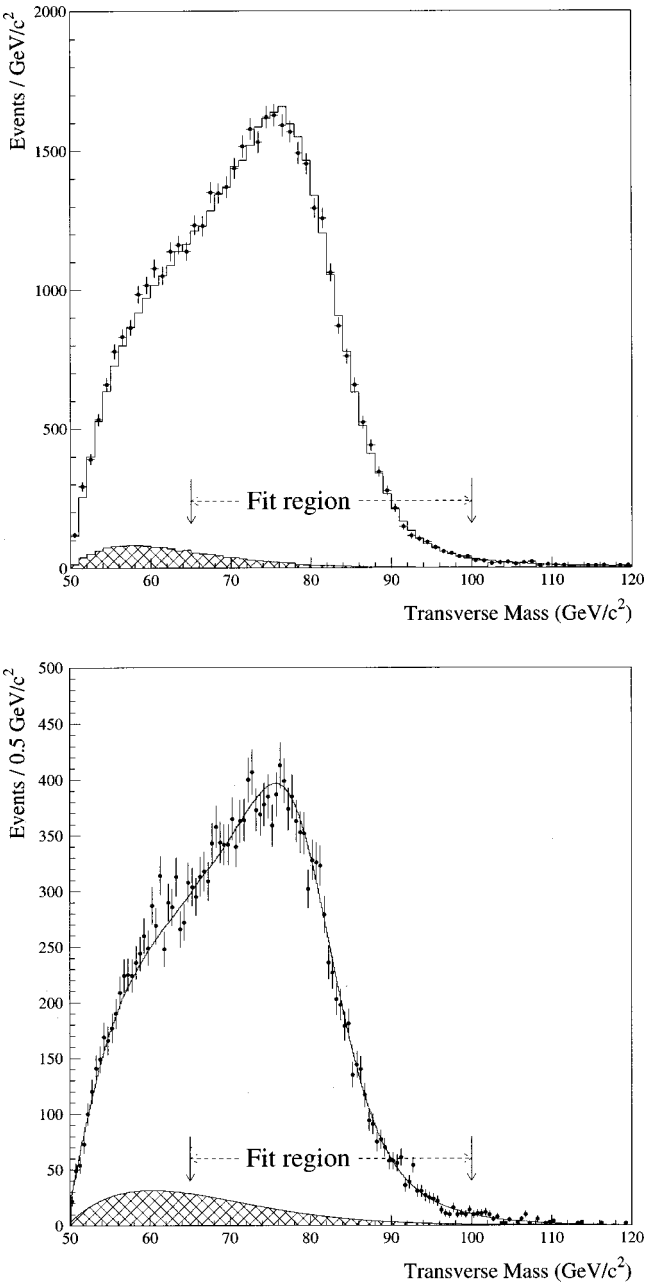

FIG. 14. The *W* transverse mass fits (–) to the CDF candidate events (●) and the expected backgrounds (hatched). The top plot shows the $W \to e\nu$ data and the bottom plot shows the $W \to \mu\nu$ data.

azimuthal angle of the electron, the azimuthal angle of the recoil, instantaneous luminosity, chronological time, and when the fiducial cut on the pseudorapidity of the electron is varied. The stability of the measured mass under these cross checks gives confidence in the results and the estimated uncertainties.

As a consistency check, DØ also fits the transverse mass distribution of the $Z \to e^+e^-$ events, reconstructed using each electron and the recoil. The measured energy of the second electron is ignored, both in the data and in the Monte Carlo program used to obtain the templates. The fits are good and the fitted masses are consistent with the input *Z* mass.

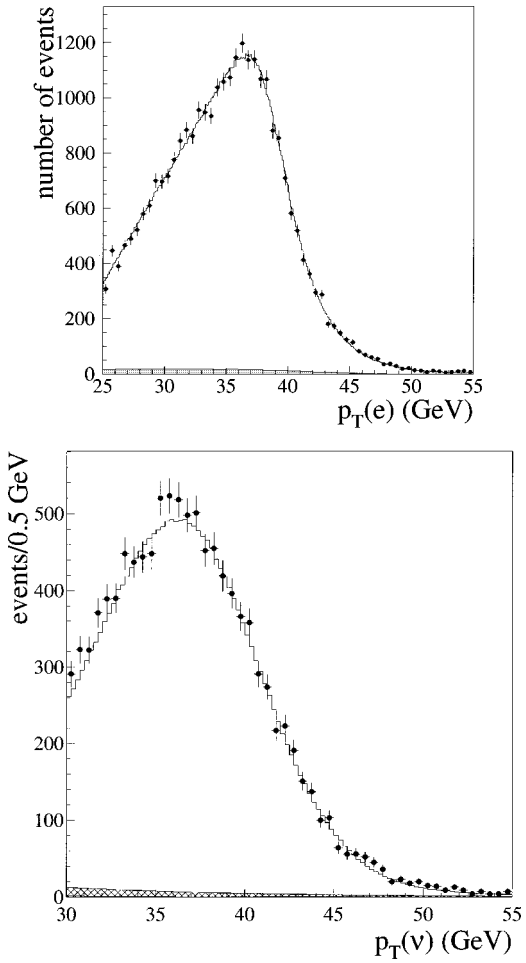

FIG. 15. The *W* mass fits (–) to the DØ data (●) and expected backgrounds (shaded): top, the central calorimeter $p_T(e)$ spectrum; bottom, the end calorimeter $p_T(\nu)$ spectrum.

CDF performs a simultaneous fit for the mass and width of *W* near the Jacobian edge. The *W* width obtained is consistent with the SM value, and the fitted mass is consistent with the result from the one-dimensional fit. This gives confidence that the detector response which affects the observed Jacobian edge has been modeled correctly in the simulation.

Systematic uncertainties on the fitted *W* masses are estimated using the Monte Carlo simulation. The various parameters defining the production and decay model, the detector response to the lepton and the hadronic recoil, and the background shapes and normalizations are varied by $\pm 1\sigma$ and the effects propagated to the *W* mass. CDF keeps track of correlated errors between the electron and muon measurements, while DØ keeps track of the correlations between the central and forward electron analyses and the correlations between the m_T, $p_T(e)$, and $p_T(\nu)$ fits in both analyses. Correlations with analyses based on previous Run 1A data sets are also computed.

Tables II and III show a summary of the systematics on the CDF and DØ results from Run 1B. DØ has combined the six measurements [central and forward electron samples and m_T, $p_T(e)$, and $p_T(\nu)$ fits] using a sophisticated error analysis taking into account all statistical and systematic correlations. The combined Run 1B DØ measurement is $M_W = 80.498 \pm 0.095$ GeV. The χ^2/dof is 5.1/5, with a probability of 41%. The consistency of the six results indicates that the ingredients of the Monte Carlo model and their uncertainties are understood. The CDF Run 1B combined electron and muon channel result is $M_W = 80.470 \pm 0.089$ GeV. When the measurements from Run 1A are included, the Run 1 results become

$$M_W^{D\emptyset} = 80.482 \pm 0.091 \text{ GeV},$$
$$M_W^{CDF} = 80.433 \pm 0.079 \text{ GeV}. \quad (24)$$

Assuming a common uncertainty of 25 MeV in the hadron collider measurements due to PDF's and QED radiative corrections, the hadron collider average (including the UA2 measurement) is $M_W = 80.452 \pm 0.062$ GeV. The LEP2 *W* mass average from direct *W* reconstruction is $M_W = 80.401 \pm 0.048$ GeV, and the result combined with the threshold scan is $M_W = 80.401 \pm 0.048$ GeV (LEP WW Working Group, 2000). The world average of the direct *W* mass measurements is $M_W = 80.420 \pm 0.038$ GeV. A global fit to all electroweak measurements excluding the direct *W* mass measurements predicts $M_W = 80.381 \pm 0.026$ GeV (LEP Collaborations, 2000a). Figure 16 gives a summary of the most recent direct *W* mass measurements.

In Fig. 17 we compare the measured *W* and top-quark masses (Abbott *et al.*, 1999e; Abe *et al.*, 1999b, 1999d) from DØ and CDF with the the values predicted by the SM for a range of Higgs mass values (Degrassi *et al.*, 1997; Degrassi *et al.*, 1998). Also shown is the prediction (Chankowski *et al.*, 1994; Garcia and Sola, 1994; Dabelstein *et al.*, 1995; Pierce *et al.*, 1997) for a model involving supersymmetric particles assuming the chargino, the

TABLE I. CDF and DØ electron and muon channel *W* mass results and statistical errors (in GeV) from Run 1B.

CDF	Central electron	Central muon
m_T	80.473 ± 0.065	80.465 ± 0.100
DØ	**Central electron**	**Forward electron**
m_T	80.438 ± 0.070	80.757 ± 0.107
$p_T(e)$	80.475 ± 0.087	80.547 ± 0.128
$p_T(\nu)$	80.37 ± 0.11	80.740 ± 0.159

TABLE II. Systematic uncertainties in the *W* mass (in MeV) in the CDF measurements from the Run 1B data.

Source	$W\to e\nu$	$W\to \mu\nu$	Common
Lepton scale	75	85	
Lepton resolution	25	20	
Parton distribution function	15	15	15
p_T^W	15	20	3
Recoil	37	35	
Higher-order QED	20	10	5
Trigger, lepton identification bias		$15\oplus 10$	
Backgrounds	5	25	
Total	92	103	16

lightest Higgs boson, and left-handed selectron masses are greater than 90 GeV. The measured values are in agreement with the prediction of the SM and favor a light standard-model Higgs boson. The results are also consistent with the MSSM prediction.

B. Width

The width of *W* can be measured directly by analyzing the *W* line shape, which is given by the Breit-Wigner distribution [see Eq. (13)]. In a hadron collider, the mass dependence of this cross section is modified by the parton distribution function [see Eq. (12)].

In principle, the entire high-m_T half of the Jacobian edge contains information on Γ_W. However, the distribution falls rapidly close to the Jacobian peak and therefore is sensitive to the detector resolution, particularly the hadronic recoil resolution used to reconstruct $p_T(\upsilon)$. But away from the Jacobian peak, the Breit-Wigner distribution falls slowly compared to the resolution and is much less sensitive to resolution smearing. CDF performs an analysis of the m_T line shape in the range $100<m_T<200$ GeV to extract Γ_W, where the lower window limit is chosen to optimize sensitivity considering both statistical and systematic uncertainties.

TABLE III. *W* mass uncertainties (in MeV) in the combined DØ measurement from the Run 1B data.

Source	Uncertainty in MeV
W statistics	61
Z statistics	59
Calorimeter linearity	25
Calorimeter uniformity	8
Electron resolution	19
Electron angle calibration	10
Recoil response	25
Recoil resolution	25
Electron removal	12
Selection bias	3
Backgrounds	9
Parton distribution function	7
Parton luminosity	4
$p_T(W)$	15
$\Gamma(W)$	10
Radiative corrections	12

1. Direct Γ_W measurement

CDF has performed a direct measurement of the total *W* width in the electron decay channel using Run 1A data (Abe *et al.*, 1995c) and in both electron and muon decay channels using Run 1B data (Affolder *et al.*, 2000a). The analysis technique and procedure is similar to the *W* mass measurement described in Sec. V.A. The simulation produces m_T spectra for Γ_W values between 1.0 and 3.0 GeV in 50-MeV steps. Each spectrum is normalized to the background-subtracted data in the region $m_T<200$ GeV, and backgrounds with the measured shapes and normalizations are added to the predicted spectra. A binned maximum-likelihood fit in 1-GeV bins

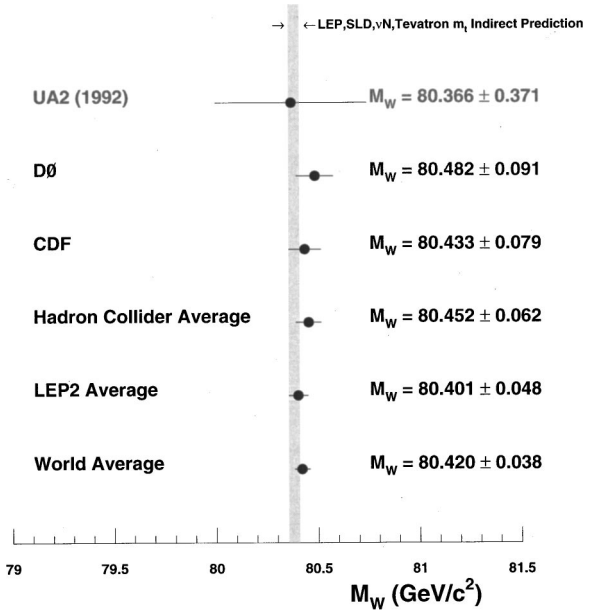

FIG. 16. A comparison of recent measurements of the *W* mass. The shaded region indicates the predicted *W* mass value from global fits to other electroweak measurements.

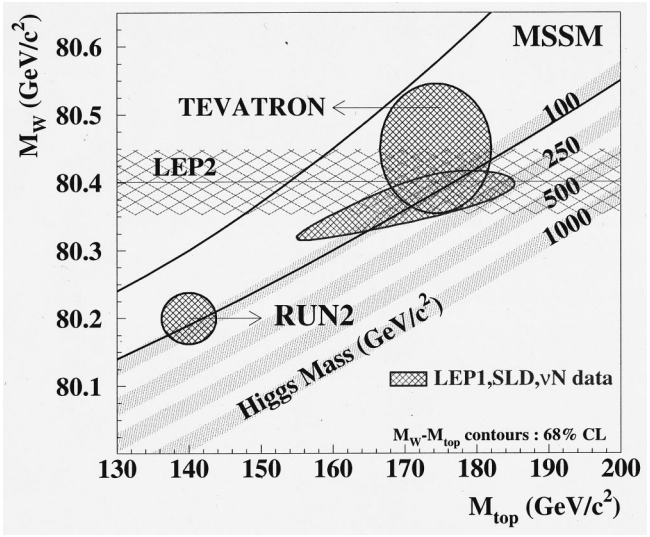

FIG. 17. A comparison of the *W* and top-quark mass measurements with the SM predictions for different Higgs masses. The width of the bands for each Higgs mass value indicates the uncertainty due to the error in $\alpha(M_Z^2)$. Also shown is the direct *W* mass measurement from the LEPII experiments and the indirect limits from LEP1, SLD, and neutrino experiments. The area between the two solid lines is the range allowed by the MSSM. The size of the "Run2" ellipse indicates the precision expected to be achieved from Run 2A data.

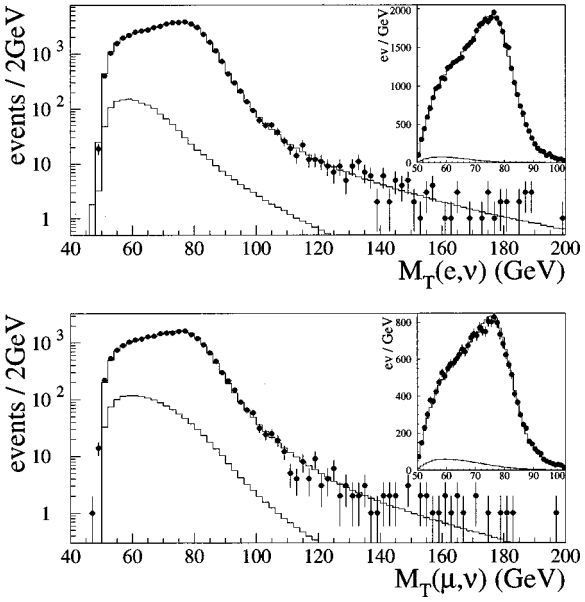

FIG. 18. CDF transverse mass spectra (filled circles) for $W \rightarrow e\nu$ (upper) and $W \rightarrow \mu\nu$ (lower) data, with best Monte Carlo fits superimposed as a solid curve. The lower curve in each plot shows the sum of the estimated backgrounds. Each inset shows the 50–100 GeV region on a linear scale.

over the $100 < m_T < 200$ GeV window yields $\Gamma_W = 2.175 \pm 0.125(\text{stat})$ GeV for the electron channel and $\Gamma_W = 1.780 \pm 0.195(\text{stat})$ GeV for the muon channel. Figure 18 shows the m_T distributions with the best-fit Monte Carlo templates and the backgrounds.

Sources of systematic uncertainty that alter the shape of the m_T distribution are the electron and muon energy scales, the nonlinearity of the calorimeter affecting the electron E_T, the recoil model, the p_T^W spectrum, the parton distribution functions, QED radiative corrections, the *W* mass, and the backgrounds. The systematic uncertainties for the measurements from the Run 1B data are summarized in Table IV. The combined $e+\mu$ result is $\Gamma_W = 2.04 \pm 0.11(\text{stat}) \pm 0.09(\text{syst})$ GeV. The result is in good agreement with the SM prediction $\Gamma_W = 2.093 \pm 0.002$ GeV (Particle Data Group, 1998, p. 225) and puts an upper limit on the *W* partial width into new decay modes.

C. Cross section

As mentioned in Sec. I.B, the production cross sections of *W* and *Z* bosons provide insight into the proton's internal structure and the *W* and *Z* couplings to quarks. The largest single source of uncertainty in the

TABLE IV. Uncertainties in the CDF *W* width Γ_W measurements (in MeV) from Run 1B data.

Source	$W \rightarrow e\nu$	$W \rightarrow \mu\nu$	Common
Statistics	125	195	
Lepton E or p_T nonlinearity	60	5	
Recoil model	60	90	
p_T^W	55	70	
Backgrounds	30	50	
Detector modeling, lepton ID	30	40	
Lepton E or p_T scale	20	15	
Lepton resolution	10	20	
Parton distribution function	15	15	15
M_W	10	10	10
Higher-order QED	10	10	10
Total systematic	115	135	25
Total statistical⊕systematic	170	235	25

measurement of the inclusive W and Z cross sections is the integrated luminosity used for the absolute normalization. By carefully designing the analysis, one can completely cancel the luminosity normalization in the $\sigma \cdot B$ ratio of the W to Z bosons, along with certain other sources of systematics, thus making the measurement of R in Eq. (9) much more precise than the individual $\sigma \cdot B$ measurements. R is used to derive an indirect measurement of Γ_W, according to the method discussed in Sec. I.A, exploiting the fact that on the theoretical side, as well, the calculation of the inclusive cross-section ratio σ_W/σ_Z is less sensitive to parton distribution functions and QCD corrections. Similar considerations apply to the measurement of $\tau-e$ universality using the ratio of $\sigma_W \cdot B$ in the τ and e channels [see Eq. (11)].

CDF and DØ have published measurements of $\sigma \cdot B$ for the electron and muon decay channels of W and Z bosons and for Γ_W extracted from R. DØ published both electron and muon channel measurements from the Run 1A data (Abachi *et al.*, 1995c; Abbott *et al.*, 1999f) and the electron channel measurement from the Run 1B data (Abbott *et al.*, 2000b). CDF has published these measurements in the electron channel from the Run 1A data (Abe *et al.*, 1995a, 1996b) and the Z boson measurement in the muon channel from Run 1B (Abe *et al.*, 1999c). The most recent τ channel measurement was performed by DØ from Run 1B data (Abbott *et al.*, 2000e) using a special τ trigger.

1. Electron measurement

Both central and forward electrons are used. CDF requires the W electron to be central and at least one of the two Z electrons to be central. The second Z electron is allowed to be forward in order to increase the Z acceptance and to ensure that the second electron's rapidity distribution follows that of the neutrino in the W decay. This causes the uncertainty in the acceptance for the W and Z bosons to correlate strongly and hence cancel in the cross-section ratio. DØ uses both central and forward electrons for the W decay and allows either Z electron to be central or forward.

Similar reasoning guides the electron identification requirements. The W electron is required to satisfy electromagnetic cluster cuts and is required to have a matching track associated with the cluster. One of the Z electrons is required to satisfy the same criteria, while the second electron has much looser requirements. The latter technique not only increases the efficiency of Z identification (Z statistics are a limitation while W statistics are not), but also causes the second Z electron to emulate the W neutrino more closely. This allows further cancellation of efficiency-related systematics in the cross-section ratio.

Detector acceptances are estimated using a Monte Carlo program similar to the one used for the direct W mass and width measurements. The boson mass, rapidity, and p_T distributions are generated similarly, and the detector geometry, response, and resolution to the lepton and the hadronic recoil are parametrized and modeled in the simulation. QED radiative effects are also simulated. The detector simulation is tuned on W, Z, and minimum-bias data using the techniques described earlier for the W mass analyses.

Electron identification efficiencies are measured using the $Z \rightarrow e^+e^-$ data. Tight cuts are used to identify one electron, and the invariant mass reconstructed with a second loosely identified electromagnetic cluster is required to be in the Z peak region. A fairly pure $Z \rightarrow e^+e^-$ sample can be identified in this way. The second electromagnetic cluster provides an unbiased sample with which to measure the identification cut efficiencies.

This technique assumes that the cut efficiencies for the two electrons are uncorrelated. DØ has checked for such correlations in the calorimeter-based cuts by using a GEANT-based simulation. The impact of such a correlated bias is found to be small compared to the uncertainty on the efficiency, and is neglected. The track-based cuts are checked using the data. The tracking efficiency is found to be 1.7% lower than what one would get assuming no correlations. The effect of this correlation cancels in the ratio of cross sections.

The backgrounds in the $W \rightarrow e\nu$ sample are estimated using the same techniques as described in the W mass analysis section. The background fraction in the $Z \rightarrow e^+e^-$ sample is estimated using the sidebands of the Z peak. The background shape is determined from data selected similarly to the signal sample, but passing anti-electron cuts. One then fits for the background fraction by fitting the $Z \rightarrow e^+e^-$ mass distribution with a linear combination of the background shape and simulated signal shape.

The measurement of the absolute luminosity is very important for the measurement of inclusive W and Z cross sections. The luminosity is measured from the rate in scintillator counters close to the beam, after correcting for the counter efficiency and the acceptances for single-diffractive, double-diffractive, and nondiffractive components of the total $p\bar{p}$ cross section. CDF and DØ differ in their luminosity calculation in that CDF uses its own measurement of the inelastic $p\bar{p}$ cross section, while DØ uses the "world average" of the results from CDF, E710, and E811. Consequently, CDF and DØ cross sections are *ab initio* different, and care must be taken in comparing and combining their results and in comparing them to other hard-scattering cross sections.

DØ has also measured the $W \rightarrow e\nu$ cross section at center-of-mass energy $\sqrt{s}=630$ GeV, using data collected during Run 1C. Since there were insufficient $Z \rightarrow e^+e^-$ events to remeasure efficiencies, the efficiency measurements made at $\sqrt{s}=1800$ GeV were extrapolated as a function of the extraneous energy density in the event. Background estimates were also extrapolated by scaling the estimates from $\sqrt{s}=1800$ GeV data by the ratio of signal and background process cross sections. The result for 630 GeV is $\sigma_W \cdot B(W \rightarrow e\nu) = 658 \pm 58(\text{stat}) \pm 34(\text{syst})$ pb.

Table V shows the results and uncertainty contributions for the CDF and DØ measurements of the cross sections. Table VI shows the same for the measurement of the cross-section ratio R. Consistency checks are per-

TABLE V. DØ and CDF number of events N_{evts}, background fractions f, kinematical plus geometrical acceptance A, trigger plus selection efficiency ϵ, and total cross section times leptonic branching fraction $\sigma \cdot B$ for W and Z reconstructed in both leptonic channels. The standard-model predictions are (see Abbott *et al.*, 1999e for a discussion) $\sigma_W \cdot B(W \to l\nu) = 2.42^{+0.13}_{-0.11}$ nb and $\sigma_Z \cdot B(Z \to l^+l^-) = 0.226^{+0.011}_{-0.009}$ nb per lepton family.

DØ	$W \to e\nu$	$Z \to ee$	$W \to \mu\nu$	$Z \to \mu\mu$
N_{evts}	67078	5397	1665	77
f (%)	6.4±1.4	4.5±0.5	22.1±1.9	10.1±3.7
A (%)	46.5±0.4	36.6±0.3	24.8±0.7	6.5±0.4
ϵ (%)	67.1±0.9	74.4±1.1	21.9±2.2	52.7±4.9
$\sigma \cdot B$ (nb)	2.31±0.11	0.221±0.011	2.09±0.25	0.178±0.032
$\int L(\text{pb}^{-1})$	84.5±3.6	84.5±3.6	11.4±0.6	11.4±0.6
CDF	$W \to e\nu$	$Z \to ee$	$W \to \mu\nu$	$Z \to \mu\mu$
N_{evts}	13796	1312	1436	2417
f (%)	12.3±1.2	2.1±0.7	15.3±2.1	7.5±1.6
A (%)	34.2±0.8	40.9±0.5	19.0±0.9	16.6±0.4
ϵ (%)	72.0±1.3	69.6±1.7	82.1±3.5	58.1±1.3
$\sigma \cdot B$ (nb)	2.49±0.12	0.229±0.012	2.21±0.22	0.233±0.018
$\int L(\text{pb}^{-1})$	19.7±0.7	19.7±0.7	3.54±0.24	107.4±7.1

formed by measuring the cross section separately in different rapidity regions, and with subsamples binned in instantaneous luminosity. Further checks are performed by measuring the cross sections and the cross-section ratio with different kinematic cuts. Raising the kinematic cuts on the p_T of the leptons reduces the acceptance but also reduces the backgrounds. Since the acceptance corrections and backgrounds for the W and Z samples are different, the stability of the measurements with variation in the kinematic cuts gives confidence that these corrections are well understood.

2. Muon measurement

DØ has published measurements of the inclusive $W \to \mu\nu$ and $Z \to \mu^+\mu^-$ cross sections and their ratio R from Run 1A using central muons. Candidate muon tracks must be confirmed by the presence of energy in the calorimeter along the muon trajectory. Typically a muon deposits ~ 3 GeV; at least 1 GeV is required. To obtain a reliable momentum measurement, the minimal integral of the magnetic field in the toroidal magnet along the muon track is required to be greater than 2 Tm. This requirement also eliminates regions of reduced calorimeter thickness (about 9 interaction lengths as compared to the typical 13–18 interaction lengths), and hence reduces punch through background. DØ has a compact inner tracker and gains from reduced π and K decays to muons in flight compared to CDF. Cosmic-ray background is reduced by requiring small impact parameters of the muon track relative to the interaction vertex, and correct drift time relative to the beam crossing. Muons from W and Z decays are expected to be isolated in energy compared to muons associated with jets, such as those produced from heavy-quark decays. The latter are rejected by requiring that the calorimeter energy along the muon track not exceed the expected energy loss by more than 3σ and by requiring that the calorimeter energy surrounding the muon in a cone of radius $\Delta R = 0.6$ be less than 6 GeV.

The W decay muon is required to satisfy all these criteria, as is one of the Z decay muons. The other Z muon is only required to deposit at least 1 GeV in the calorimeter. The efficiency of reconstructing muon tracks in the proportional drift tubes is measured by visually scanning event displays with very loose trigger requirements and no offline reconstruction requirements. Further identification efficiencies are measured from $Z \to \mu^+\mu^-$ events by making stringent cuts on one muon and using the other muon to measure the efficiency. The muon hardware trigger efficiency is determined from jet triggers containing a muon.

TABLE VI. Results and uncertainties in the DØ R measurement from Run 1B, and the CDF R measurement from Run 1A for the electron channel.

	DØ	CDF
R	10.43±0.27	10.90±0.32(stat)±0.29(syst)
Ratio of events	12.43±0.18	
Efficiency ratio	1.108±0.007	1.035±0.016
Acceptance ratio	0.787±0.007	0.835±0.013
NLO electroweak	1.00±0.01	

TABLE VII. Inputs used by CDF and DØ to extract Γ_W from $R=\sigma_W\cdot B(W\to e\nu)/\sigma_z\cdot B(Z\to e^+e^-)$.

	CDF	DØ
σ_W/σ_Z	3.35 ± 0.03	3.362 ± 0.053
$\Gamma(Z)$	2.4969 ± 0.0038 GeV	
$\Gamma(Z\to e^+e^-)$	83.98 ± 0.18 MeV	
$B(Z\to e^+e^-)$		0.03367 ± 0.00006
$\Gamma(W\to e\nu)$	225.9 ± 0.9 MeV	227.0 ± 1.1 MeV

The detector acceptance for W and Z events is determined from a full detector simulation based on GEANT, with ISAJET as the parton-level event generator. Backgrounds arise from muons associated with jets, cosmic rays, and random proportional drift tube hits, as well as from $W\to\tau\nu$, $Z\to l^+l^-$, and $Z\to\tau^+\tau^-$ sources. The jet background is determined by analyzing the distribution of isolation energy. Cosmic-ray and combinatorial backgrounds are estimated from the drift time distribution. Punchthrough and decays in flight are negligible. The $W\to\tau\nu$, $Z\to l^+l^-$, and $Z\to\tau^+\tau^-$ backgrounds are estimated from Monte Carlo models. Table V shows the results and the SM predictions.

3. Extraction of $B(W\to l\nu)$ and $\Gamma(W)$

Table VII shows the values of the production cross-section ratio, the Z total width, and the leptonic width from LEP used to extract the W leptonic branching ratio. CDF extracts $B(W\to e\nu)=0.1094\pm0.0033(\text{stat})\pm0.0031(\text{syst})$ and $\Gamma(W)=2.064\pm0.0060(\text{stat})\pm0.059(\text{syst})$. Using the SM prediction for $B(W\to l\nu)$ as a function of the top-quark mass m_t, CDF extracted a 95% C.L. limit $m_t>62$ GeV. This limit is independent of top-quark decay modes and only assumes the W coupling to $t\bar{b}$.

DØ extracts from the Run 1B data

$$B(W\to e\nu)=0.1044\pm0.0015(\text{stat})\pm0.0020(\text{syst})\pm0.0017(\text{other})\pm0.0010(\text{next-to-leading order}) \text{ and}$$

$$\Gamma(W)=2.169\pm0.031(\text{stat})\pm0.042(\text{syst})\pm0.041(\text{other})\pm0.022(\text{next-to-leading order}) \text{ GeV},$$

where the third source of uncertainty is uncertainties in the LEP input and the theoretical cross-section ratio. The fourth source of uncertainty is next-to-leading-order electroweak radiative corrections. DØ has also combined their results from Run 1A and Run 1B. The electron channel measurements are mostly uncorrelated. Only the acceptance, the Drell-Yan correction, and the next-to-leading-order electroweak correction uncertainties are correlated. The measurements in the electron and muon channels are uncorrelated. The combined DØ result is $R=10.51\pm0.25$ and $\Gamma(W)=2.152\pm0.066$ GeV. Comparing this to the SM prediction of $\Gamma(W)=2.094\pm0.006$ GeV, DØ extracts the 95% C.L. upper limit of 191 MeV on the W partial width for nonstandard-model final states.

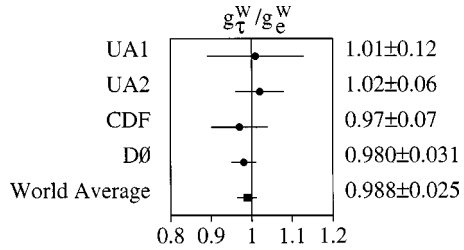

FIG. 19. Results on $\tau-e$ universality at $Q^2=M_W^2$ from hadron colliders.

4. τ measurement

$W\to\tau\nu$ decays are identified using the hadronic decays of the τ, which result in a narrow, isolated, low-multiplicity jet, and $\not\!\!E_T$. CDF has used charged-particle tracking to identify the τ decay, while DØ has used the fine granularity of the calorimeter. Based on 1202 candidate events and an estimated total background of 222 ± 17 events, DØ measures $g_\tau/g_e=0.980\pm0.020(\text{stat})\pm0.024(\text{syst})$, consistent with $\tau-e$ universality. Phase-space effects and nonuniversal radiative corrections are negligible. Figure 19 shows a summary of recent results (Albajar *et al.*, 1989, 1991; Alitti *et al.*, 1992d; Abe *et al.*, 1992b; Abbott *et al.*, 2000e).

D. Lepton charge asymmetry

The W asymmetry is measured by CDF (Abe *et al.*, 1992a, 1995d, 1998c) by counting the number of positively and negatively charged leptons as a function of lepton rapidity and constructing the asymmetry as

$$A(y_l)=\frac{d\sigma^+/dy_l-d\sigma^-/dy_l}{d\sigma^+/dy_l+d\sigma^-/dy_l}, \tag{25}$$

where $d\sigma$ is the cross section for W decays as a function of lepton rapidity. Since the difference in efficiencies between the l^- and l^+ is typically very small, its contribution to the systematic uncertainty in the ratio is also very small. In addition, *CP* invariance implies that the asymmetry is an antisymmetric function of rapidity, thereby allowing the positive and negative rapidity regions to be combined, further reducing systematic uncertainties due to efficiencies.

Events are collected using the typical criteria for W decays to leptons. The lepton rapidity range in accepted events extends to $|y_l|<2{:}5$, with muons contributing in the regions $|y_\mu|<1.1$ and $1.9<|y_\mu|<2.5$, and electrons contributing in the region $|y_e|<2.4$. The high-rapidity muon region, which uses the forward toroidal muon detectors, is a departure from more typical CDF W analyses. The electron contribution likewise makes use of higher-rapidity end-plug regions due to the development of an alternative method of charge determination. The silicon vertex detector is used to complement the track-

TABLE VIII. Background fractions in the $W \to e\nu$ charge asymmetry data samples.

Sample	$W \to \tau\nu$	QCD dijets	$Z \to l^+l^-$
Central e(%)	2.0±0.2	0.7±0.2	<0.2
Central μ(%)	2.0±0.2	0.6±0.2	4.7±0.7
Plug-SVX e(%)	2.0±0.2	1.6±0.3	<0.2
Plug-CTC e(%)	2.0±0.2	2.4±0.6	<0.2
Forward μ[a](%)	2.0±0.2	4±2	6.5±0.6

[a]There is also a 4% background from low-momentum muons reconstructed as high-momentum muons in the Forward μ data.

ing chamber for tracks with $|y| > \sim 1$. In this region, the tracking chamber efficiency and resolution degrade with increasing rapidity up to 1.8, which is the extent of the tracking chamber coverage. Beyond this, the silicon vertex detector measurement of the electron trajectory, combined with the position of the electromagnetic shower in the calorimeter, provides the charge determination.

The key pieces of information in this measurement are the charge and rapidity of the lepton. Thus most of the systematic uncertainties concentrate on how well the charge is determined. Trigger efficiency dependences on E_T or charge are investigated and found to be negligible with the exception of electron triggers in the end-plug calorimeter region, which have an E_T dependence. A correction for this dependence is applied to the asymmetry, where it varies with rapidity but is always less than 0.005 (compared to the average statistical uncertainty of 0.015). The event selection criteria are also checked for charge-dependent biases using clean W and Z events; none are found. The charge misidentification rate for low-rapidity muons is determined to be negligible; for high-rapidity muons the rate is found to be less than 1%. The charge misidentification rate for low-rapidity (central) electrons is measured using Z events in which both electrons have the same charge. Errors in the charge determination of central electrons are caused by overlap with electron pairs produced from a bremsstrahlung photon radiated from the W decay electron. These three electrons are colinear, which confuses the pattern recognition in the tracking chamber. For high-rapidity electrons, charge misidentification is determined from the tails of the silicon vertex detector charge measurement. The misidentification rates range from 0.2% in the central region to 10% in the highest rapidity bin. Since the charge asymmetry is diluted by picking the wrong sign, it is corrected for these misidentification rates as a function of rapidity.

The backgrounds in this analysis are the same as for most other W analyses; however, here the interest is in the charge symmetry of the background. Table VIII lists the various backgrounds by decay mode and detector region. In forward electron events, misidentified dijet events compose the largest background. This background is charge symmetric, which dilutes the asymmetry. Central electron events suffer mostly from $W \to \tau\nu \to e\nu\bar{\nu}\nu$, which is not a charge-symmetric background since it originated from a W decay. The dominant background for central muons is due to unreconstructed Z events in which one muon is at large rapidity and escapes the tracking chamber. The backgrounds in high-rapidity muon events are larger and are split between unreconstructed Z events, misidentified dijets, and low-momentum muons that are measured as high-momentum muons due to the presence of noise hits. The W asymmetry is corrected for all these backgrounds as a function of rapidity.

Figure 20 shows the folded asymmetry distribution overlayed with predictions of the asymmetry using a variety of parton distribution functions. The functions are generated using the DYRAD (Giele *et al.*, 1993) next-to-leading-order QCD generator. The fits by the MRS-R2 Collaboration (Martin, Roberts, and Stirling 1996) and CTEQ-3M Collaboration (Lai, 1995) include roughly 20% of the full W asymmetry data set. Notice that while these fit well at low values of rapidity, they have large discrepancies at high rapidities. Reanalysis (Yang *et al.*, 1998) of the data of the NMC Collaboration (Arneodo *et al.*, 1997) leads to a modification of the d/u ratio and a new fit, the MRS-R2 modified curve, which agrees much better overall. Recent global parton distribution function fits (including all these data) resulted in the MRST (Martin, Roberts, Stirling, and Thorne, 1998) set of parton distribution functions, which also agrees quite well.

At large rapidity, the W asymmetry is influenced by the p_T^W spectrum. Since DYRAD does not accurately reproduce the p_T^W spectrum at low p_T, another Monte

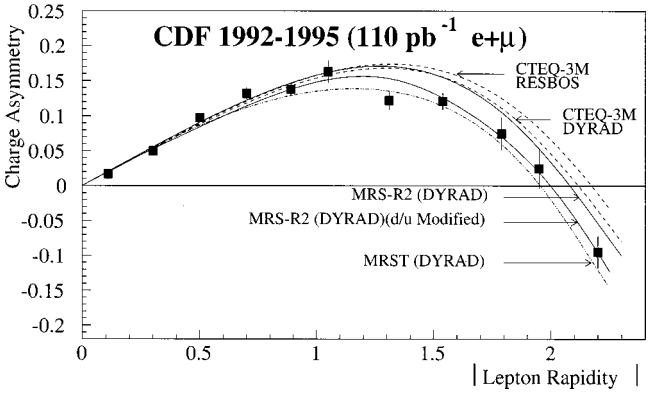

FIG. 20. The CDF lepton charge asymmetry vs lepton rapidity. The negative rapidity region has been combined with the positive region. See the text for an explanation of the curves.

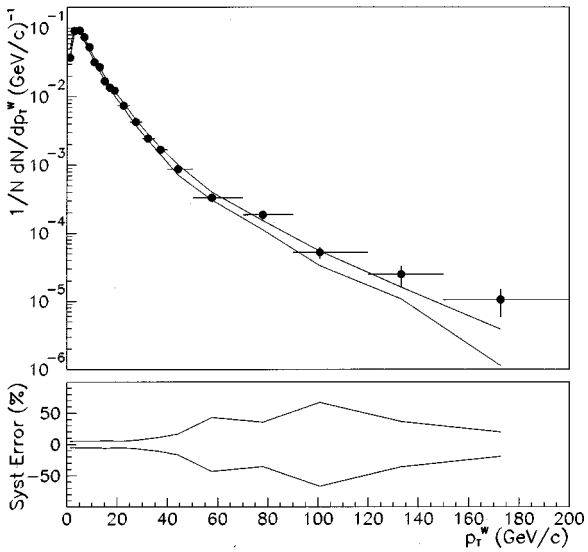

FIG. 21. The DØ measurement of the p_T^W spectrum (●). The error bars show the statistical uncertainty. The two lines show the theoretical calculation by Arnold and Kauffman, smeared for detector resolution, with $\pm 1\sigma$ variation of the detector modeling parameters. The fractional systematic uncertainty on the data is shown as the band in the lower plot.

Carlo program is used to cross-check the DYRAD calculation. The RESBOS generator (Balazs and Yuan, 1997) includes soft-gluon resummation at all orders of perturbation theory, and since soft gluons are mainly responsible for the low end of the p_T^W distribution, it should be a good test of the DYRAD results. Using the parton distribution functions of the CTEQ3M Collaboration, one finds that the two generators agree in the low-rapidity region, but are slightly different in the high-rapidity region, where one expects differences (see Fig. 20).

These results demonstrate that the *W* asymmetry is a sensitive and unique probe of the d/u ratio and contributes significantly to parton distribution fits.

E. Transverse momentum and jets

QCD studies of *W* and *Z* production properties have typically been performed in two ways: (i) measuring the kinematics of the *W* and *Z* inclusively, without measuring the details of the hadronic recoil, and (ii) characterizing the hadronic recoil in terms of the identified jets and associating these jets with hard partons. We discuss measurements made by CDF and DØ using both approaches.

1. *W* and *Z* boson transverse momentum

DØ has measured the shape of the p_T^W distribution from the Run 1A data using the $W \to e\nu$ channel (Abbott *et al.*, 1998e). Electrons are accepted in the central calorimeter only to keep the background contamination from multijet events at a reasonable level at high values of p_T^W. The electron and event selection criteria are similar to those discussed earlier in other measurements.

The trigger and selection efficiencies are determined using $Z \to e^+e^-$ data. No dependence of these efficiencies on p_T^W is found within an accuracy of 5%. A parametric Monte Carlo detector simulation, similar to the one used for the *W* mass and cross-section measurements, is used to compare the theoretical predictions to the data. This procedure is preferred to unsmearing the data (i.e., correcting the data for resolution effects) because of the rapid variation in the dN/dp_T^W distribution near the origin. Since the resolution on the hadronic recoil (~5 GeV) is of the same order of magnitude as the location of the peak in dN/dp_T^W (at ~4 GeV; see Fig. 21), the unsmearing correction is very sensitive to the prior assumption of the true p_T^W distribution at low p_T^W. Hence smearing corrections are not applied to the data, rather the detector effects are folded into the predictions before comparing to the data.

The largest source of background in the $W \to e\nu$ candidates are QCD multijet events. As p_T^W increases, the distinctive *W* event signature is spoiled and the multijet background increases. The background is measured in the same p_T^W bins used for the differential cross section. The amount of multijet background in the p_T^W bins of 0–30, 30–60, and >60 GeV was estimated to be (2.9 ± 1.6), (20.9 ± 11.7), and $(38.3 \pm 21.5)\%$, respectively. Additional backgrounds from top-quark decays and $Z \to e^+e^-$ events are less than 5%. As a cross check, the m_T and $\not\!\!E_T$ distributions in these bins are compared to the sum of signal prediction from the Monte Carlo simulation and expected background; good agreement is found. The background-subtracted data are compared to the theoretical prediction with detector simulation in Fig. 21. The agreement is good over the entire p_T range.

The p_T^W distribution provides a high-statistics measurement at high p_T. At low p_T the measurement is limited by the resolution on the hadronic recoil. The measurement of p_T^Z using the decay charged leptons is complementary because it provides a more precise measurement at low p_T. In this region the QCD resummation formulation is more relevant, and at very low p_T there are nonperturbative contributions which are important to understand for the *W* mass measurement.

CDF (Affolder *et al.*, 2000c) and DØ (Abbott *et al.*, 2000a, 2000d) have both measured the p_T^Z distribution using the $Z \to e^+e^-$ events. One electron is required to be central while the second electron can be central or forward. The p_T^Z dependence of the electron identification efficiency is more important in this case than the p_T^W measurement because there are two electrons. As p_T increases, the hadronic recoil is more likely to spoil the isolation of at least one electron, thus causing loss of *Z*-finding efficiency. At high values of p_T^Z both electrons are boosted away from the recoil, and the *Z*-finding efficiency recovers. At $p_T \sim 40$ GeV, the relative loss peaks at about 8%. The background fraction in each p_T^Z bin is determined from a fit to the *Z* peak and sidebands with a combination of signal and background shapes.

The resolution corrections are important at low p_T^Z and are well understood. DØ reports the resolution cor-

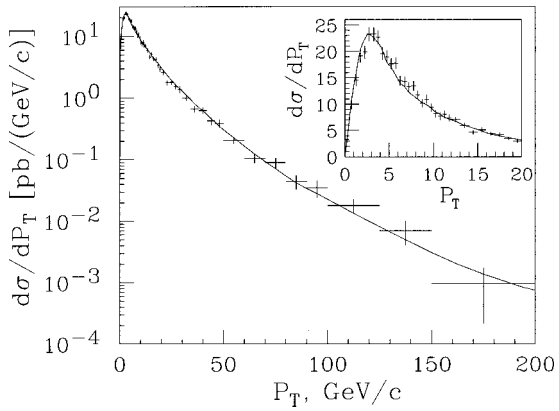

FIG. 22. The CDF measurement of the p_T^Z spectrum of e^+e^- pairs in the mass range 66–116 GeV (Affolder *et al.*, 2000c). The inset shows the $p_T<20$ GeV region on a linear scale. The crosses are the data with all errors included except the 3.9% luminosity error. The curve is the *Z*-only RESBOS prediction with the cross section normalized to 248 pb.

rection in the $0<p_T^Z<1$ GeV range to be 18.5%, decreasing to <5% above 5 GeV. CDF reports the uncertainty on the correction to be 3.6% at $p_T^Z=0$ GeV, decreasing to 0.6% for $p_T^Z>20$ GeV.

Figures 22 and 23 show the fully corrected p_T^Z distribution from CDF and DØ. CDF has compared their measurement to the EV (Ellis and Veseli, 1998) and RESBOS calculations, which combine the perturbative QCD calculation at high p_T with QCD resummed calculations and nonperturbative form factors at low and very low p_T. DØ has made similar comparisons and also comparisons to purely perturbative $\mathcal{O}(\alpha_s^2)$ calculations. The comparisons confirm the need for the QCD resummation formulation and the nonperturbative form factor at low p_T. DØ has fit their measurement to extract the g_1, g_2, and g_3 parameters of the Ladinsky-Yuan parametrization [see Eq. (20)] of the nonperturbative form factor. The fitted values are consistent with the values extracted from fits to low-energy Drell-Yan data, and the

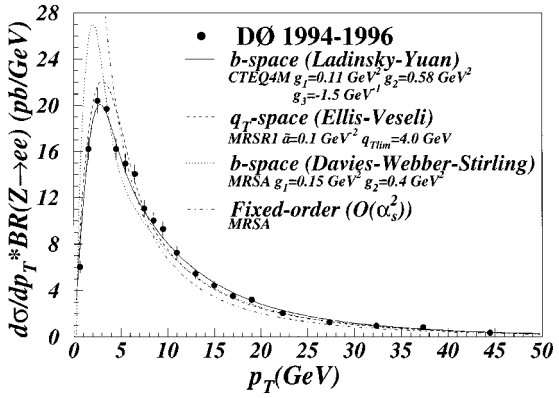

FIG. 23. The DØ measurement (see Abbott *et al.*, 2000a, 2000d and references therein) of the p_T^Z spectrum (●), compared with theoretical calculations using resummation techniques and nonperturbative parametrizations as well as a fixed-order calculation.

g_2 fitted value is considerably more precise than previous determinations.

2. Properties of *W* and *Z* boson+jet events

CDF and DØ have measured the properties of jets accompanying *W* and *Z* bosons (Abe *et al.*, 1994, 1997b; Abachi *et al.*, 1995d; Abbott *et al.*, 1999d). The details of the corrections applied to jets are described in Abe *et al.* (1993) and Abbott *et al.* (1999c). The CDF measurement of the $W+$jets events is made from the data collected during Run 1. The jets are reconstructed in the $W\to e\nu$ events using the cone algorithm with radius $\Delta R=0.4$. The parton energy deposited outside the cone and the energy contaminating the cone from the underlying event are corrected for. Jets are counted with $E_T>15$ GeV and $|\eta|<2.4$, and events that have a jet within $\Delta R=0.52$ of the lepton are rejected. The latter requirement ensures that the jets are well separated from the electron (the cone algorithm differentiates well when the separation exceeds 1.3 times the cone radius).

The jet multiplicities are corrected for jets produced in additional $p\bar{p}$ interactions. The main background is from QCD multijet contamination and is measured with a sample obtained by removing the electron isolation and $\not\!\!E_T$ requirements and then extrapolating from the multijet-dominated region into the *W* signal region in $\not\!\!E_T$. The multijet background ranges from $(2.9\pm0.9)\%$ for the $\geqslant 0$ jet sample to $(27\pm11)\%$ for the $\geqslant 4$ jet sample.

The systematic uncertainties on jet counting are determined by varying the jet energy by ±5%, varying the jet η by ±0.2, varying the probability for extra jets from additional $p\bar{p}$ interactions by a factor of 2 (the probability for the presence of one extra jet is 1% and reduces by a factor of 6 for each additional jet), and varying the correction for energy contamination in the jet cone by ±50% (±0.5 GeV on average). The combined uncertainty ranges from 10% for the $\geqslant 1$ jet sample to 30% for the $\geqslant 4$ jet sample.

The final correction to the number of $W\to e\nu+\geqslant n$ jet candidates includes the overall efficiency of identifying $W\to e\nu$ decays, including the acceptance, electron-jet overlap efficiency, and efficiency of online trigger and offline identification. The overlap efficiency is calculated from the data by taking $Z\to e^+e^-$ events and replacing the $Z\to e^+e^-$ decay with a simulated $W\to e\nu$ decay, preserving the boson p_T.

The data are compared with leading-order perturbative QCD calculations performed with the VECBOS (Berends *et al.*, 1991) program. Initial-state gluon radiation, final-state parton fragmentation, and hadronization are performed by interfacing VECBOS to the HERWIG Monte Carlo program, with subsequent full detector simulation. HERWIG parton showers represent partial higher-order corrections to the leading-order VECBOS calculation, which CDF refers to as enhanced leading-order (ELO). CDF compares the $W+n$ jet cross sections to the ELO predictions with variation of renormalization scale and finds agreement for $n=2-4$ (see Fig.

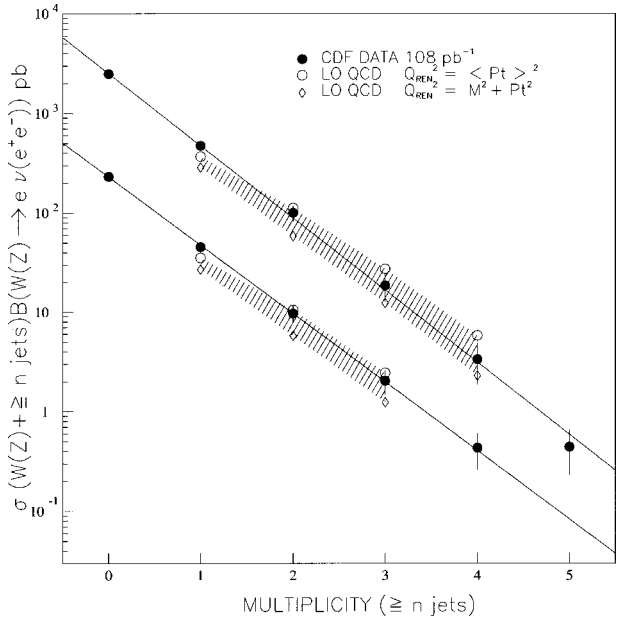

FIG. 24. The CDF measurement of cross sections vs inclusive jet multiplicity: top, for $W+n$ jets; bottom, for $Z+n$ jets. The lines are exponential fits to the data. The theory is shown as a shaded band which represents the uncertainty due to the renormalization scale. The 0 jet prediction is the Born-level calculation for W production.

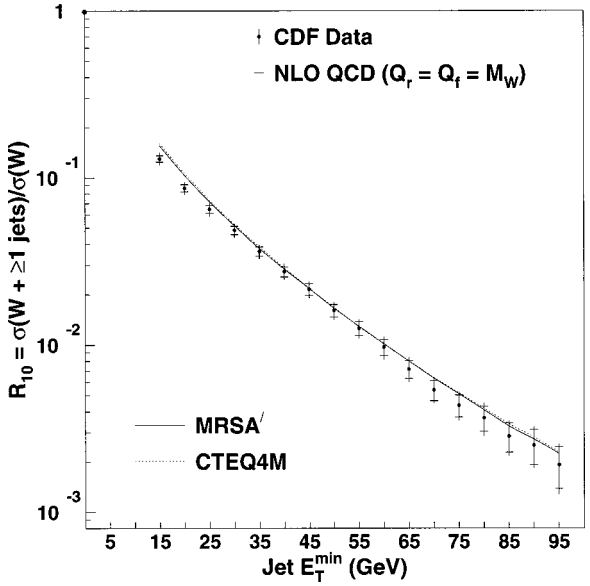

FIG. 25. The CDF measurement (see Abbott *et al.*, 1999c, and references therein) of R_{10} vs jet E_T^{min}, compared to the next-to-leading-order QCD predictions calculated using the MRSA′ and CTEQ4M parton distribution functions. The inner error bars include statistical uncertainties only; the outer error bars include both statistical and systematic uncertainties. The R_{10} measurements at each value of E_T^{min} are statistically correlated because the corresponding event samples are not independent.

24). The distributions of jet E_T, dijet mass, and angular separation are also reasonably well described by the calculations. The statistics of the $W\to e\nu$ data are large enough to show some limitations of the ELO predictions.

Another technique of comparing data to QCD calculations is to measure the ratio of cross sections of inclusive jet production in W events to the total W cross section. CDF and DØ have made measurements of the ratio $R_{10}\equiv\sigma(W+\geq 1\text{ jet})/\sigma(W)$. This ratio can be compared to next-to-leading-order QCD predictions as a function of the jet E_T threshold E_T^{min}. The measurements have been made in the $W\to e\nu$ channel. Measuring the ratio takes advantage of the cancellation of the integrated luminosity uncertainty and the reduction of other systematic uncertainties.

The CDF measurements are made from the Run 1 data using the same criteria and algorithms as used for the $W+n$ jet cross-section measurements. Results are reported for the jet E_T^{min} varied between 15 GeV and 95 GeV. The acceptance, efficiency, and backgrounds are estimated for each value of E_T^{min}. The acceptance, calculated using the VECBOS generator and the CDF detector simulation, increases with E_T^{min} from 24 to 36 % for $W+\geq 1$ jet events. The acceptance for inclusive W events is $(23.9\pm 0.5)\%$.

The main source of background is QCD multijet production, which increases with E_T^{min} from 13 to 28 %. Other backgrounds include $W\to\tau\nu\to e\nu\bar{\nu}\nu$, $Z\to e^+e^-$, $Z\to\tau^+\tau^-$, top decays, $W\gamma$, and jets from additional $p\bar{p}$ interactions. The total background increases with E_T^{min} from (22 ± 5) to $(44\pm 13)\%$.

The jet energy scale uncertainty is one of the large systematic uncertainties on R_{10}, increasing from 5 to 11% as a function of E_T^{min}. The overall systematic uncertainty increases from 8 to 19 %.

The measured values of R_{10} are compared to perturbative next-to-leading-order QCD predictions generated using the DYRAD Monte Carlo program, which calculates inclusive W production at order α_s and $W+\geq 1$ jet at order α_s^2. The renormalization and factorization scales are set equal to the W mass. Partons with $\Delta R < 0.52$ are merged vectorially to form jets which are then smeared in E_T, η, and ϕ to model detector resolution effects. Monte Carlo events with at least one jet with $E_T > E_T^{min}$ and $|\eta| < 2.4$ are used to compute R_{10} for the theory.

Figure 25 shows the measured and predicted values of R_{10} as a function of E_T^{min}. Data and theory agree well for $E_T^{min} > 25$ GeV. At low E_T^{min}, the matrix element calculation diverges and does not include soft-gluon effects.

Since the data are not corrected for QCD out-of-cone showering, the measured R_{10} depends on the cone size. The next-to-leading-order calculation approximates the jet shape by producing up to two final-state partons. The agreement between data and theory depends on how well the jet shape is reproduced by the theory. The effect of changing the parton clustering algorithm is found to be small. The next-to-leading-order predictions are found to be much less sensitive to changes in the factorization and renormalization scales than leading-order predictions: a factor-of-2 variation in the scales changes

TABLE IX. Summary of the CDF and DØ $W' \to l\nu$ searches. The DØ search in the $(M_{W'}, M_\nu)$ plane (see Sec. V.F.2) from Run 1B yields the best limit $M_{W'}(95\%\ \text{C.L.}) > 720\,\text{GeV}$ for a light ν.

	CDF $W' \to \mu\nu$	CDF $W' \to e\nu$	DØ $W' \to e\nu$
N_{obs}	31992	10534	9135
$\int L(\text{pb}^{-1})$	107	19.7	13.9
$N_{obs}(m_T > 150\,\text{GeV})$			16
$N'_{bkg}(m_T > 150\,\text{GeV})$			19.7 ± 5.7
$N_{obs}(m_T > 200\,\text{GeV})$	14	5	
$N'_{bkg}(m_T > 200\,\text{GeV})$	11.8 ± 0.9	7	
$M_{W'}(95\%\ \text{C.L.})$ limit	660 GeV	652 GeV	610 GeV

R_{10} by 5% at next-to-leading order and 15% at leading order.

The data are compared to theory predictions for various input values of $\alpha_s(M_Z)$. There is agreement for $\alpha_s(M_Z)$ values between 0.105 and 0.130. The sensitivity of the predicted R_{10} to α_s is not large enough to permit an extraction of α_s from the current measurements. DØ performed the same measurement with the Run 1A data, with a jet cone radius of 0.7 and $E_T^{min} = 25\,\text{GeV}$. The DØ measurement of R_{10} is one standard deviation higher than the prediction (Abachi *et al.*, 1995d).

DØ has performed an analysis of QCD color coherence effects in *W* events with at least one jet (Abbott *et al.*, 1999d). In this analysis one observes initial-to-final state coherence effects by comparing the soft-particle angular distributions around the colorless *W* boson and the opposing jet in the same event. The fine granularity of the calorimeter is also exploited. The ratio of the tower multiplicity around the jet to the tower multiplicity around the *W* boson in an annulus of $0.7 < R < 1.5$, as a function of angle around the annulus, provides a direct measure of color coherence effects. The signal is consistent with Monte Carlo predictions when coherence effects (angular-ordered parton showers with string fragmentation) are included, and with an analytic modified-LLA perturbative calculation based on local parton-hadron duality.

F. Heavy and right-handed *W* bosons

Heavy right-handed gauge bosons have been sought in the $l\nu$ and *eejj* channels. In $l\nu$ searches, one assumes that right-handed neutrinos from the $W_R \to l_R \nu_R$ process will be light ($M_{\nu_R} \ll M_{W_R}$). These searches do not distinguish between left-handed and right-handed *W* decay topologies and are referred to as heavy-W' boson searches. Previous direct searches for $W' \to l\nu$ decays in $p\bar{p}$ experiments (Ansari *et al.*, 1987a; Albajar *et al.*, 1989) had set a lower limit for the mass of the W' of 220 GeV at 90% C.L. A CDF search using Run 0 data (Abe *et al.*, 1991c) measured $M_{W'} > 520\,\text{GeV}$ at 95% C.L.

In *eejj* searches, one makes definite assumptions about the subsequent decay of the ν_R, which depends on the mixing between the right- and left-handed gauge bosons. For minimal mixing, the ν_R decays into an electron and an off-shell W_R^*, which in turn has only the $q\bar{q}'$ channel open assuming that the electron ν_R is the lightest among the right-handed neutrinos. For large mixing, the ν_R preferably decays into an electron and a left-handed *W*, which goes into $q\bar{q}'$ in two-thirds of the cases. In both scenarios, the most abundant final state involves two electrons and two jets coming from the quarks. The only previous W_R direct search at hadron colliders was performed by the UA2 Collaboration (Alitti *et al.*, 1993) and resulted in a lower limit, $M_{W_R} > 261\,\text{GeV}$, for any value of the ν_R mass.

Indirect limits on the W_R mass can be inferred from low-energy phenomena like deviations of the *V-A* angular distribution in polarized muon decays, measured differences between the K_S and K_L masses, and neutrinoless nuclear double beta decay. The above limits are combined to exclude a heavy W_R boson below 1.3 TeV (Langacker, 1989). Cosmological constraints (Olive *et al.*, 1981; Raffelt and Seckel, 1988; Barbieri and Mohapatra 1989) have established limits of $\mathcal{O}(1\text{–}10)$ TeV assuming very low neutrino masses ($M_{\nu_R} < 1\text{–}10\,\text{MeV}$).

1. Search for heavy W' bosons

Both CDF (Abe *et al.*, 1995f) and DØ (Abachi *et al.*, 1995a) have pursued helicity-independent searches for direct production of W' in the electron channel using Run 1A data. They assume that the W' has standard couplings to fermions, that the $W'WZ$ coupling is suppressed, and that the neutrinos are light, noninteracting, and stable. DØ allows events coming from $W' \to \tau\nu \to e\nu\nu$ in the signal definition. CDF has also searched for W' production in the muon channel using the full Run 1 sample (Abe *et al.*, 1999a). In all of these analyses the m_T distribution is searched for evidence of a Jacobian peak above the *W* mass peak. The limits on the production and decay rates of such a massive object are usually calculated relative to the production and decay rate of the standard-model *W* boson, thus avoiding many of the uncertainties associated with an absolute measurement. The DØ search (Abachi *et al.*, 1996a) described in the next section produced the best limit on a heavy charged gauge boson.

Table IX shows the number of $l\nu$ events selected by the above searches with requirements analogous to the

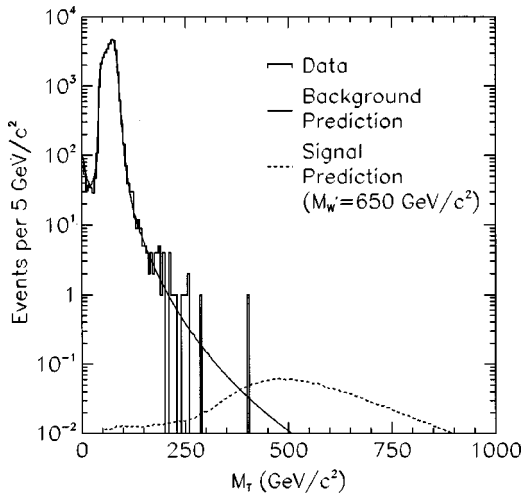

FIG. 26. Transverse mass spectrum in the CDF $W' \to \mu\nu$ search. The background fit (solid line) is superimposed on the data (histogram). The signal (dashed line) expected for a W' with a mass of 650 GeV is also shown.

W mass analysis. Background sources other than SM leptonic W decays come from $W \to \tau\nu$, $Z/\gamma \to ll$, $Z/\gamma \to \tau\tau$, and QCD dijet events in which one jet fakes an electron or a muon and the second is poorly measured, giving rise to substantial $\not\!\!E_T$. The shape of the first three sources is extracted from Monte Carlo simulations, while their size is determined using measured production rates and branching fractions to these final states. The QCD background contribution is estimated directly from the data. Figure 26 shows the transverse mass distribution for the CDF $W' \to \mu\upsilon$ selected sample. Superimposed is the unbinned maximum-likelihood fit to the m_T distribution between 40 and 2000 GeV assuming only contributions from left-handed $W \to \mu\nu$ decays and from the other known background sources. There is good agreement over the whole spectrum and no excess is observed in the high-m_T region to indicate the presence of $W' \to \mu\nu$ decays. The same qualitative agreement is found for the $W' \to e\nu$ searches, as shown by the number of observed versus expected events in the high-m_T region presented in Table IX.

The $q\bar{q} \to W'$ production is simulated using leading-order or next-to-leading-order generators with parton distribution functions from the MRS-D′ Collaboration (Martin *et al.*, 1993) or CTEQ 4A1 Collaboration (Lai, 1997) for the electron and muon decay channels, respectively. Whenever a leading-order generator is used, higher-order diagrams for W' production are taken into account by modeling the p_T of the W' at production according to the measured W spectrum. To extract a limit on the mass of the heavy boson, the kinematic and geometric acceptance for the signal is estimated as a function of $M_{W'}$ after passing the generated W' events through the detector simulation.

The limit on the relative contribution of a W' is obtained by fitting the data distribution to the sum of the background, including $W \to l\nu$, and the m_T distribution expected for a W' of a given mass. The resulting likelihood function is used to set a 95% C.L. upper limit on the ratio of W' candidates to the SM contribution. The limits are insensitive to the assumed width of the W' since the width is dominated by the detector resolution. Systematics uncertainties in the acceptance, backgrounds, and m_T shape distributions coming from different choices of parton distribution function are incorporated into the probability density functions as Gaussian distributed errors. The 95% C.L. limits shown in Table IX are obtained by plotting the $\sigma(p\bar{p} \to W') \cdot B(W' \to l\nu)$ limit as a function of $M_{W'}$ and finding the point where it intercepts the theoretical curve assuming standard couplings to fermions.

2. Search for right-handed *W* bosons

DØ has performed a direct *eejj* search for W_R bosons with mass greater than 200 GeV, which decay into an electron and a heavy right-handed neutrino ν_R, using Run 1 data (Abachi *et al.*, 1996a).

Two different analyses are performed depending on the ratio $R = M_{\nu_R}/M_{W_R}$. If $R \leqslant 1/2$, the electron transverse energy E_T^e is searched for a Jacobian peak indicative of the presence of the W_R (peak search). If on the other hand $R \geqslant 1/2$, the decay products of the more massive and thus slower ν_R are expected to be well separated, making possible the identification of the two electrons and two jets in the event. A simple counting experiment is then performed after requiring the two electrons to give a mass outside the Z peak, and this is the *eejj* search.

The peak search finds 101 events with $E_T^e > 100\,\text{GeV}$. After modeling backgrounds from large-p_T W and Z events and misidentified QCD dijet events, a simultaneous fit to the E_T^e and m_T distributions is used to extract information on the probability that events coming from W_R decays are in the sample. No evidence of an excess in the high-E_T^e or m_T regions is found. The acceptance for the E_T^e distribution of the signal was calculated for a grid of points in the (M_{W_R}, M_{ν_R}) plane using a Monte Carlo simulation. The 95% C.L. upper limit on the number of W_R events is converted into an upper limit for the $\sigma(p\bar{p} \to W_R) \cdot B(W_R \to e\nu_R)$ by normalizing to the measured σ_W and σ_Z and to the observed number of W and Z events found in the simultaneous fit to the E_T^e and m_T distributions. Since this search looks only at the inclusive high-E_T^e distribution, it is sensitive to both right-handed and left-handed W bosons. The point where the 95% C.L. upper limit $\sigma \cdot B$ curve intersects the theoretical curve for the standard coupling scenario gives a limit on the W' gauge boson of any helicity. For $M_\nu \ll M_{W'}$, the DØ limit is $M_{W'} > 720\,\text{GeV}$, which is the best limit from Run 1.

For the *eejj* search, events with two isolated electrons with $E_T > 25\,\text{GeV}$ and two or more jets with $E_T > 25\,\text{GeV}$ are selected. Of the 22 events passing these cuts, only two survive the requirement that the invariant mass of the two electrons be outside the M_Z peak. These two W_R candidates are consistent with the esti-

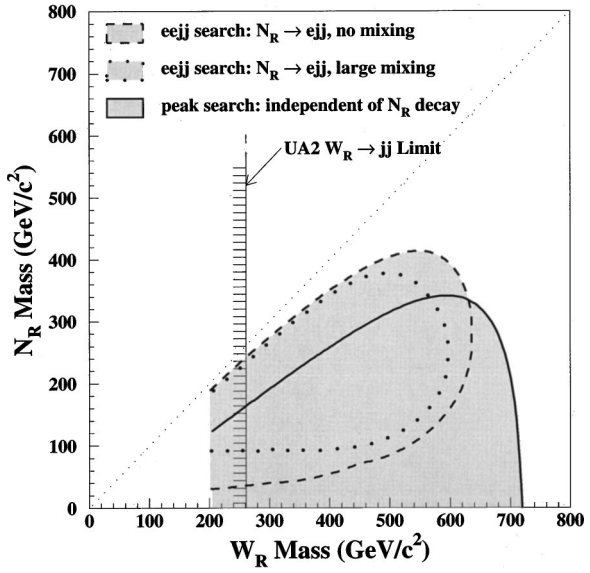

FIG. 27. Excluded regions at 95% C.L. of the M_{W_R} vs M_{ν_R} plane for the DØ W_R searches assuming standard coupling of the W_R to fermions. Also shown is the previous UA2 limit.

mated total background of 3.08 ± 0.78 events obtained from Monte Carlo studies of $Z+$jets, $t\bar{t}$, and QCD events. As for the peak search, the signal acceptance is calculated with the Monte Carlo simulation for a grid of points in the (M_{W_R}, M_{ν_R}) plane for both small and large mixing cases. An upper limit on $\sigma \cdot B$ is obtained using a Bayesian approach (Particle Data Group, 1998, p. 174) with a flat prior distribution. Figure 27 summarizes the results of the DØ searches in terms of the excluded region in the (M_{W_R}, M_{ν_R}) plane.

G. Rare decays

Two rare decays, $W \to \pi\gamma$ and $W \to D_s\gamma$, have been sought at hadron colliders. The former has a predicted decay branching fraction of $\sim 3 \times 10^{-8}$ while the latter has a predicted branching fraction of $\sim 1 \times 10^{-7}$ (Arnellos *et al.*, 1982). These decay rates are about six orders of magnitude smaller than the leptonic decay rates.

1. $W \to \pi\gamma$

The upper limit on the decay rate for $W \to \pi\gamma$ has been measured by CDF, UA2, and UA1 (Albajar *et al.*, 1990; Abe *et al.*, 1992c, 1996a, 1998a; Alitti *et al.*, 1992c). This section describes the most recent CDF measurement from Run 1B.

A $W \to \pi\gamma$ event is characterized by a high-E_T photon and a high-p_T pion. The pion appears as a high-E_T jet with a single high-p_T track pointing to the jet. Background events are predominantly QCD direct-photon events (a photon back-to-back with a quark/gluon) in which the jet fragmentation process produces a single charged pion.

The trigger selects events with photon candidates with $E_T > 23$ GeV. The results are corrected for the photon trigger efficiency. The offline analysis consists of two paths: one that selects photons and one that selects pion candidates. The photon candidate shower shape is required to be consistent with shower shapes measured in test-beam data. The shower should be isolated from neighboring energy deposits by requiring less than 4 GeV in a cone of $\Delta R = 0.7$ around the photon. The photon direction is reconstructed from the position of the shower and the location of the event vertex.

The pion search looks for jets with a single high-p_T track pointing in the direction of the jet. Both the jet and the associated track are required to have $E_T > 15$ GeV. The track is required to be isolated, with no other tracks having $p_T > 1$ GeV in a cone of $\Delta R = 0.7$ around the pion candidate track. The hadronic calorimeter is required to contribute more than 20% to the total energy of the jet. To further correlate the track with the jet, the charge fraction, which is the ratio of track p_T to jet E_T, must be greater than 1.0.

The pion track and the photon must be separated in ϕ by more than 1.5 radians to remove accidental overlaps between, say, a jet and an electron from a W leptonic decay. A candidate sample of 28 events remains after adding a final requirement that there be no other jets with $E_T > 15$ GeV. Three of these 28 events are within the W pole region defined as three times the mass resolution (± 8.7 GeV).

Leptonic $W \to e\nu$ decay events are used to determine selection efficiencies. $W \to e\nu$ events are selected from the single-track jet data comprising the first element of the pion search. An additional requirement that the jet contain at least 15 GeV of electromagnetic energy almost exclusively selects $W \to e\nu$ events. The neutrino momentum in these events is computed from the electron momentum, $\not{E}_T$, and the W mass. There are in general two solutions, either of which may be unphysical and not used. If both are valid, the choice is made by the fiducial requirement of $|\eta(\nu)| < 1.1$ or random selection if both satisfy the fiducial cut.

Using the $W \to e\nu$ events, one determines the photon shower shape efficiencies from the electron shower shapes and compares them to Monte Carlo simulations. A systematic uncertainty is assigned to account for data–Monte Carlo differences and to allow for electron brehmsstrahlung. The photon isolation-cut efficiency is measured using an isolation cut around the neutrino direction, with a systematic uncertainty reflecting the differences between isolation around the neutrino and around the electron. An embedded simulated pion with the same momentum as the neutrino is used to determine the jet electromagnetic fraction and charged fraction pion selection efficiencies. Again, differences between data and Monte Carlo simulation contribute systematic uncertainties. Here, as in the photon case, the isolation efficiency is determined by looking at the isolation around the neutrino. The overall efficiency times acceptance is taken from a Monte Carlo model and scaled by the difference between the Monte Carlo and the data. It amounts to 0.038 ± 0.005 with the bulk of the losses coming from geometric acceptance.

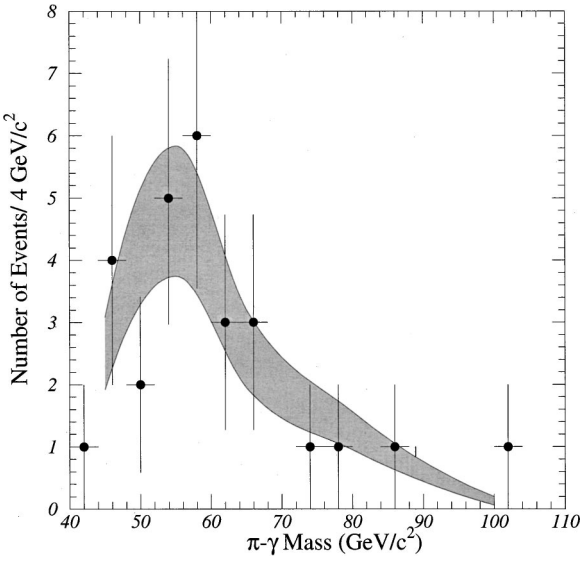

FIG. 28. The $\pi\gamma$ invariant-mass distribution from CDF. The shaded region is the expected distribution from backgrounds.

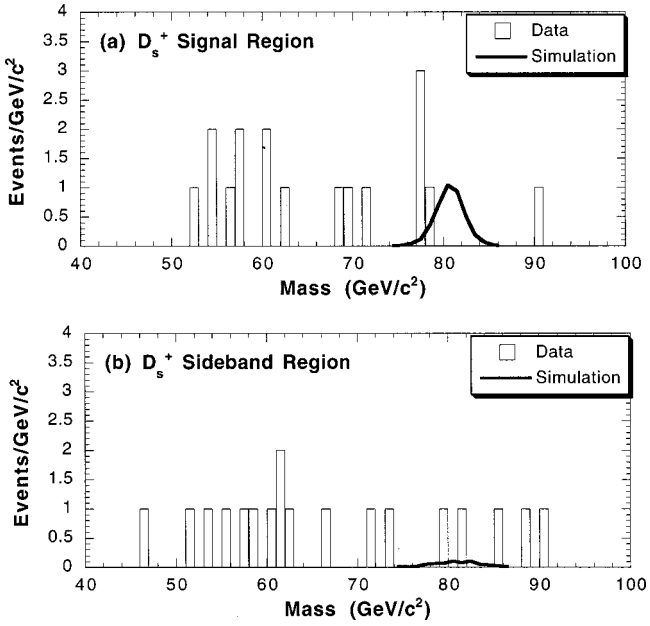

FIG. 29. The CDF invariant-mass distributions for signal and sideband regions. The curve is the $W\to D_s\gamma$ Monte Carlo simulation normalized to four signal events.

The dominant direct-photon background is estimated from the data by relaxing the single-track cut and instead requiring at least three tracks whose net charge is ± 1. The summed momentum of the tracks (those with $p_T > 1$ GeV) is used in the charged-fraction criterion. The number of events observed is found to be a linear function of the number of tracks in the momentum sum. Thus, extrapolating to one track determines the number of background events. This extrapolation is carried out for both the 3σ mass region around the W mass and elsewhere (from 40 to 110 GeV). The extrapolated numbers are scaled such that the number of background events in the regions excluding the W mass region agree with the 25 observed events. The number of background events expected in the W signal region is 5.2 ± 1.5, to be compared with three observed events (see Fig. 28).

From these numbers a limit of $\sigma\cdot B(W\to\pi\gamma) \leq 1.7$ pb is obtained at the 95% confidence level, or alternatively $\Gamma(W\to\pi\gamma)/\Gamma(W\to e\nu)\leq 7\times 10^{-4}$.

2. $W\to D_s\gamma$

The decay rate for $W\to D_s\gamma$ is expected to be about a factor of 3 larger than the decay rate for $W\to\pi\gamma$, but because the D_s has a large number of decay modes, and only a small number are open to experimental identification, the actual sensitivity is much smaller than the $W\to\pi\gamma$ case. There is only one measurement currently of this decay mode, published by CDF (Abe *et al.*, 1998b) using Run 1B data.

Like the $W\to\pi\gamma$ rare decay, the $W\to D_s\gamma$ final state also contains a high-E_T photon, but instead of containing a single-track jet produced by the pion, it contains a collection of final states resulting from the decay of the D_s. Two decay modes of the D_s are utilized in this measurement: $D_s^{\pm}\to\phi\pi^{\pm}\to K^+K^-\pi^{\pm}$ and $D_s^{\pm}\to\overline{K^{*0}}K^{\pm}\to K^-\pi^+K^{\pm}$. These constitute about 4% of the D_s width.

The data selection follows the same path as for the $W\to\pi\gamma$ analysis, including trigger efficiency calculations. The photon selection criteria and their efficiencies are also shared with the $W\to\pi\gamma$ analysis. The identification of the D_s involves simple combinatoric mass fits, first reconstructing either the ϕ or $\overline{K^{*0}}$ and then the D_s using tracks with $p_T>1$ GeV. The p_T of the reconstructed intermediate state is required to be greater than 10 GeV, and the p_T of the D_s is required to be greater than 22 GeV (consistent with the photon). There are also D_s sideband fits, which are used for background determinations. The D_s should be isolated in much the same way as the pion was: there should be no other tracks with $p_T>1$ GeV in a cone of $\Delta R=0.7$ around the D_s. There are four D_s events left in the W pole region (3σ in this analysis is ± 7.9 GeV) and four D_s sideband events. The D_s signal events contain one ϕ channel and three $\overline{K^{*0}}$ channel events.

The D_s fitting efficiency is determined from a Monte Carlo simulation using a combination of PYTHIA and the Monte Carlo program of the CLEO Collaboration together with a full detector simulation. Track-finding efficiencies are determined by embedding simulated tracks in data and convoluting the measured efficiencies with the p_T spectrum from the Monte Carlo simulation. As with the $W\to\pi\gamma$ analysis, the track isolation efficiency is measured using the neutrino direction in the $W\to e\nu$ sample.

The net efficiency times acceptance is 0.069 ± 0.005, of which the dominant loss is again due to acceptance. Applying this to the four signal events or four background events results in a limit of $\sigma\cdot B(W\to D_s\gamma)\leq 27.4$ pb at 95% C.L. Expressed as the ratio of $\Gamma(W\to D_s\gamma)/\Gamma(W\to e\nu)$, this is $\leq 1.1\times 10^{-2}$. Figure 29 shows the signal

and sideband mass distributions together with the $W \rightarrow D_s\gamma$ simulation normalized to four signal events.

H. Trilinear gauge couplings

Trilinear W boson couplings are a direct consequence of the gauge invariance of the standard model due to the non-Abelian character of the $SU(2)_L$ isospin symmetry group. These couplings can be studied directly at the Tevatron in events with $W\gamma$, WW, and WZ diboson production. The presence of anomalous couplings manifests itself in an increase of the total diboson cross section, especially at large values of the diboson invariant mass. This can be understood because the trilinear couplings contribute via the s-channel diagram, whose effect is particularly strong in the central part of the detectors. Experimental limits on anomalous couplings are obtained by comparing the measured cross section or the shape of event kinematical distributions to the standard model and to the effective Lagrangian predictions for anomalous couplings. In the following we discuss the distributions that are expected to be more sensitive to the anomalous coupling parameters g_1^V, λ_V, and $\Delta\kappa_V$.

The next-to-leading-order cross sections for diboson production in $p\bar{p}$ colliders have been calculated for the $W\gamma X$ (Baur *et al.*, 1993; Ohnemus, 1993), the WWX (Ohnemus, 1991a; Baur *et al.*, 1996), and the WZX final state (Ohnemus, 1991b; Baur *et al.*, 1995). The SM predictions for $\sigma(WW)$ and $\sigma(WZ)$ are 9.5 and 2.5 pb, respectively. For the $W\gamma$ final state, the predictions are usually for the cross section times the branching fraction $B(W\rightarrow l\nu)$, integrated over the photon E_T spectrum above a minimum $E_T^{min}(\gamma)$, to avoid the divergence for $E_T^{min}(\gamma)\rightarrow 0$. At the Tevatron energies, next-to-leading-order corrections are responsible for an increase of $\approx$30% in the leading-order cross section but, to first degree, leave the shape of the event kinematic variables unchanged. Therefore, when studying these final states, it is customary to multiply distributions obtained from leading-order Monte Carlo generator samples by a K factor of $1+8/9\pi\alpha_s(M_W^2)\approx 1.34$. The situation is quite different at LHC energies, where the rapid increase with center-of-mass energy of the order-α_s corrections from the $qg\rightarrow W\gamma qX$ process, due to the rapid increase in gluon density, cannot be ignored. This results in both large next-to-leading-order correction to the cross section and large distortion of the shape of the kinematic variables most sensitive to anomalous couplings.

The standard model predicts that the $p\bar{p}\rightarrow W\gamma X$ process has vanishing amplitudes for $\cos\Theta=\pm 1/3$, where Θ is the angle between the scattered photon and the quark direction in the $W^{\mp}\gamma$ center-of-mass frame. This is known as the amplitude zero effect and would be partially eliminated by the presence of anomalous couplings. But because the longitudinal momentum of the neutrino is unknown, one cannot reconstruct $\cos\Theta$ directly in $p\bar{p}$ detectors. The Tevatron detectors have used, instead, another variable very sensitive to any deviation from SM predictions, the photon E_T spectrum. The average photon E_T increases considerably if anomalous couplings exist because their effects are enhanced at large parton center-of-mass energies. In general $WW\gamma$ studies have higher sensitivity to the λ_γ than to the $\Delta\kappa_\gamma$ coupling.

The $p\bar{p}\rightarrow WWX$ events are selected using leptonic decays of both or at least one W boson. The former are cleaner but suppressed by the additional $B(W\rightarrow l\nu)$ factor. The latter has larger background contamination from $W+2$ jet events and is practically impossible to distinguish from the WZ events where the Z decays hadronically. The dilepton p_T spectra and the W boson p_T distributions are most sensitive to trilinear couplings for the two classes of events. WW production has contributions from both $WW\gamma$ and WWZ vertices. To derive limits on the anomalous trilinear contributions, it is customary to assume some relations between the $WW\gamma$ and WWZ couplings so as to reduce the number of independent parameters. Common choices are (a) SM values for one set of parameters, (b) equal $WW\gamma$ and WWZ couplings, or (c) the HISZ relations (Hagiwara, Ishihara, Szalapski, and Zeppenfeld, 1993), which specify λ_Z, κ_Z, and g_1^Z in terms of the independent variables λ_γ and κ_γ. In general, one expects WW production to be considerably more sensitive to $\Delta\kappa_V$ than $p\bar{p}\rightarrow W\gamma X$ and $p\bar{p}\rightarrow WZX$ processes.

The $p\bar{p}\rightarrow WZX$ process is sensitive only to the WWZ vertex but suffers from a low cross section. It has been found that in the standard model, at tree level, WZ production exhibits an approximate amplitude zero (Baur *et al.*, 1995) similar in nature to the $W\gamma$ effect. As for the WW process, the effect of anomalous couplings is to increase the WZ cross section, especially at large values of the W or Z transverse momentum.

At the Tevatron, events with a $W\gamma$, WW, or WZ final state are isolated by requiring a leptonic decay of at least one of the massive bosons. Analyses have been performed in the following channels:

(1) $W\gamma\rightarrow l\nu\gamma$,
(2) $WW\rightarrow l\nu l\nu$,
(3) $WW/WZ\rightarrow l\nu jj$ and $WZ\rightarrow jjl^+l^-$,
(4) $WZ\rightarrow l\nu l^+l^-$,

where l stands for either e or μ.

1. $W\gamma\rightarrow l\nu\gamma$ analysis

The $p\bar{p}\rightarrow W\gamma X$ process has the largest diboson cross section but also an important background contribution from radiative W decays in which the charged lepton radiates a photon. In these events the photon and the lepton tend to be collinear, hence the need to cut on their angular separation $\Delta R_{l\gamma}>0.7$. The contribution from this background can be further reduced by a cut on the $W\gamma$ transverse mass, since in radiative decays the $l\nu$ pair and the photon form a system with transverse mass $m_T(l\nu\gamma)$ below the W mass, whereas for $W\gamma$ production the $m_T(l\nu\gamma)$ is larger than M_W. Possible contamination from the process $q_1q\rightarrow Wq_2$ with photon bremsstralung

TABLE X. Summary of the DØ and CDF analyses of $W\gamma \to l\nu\gamma$ events. The number of candidate $W\gamma$ events, N_{obs}, is shown together with the estimated background N_{bkg}, the number of signal events after background subtraction N_{sgn}, and the SM prediction N_{SM}.

	DØ		CDF	
	$e\nu\gamma$	$\mu\nu\gamma$	$e\nu\gamma$	$\mu\nu\gamma$
N_{obs}	57	70	75	34
N_{bkg}	15.2±2.5	27.7±4.7	16.1±3.5	10.3±1.6
N_{sgn}	41.8±8.2	42.3±9.0	58.9±9.4	10.3±6.0
N_{SM}	43.6±3.1	38.2±2.8	53.5±6.8	21.8±4.3
$E_T^{min}(\gamma)$	10 GeV		7 GeV	
$\sigma\times B(W\to l\nu)_{expt}$	11.3±2.2 pb		20.7±3.0 pb	
$\sigma\times B(W\to l\nu)_{SM}$	12.5±1.0 pb		18.6±2.8 pb	
$\int L$	92.8 pb^{-1}		67 pb^{-1}	

off the final-state quark can be efficiently suppressed by requiring the photon to be isolated (Ohnemus and Stirling, 1993).

The DØ results from the full Run 1 statistics (Abachi *et al.*, 1997a) are shown in Table X. The CDF Collaboration has published the cross-section measurement and limits on anomalous couplings based on Run 1A data (Abe *et al.*, 1995e). Table X shows preliminary results from Run 1B data (Benjamin, 1996).

The major source of background in $W\gamma \to l\nu\gamma$ events is neutral mesons misidentified as photons or genuine photon production in W+jet events. Both CDF and DØ estimate this contamination by measuring in an independent sample of multijet events the fraction of jets which pass the photon identification criteria. This probability $P(jet\to\gamma)$ decreases with the E_T of the photon and is of order 10^{-4} to 10^{-3} after correcting for the presence of prompt γ events in the jet sample. The prompt-photon contribution in multijets events is removed using cuts on the longitudinal and transverse profile of the calorimeter showers. Other backgrounds like $Z\gamma \to ll\gamma$ events in which one lepton is outside the detector fiducial region, or $W\gamma \to \tau\nu\gamma$ events are estimated using Monte Carlo calculations.

The cross section times the branching fraction $\sigma(W\gamma)\times B(W\to l\nu)$ measured by both experiments agrees well with the SM expectation, as seen in Table X. Figure 30 shows the combined DØ electron and muon $W\gamma$ sample.

Limits on the $WW\gamma$ anomalous coupling parameters are derived from a binned maximum-likelihood analysis of the observed photon E_T spectrum. The best results are obtained by the DØ Collaboration, which sets 95% C.L. limits for the individual coupling parameters at $-0.93<\Delta\kappa_\gamma<0.94$ ($\lambda_\gamma=0$) and $-0.31<\lambda_\gamma<0.29$ ($\Delta\kappa_\gamma=0$), assuming a form-factor scale $\Lambda=1.5$ TeV. These couplings have a simple physical interpretation in terms of the W magnetic dipole moment $\mu_W=e/2M_W(1+\kappa_\gamma+\lambda_\gamma)$ and electric quadrupole moment $Q_W^e=-(e/M_W^2)(\kappa_\gamma-\lambda_\gamma)$. Figure 31 shows the two-dimensional 95% C.L. limits in the (μ_W, Q_W^e) space. Also shown is the region of parameter space allowed by

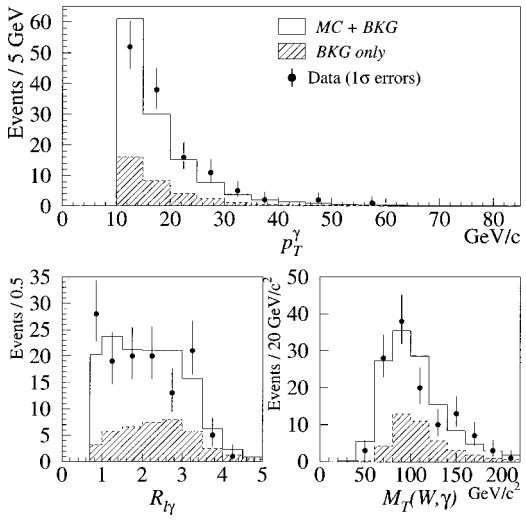

FIG. 30. Kinematic distributions from $W\gamma \to 1\nu\gamma$ production with standard-model Monte Carlo (MC) distributions and background (BKG) overlaid: top, photon E_T spectrum for DØ $W\gamma \leftarrow 1\nu\gamma$ events; bottom left, the lepton-photon angular separation; bottom right, the $W\gamma$ transverse mass distribution.

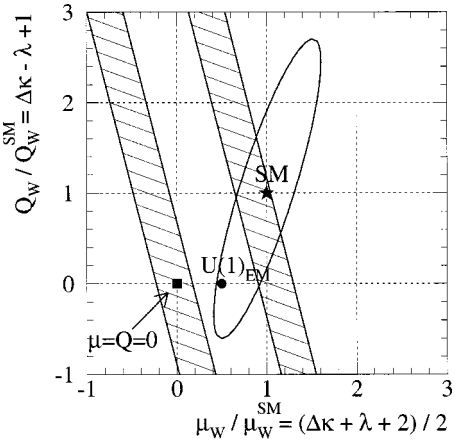

FIG. 31. DØ limits in terms of the W magnetic dipole (μ_W) and electric quadrupole (Q_W) moments, normalized to their standard-model values. The hatched regions are allowed from the CLEO $b\to s\gamma$ measurement. The point shows the minimal coupling value.

the $b \to s\gamma$ result of the CLEO Collaboration (Drell, 1997).

2. $WW \to l\nu l\nu$ analysis

One begins the analysis by identifying events with two isolated e^+e^- or $\mu^+\mu^-$ or $e^\pm\mu^\mp$ leptons and a minimum $\not\!\!E_T$ of 25 GeV. This stiff cut on the $\not\!\!E_T$ reduces both the $Z \to \tau\tau$ and the Drell-Yan ($\gamma/Z \to e^+e^-, \mu^+\mu^-$) backgrounds. Events are rejected if the invariant mass of the e^+e^- or $\mu^+\mu^-$ pair is in the range 75–105 GeV to remove any contamination from events containing a Z boson in the final state. The biggest remaining source of contamination is the $p\bar{p} \to t\bar{t} + X$ background, where the W from both top quarks decay leptonically. To remove it, CDF rejects events if they contain any jet with $p_T > 10$ GeV, while DØ requires that the hadronic energy in the calorimeter, $\vec{E}_T^{\,\mathrm{had}} = -(\vec{E}_T^{\,l_1} + \vec{E}_T^{\,l_2} + \vec{E}_T)$, be less than 40 GeV.

The CDF Collaboration has analyzed their full Run 1 data sample and found five candidates, two ee and three $e\mu$ (Abe *et al.*, 1997a). The estimated background is 1.2 ± 0.3 events, which gives $\sigma(p\bar{p} \to WW) = 10.2^{+6.3}_{-5.1}(\mathrm{stat}) \pm 1.6(\mathrm{syst})\mathrm{pb}$. The DØ Collaboration analysis also finds five events (two ee, one $\mu\mu$, and two $e\mu$) in Run 1 with 3.1 ± 0.4 events expected from background sources (Abachi *et al.*, 1995b; Abbott *et al.*, 1998b). This is in agreement with the SM expectation of 1.9 ± 0.1 events assuming a $\sigma(p\bar{p} \to WW)$ of 9.5 pb.

Limits on the WWW coupling parameters for CDF are obtained by comparing the total cross section to the Monte Carlo predictions. DØ performs a binned maximum-likelihood fit to the observed two-dimensional spectra of lepton p_T and obtains the following 95% C.L. limits, using a form-factor scale $\Lambda = 1.5$ TeV: $-0.62 < \Delta\kappa < 0.77$ (assuming $\lambda_\gamma = \lambda_Z = 0$) and $-0.52 < \lambda < 0.56$ (assuming $\Delta\kappa_\gamma = \Delta\kappa_Z = 0$).

3. $WW/WZ \to l\nu jj$ and $WZ \to jjl^+l^-$ analysis

Measurements of anomalous three-boson couplings in events in which a W decays leptonically and the second W or Z decays hadronically are a natural complement to the analysis presented in the previous section. The $WW/WZ \to l\nu jj$ final state benefits from a larger branching fraction and from a larger detector acceptance to jets. The backgrounds on the other hand are a challenge, expecially from $W + \geq 2$ jets events with $W \to l\nu$ and QCD multijet events where one of the jets is misidentified as an electron or is accompanied by a muon.

The CDF Collaboration has analyzed the Run 1A data (Abe *et al.*, 1995h) allowing for events in which the Z decays leptonically and the W hadronically. To keep the background under control, the analysis is restricted to the high-p_T boson region, where the sensitivity to anomalous coupling is maximal. The p_T^W cut is set high enough to limit the number of background events to less than one, in order to make background subtraction unnecessary. The candidate W or Z hadronic decay must have the two highest E_T jets with $E_T^J > 30$ GeV and a dijet invariant mass 60 GeV $< m(JJ) <$ 110 GeV. The p_T of the two-jet system must be $p_T(JJ) > 130$ GeV in W leptonic decays and $p_T(JJ) > 100$ GeV in Z leptonic decays. Using SM couplings, one predicts 0.13 $WW/WZ \to l\nu jj$ events with $N_{obs} = 0$ and 0.2 $WZ \to jjll$ events with $N_{obs} = 1$, consistent with no excess of events.

TABLE XI. Summary of the DØ analysis of $WW/WZ \to l\nu jj$ events, with $l = e, \mu$. See Table X for an explanation of the symbols.

	$e\nu jj$	$\mu\nu jj$
Backgrounds		
$W + \geq$ two jets	341.7 ± 38.3	105 ± 19
QCD multijets	116.5 ± 12.6	117 ± 24
$t\bar{t} \to l\nu jj$	4.6 ± 1.3	2.7 ± 1.2
N_{obs}	483	224
N_{bkg}	462.8 ± 40.3	224 ± 31
N_{SM}	20.7 ± 3.1	4.5 ± 0.8

The best Tevatron limits on anomalous WWV couplings using $WW/WZ \to l\nu jj$ events are obtained by DØ. The DØ analysis (Abachi *et al.*, 1997b; Abbott *et al.*, 1999g) makes use of the full Run 1 data sample and differs from the CDF analysis only in that it requires the presence of at least two jets with $E_T^J > 20$ GeV, for which the largest invariant-mass combination should be in the range $50\,\mathrm{GeV} < m(JJ) < 110\,\mathrm{GeV}$. No cut is applied on the p_T of the two jets; instead the limits on the couplings are obtained from a binned maximum-likelihood fit to the observed $p_T(l\nu)$ spectrum with the sum of the signal and background predicted by the Monte Carlo program. The total number of observed events is consistent with the SM prediction, as shown in Table XI. Assuming that the $WW\gamma$ and WWZ couplings are equal, DØ obtains $-0.47 < \Delta\kappa < 0.63$ ($\lambda = 0$) and $-0.36 < \lambda < 0.39$ ($\Delta\kappa = 0$) from $WW/WZ \to e\nu jj$ events, and $-0.62 < \Delta\kappa < 0.78$ ($\lambda = 0$) and $-0.45 < \lambda < 0.46$ ($\Delta\kappa = 0$) from $WW/WZ \to \mu\nu jj$ events. These limits are calculated with a form-factor scale $\Lambda = 1.5$ TeV and, while comparable for λ, are significantly better for the $\Delta\kappa$ parameter than the limits obtained from the $W\gamma \to l\nu\gamma$ analysis.

4. $WZ \to l\nu l^+l^-$ analysis

DØ has performed an analysis of WZ production in $p\bar{p} \to e\nu eeX$ and $p\bar{p} \to \mu\nu eeX$ events using a data sample corresponding to an integrated luminosity of approximately 90 pb^{-1} (Abbott *et al.*, 1999g). This very

TABLE XII. Summary of the DØ analysis of $WZ \to l\nu ee$ events with $l = e, \mu$. See Table X for an explanation of the symbols.

	$e\nu ee$	$\mu\nu ee$
N_{obs}	1	0
N_{bkg}	0.38 ± 0.14	0.12 ± 0.04
N_{SM}	0.10 ± 0.01	0.10 ± 0.01

unusual signature of three isolated high-p_T leptons and $\not{E}_T$ is expected to be background free, except for objects misidentified as leptons, like Z+jet events, where $Z \rightarrow ee$ and the jet mimics an electron or produces a muon. But very few events are expected, given the low WZ production cross section and the high branching-ratio suppression.

Data-based methods are used to estimate such backgrounds and give the results reported in Table XII. For standard-model WZ production the efficiencies are found to be $(16.9 \pm 1.4)\%$ and $(11.5 \pm 1.4)\%$ for the $evee$ and $\mu\nu ee$ channels, respectively. A 95% C.L. upper limit of 47 pb on the WZ cross section is estimated based on the only observed event in the $e\nu ee$ final state. A log-likelihood method is used to derive limits on the couplings once the probability of observing one event is determined. The value of the form factor Λ is chosen to ensure that the anomalous coupling limit is less than the unitarity limit. This analysis is most sensitive to λ_Z and Δg_1^Z. Setting $\Lambda = 1$ TeV, the one-dimensional 95% C.L. limits from $WZ \rightarrow l\nu ee$ events are $|\Delta g_1^Z| < 1.63$ ($\lambda_Z = 0$, $\Delta\kappa_Z = 0$) and $|\lambda_Z| < 1.42$ ($\lambda_Z = 0$, $\Delta\kappa_Z = 0$).

CDF has reported evidence of a $WZ \rightarrow e\nu ee$ candidate but no limits have been derived from this event (Nodulman, 1996).

5. DØ combined *WWV* analysis

DØ has performed a simultaneous fit to the most sensitive distributions for anomalous WWV couplings (Abbott *et al.*, 1998b, 1999g), thus obtaining the most stringent Tevatron limits on the λ and $\Delta\kappa$ parameters. The distributions used are the $p_T(\gamma)$ spectrum in $W\gamma$ events, the $p_T(l_1)$ and $p_T(l_2)$ of the two leptons in $WW \rightarrow l\nu l\nu$ events, the $p_T(l\nu)$ of the W boson in $WW/WZ \rightarrow l\nu jj$ events, and the observed number of events in $WZ \rightarrow l\nu e^+e^-$ searches. Assuming equal $WW\gamma$ and WWZ couplings and a form-factor scale of $\Lambda = 2$ TeV, the following limits are obtained:

$$-0.25 < \Delta\kappa < 0.39 \quad (\lambda = 0)$$

$$-0.18 < \lambda < 0.19 \quad (\Delta\kappa = 0). \tag{26}$$

The 95% C.L. one-dimensional and two-dimensional contour limits for other relations between $WW\gamma$ and WWZ coupling parameters are shown in Fig. 32.

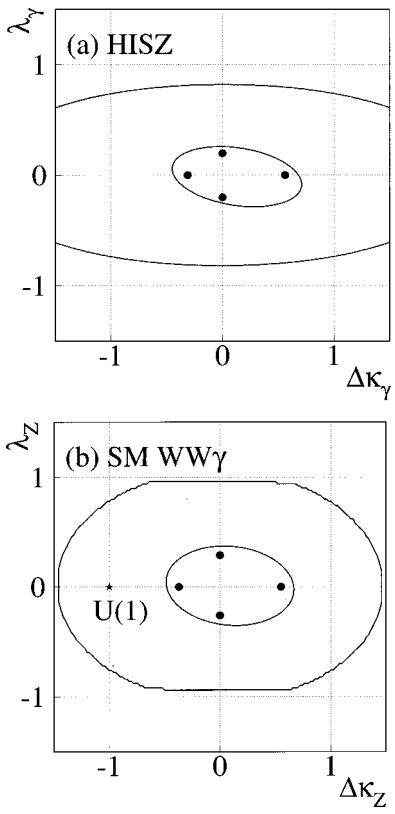

FIG. 32. Contour limits on anomalous couplings for $\Lambda = 1.5$ TeV and $\Delta g_1^Z = 0$ from the simultaneous fit to the DØ data: (a) HISZ (Hagiwara *et al.*, 1993) scenario; (b) assuming standard-model values for $WW\gamma$ parameters. The solid circles are the 95% C.L. limits from the one-dimensional fit. The inner and outer curves (where shown) are the 95% C.L. limits for the two-dimensional analysis and the unitarity constraint, respectively.

VI. FUTURE PROSPECTS

The last decade has seen an impressive number of measurements of W production and decay properties, both from Run 1 at the Tevatron and from the LEP II program. In the next ten years two proton machines, the Tevatron Collider at Fermilab and the Large Hadron Collider (LHC) at CERN, are expected to collect even larger samples of W bosons. The former is expected to start its $p\bar{p}$ Run 2 program in March 2001 with a stated goal of 2 fb^{-1} at $\sqrt{s} = 2$ TeV. The latter is expected to commence data-taking around 2005.

The main upgrades to the Tevatron are the addition of the Main Injector and the Recycler Ring (Montgomery, 1999). The main injector is a proton synchrotron with a circumference half that of the Tevatron. It was designed to deliver high-intensity $p\bar{p}$ beams to the Tevatron, thus significantly enhancing the Tevatron luminosity. The Recycler Ring is an 8-GeV permanent magnet ring equipped with stochastic cooling. Its main purpose is to store newly produced and unspent antiprotons between Tevatron runs, thus effectively doubling the number of antiprotons available for collisions. Both upgrades are presently being commissioned and, following a commissioning run with real collisions in Fall 2000, the Tevatron physics run is expected to start in Spring 2001.

Two sets of operating conditions are considered for Run 2 of the Tevatron: 36 bunches crossing every 396 ns or 108 bunches crossing every 132 ns with typical delivered luminosities of 1 and 2×10^{32} cm^{-2} s^{-1}, respectively. The expected average number of overlapping interactions in a given beam crossing will be $\bar{N} = 3$ and $\bar{N} = 2$, respectively. This ''classic'' Run 2A scenario will be compared to a ''stretched'' Run 2, or Run 2B scenario (Amidei *et al.*, 1996), with luminosities of at least 2×10^{32} cm^{-2} s^{-1} giving $\int L = 10$ fb^{-1} by the year 2005.

TABLE XIII. Expected W event yields for CDF II with 2 fb^{-1} of data: events when Run 1B detector configuration is assumed (column II), improvement factors when the increase in cross section (column III) and the increased acceptance (last column) are taken into account. For $W\gamma$, the cuts are $E_T^\gamma > 10$ GeV and $|\eta^\gamma| < 1$.

Channel	Events	$\sigma_{2.0\text{ TeV}}/\sigma_{1.8\text{ TeV}}$	$A_{\|\eta\|<2.0}/A_{\|\eta\|<1.0}$
$W\to e\nu$	1.4×10^6	1.12	2.0
$W\to \mu\nu$	6.5×10^5	1.12	2.6
$W\gamma$	1.5×10^3	1.13	1.5
$WW\to l\nu l\nu$	77	1.17	2.1
$WZ\to l\nu ll$	10	1.22	4.4

Both the CDF and DØ Collaborations have extensively upgraded their detectors to fully exploit the discovery reach of the Tevatron in this new regime of ''precision'' hadron collider physics.

The CDF II detector (CDF Collaboration, 1996) will have a completely redesigned tracking system based on a seven-layer silicon inner tracker covering the azimuthal region $|\eta|<2.0$ and an open-cell drift chamber extending to $|\eta|<1.0$, along with a new scintillator-based time-of-flight detector. Outside the solenoid, the original calorimeter and muon chambers surrounding the barrel region ($|\eta|<1.0$) will be complemented by a new plug calorimeter extending up to $|\eta|=3.6$ and an enhanced central and forward muon system able to provide almost full polar-angle coverage for $|\eta|<2.0$.

The DØ Run 2 detector (DØ Collaboration, 1996) will have an inner magnetic spectrometer, based on a silicon vertex detector surrounded by a 32-layer scintillating fiber tracker, which together will ensure tracking coverage up to $|\eta|=3.0$. These detectors are immersed in a 2-T magnetic field provided by a new superconducting solenoid. New scintillator-based central and forward preshower detectors will aid electron identification and triggering for $|\eta|<2.5$. The existing central muon chambers will have a new faster readout. The forward muons will be identified with a new plastic mini-drift-tube detector with pixel readout covering the region $1.0<|\eta|<2.0$. Due to the faster bunch crossing and higher data rates, CDF and DØ completely redesigned the trigger, front-end electronics, and data acquisition system.

The LHC will collide protons against protons every 25 ns at energies of $\sqrt{s}=14$ TeV with an initial ''low''-luminosity run at $10^{33}\,\text{cm}^{-2}\,\text{s}^{-1}$, yielding $\int L=10\,\text{fb}^{-1}$ per year, followed by a high-luminosity run at $10^{34}\,\text{cm}^{-2}\,\text{s}^{-1}$ or higher, with $\int L=100\,\text{fb}^{-1}$ per year. The latter configuration will produce $\bar{N}\sim20$ for a total of $\sim$2000 particles per crossing. Two general-purpose experimental apparatuses are being constructed, ATLAS (ATLAS Collaboration, 1994) and CMS (CMS Collaboration, 1994), which will probe the laws of fundamental interactions at effective energies of 1 TeV or higher.

In the following we report on the expectations for the Tevatron in the Main Injector era versus LEP II results and LHC sensitivities for W mass and width measurements, W charge asymmetry and QCD studies, rare decays and heavy charged-boson searches, and anomalous couplings. To set the scale of the discussion, Table XIII gives the expected yield of W and diboson events at the Tevatron for CDF II assuming an integrated luminosity of 2 fb^{-1} and the Run 1B detector configuration. Also shown are the expected improvements in statistics coming from the increase in cross section and in acceptance.

A. *W* mass and width

The CDF/DØ Run 1 preliminary combined measurement (see Fig. 16) gives $M_W^{Tevatron}=80.454\pm0.062$ GeV, where the systematic error is dominated by uncertainties in the lepton energy scale and track momentum response and resolution, and in the modeling of the recoil and W production. Uncertainties due to parton distribution functions and QED radiative corrections amount to about 20 MeV and are common to both Tevatron measurements. The LEP II average mass determination is $M_W^{LEP\text{-}II}=80.401\pm0.048$ GeV (LEP WW Working Group, 2000). The projected LEP II precision is $\Delta M_W \leqslant 40$ MeV. The largest systematic uncertainty in the W mass measurement at LEP II is due to Bose-Einstein and color reconnection effects.

The predicted W mass precision for each Tevatron experiment, with an integrated luminosity of 1(10) fb^{-1}, is around 50(30) MeV per channel. In estimating the ΔM_W achievable at the Tevatron Run 2 one should distinguish between systematic errors from measurements that are obtained from control data samples, expected to decrease as $1/\sqrt{N}$, and systematic errors from theoretical uncertainties. In the first group are uncertainties coming from the lepton and recoil energy/momentum scales and resolutions and backgrounds. In the second group are uncertainties coming from the W production and decay model, radiative corrections, and parton distribution functions. These uncertainties should be substantially reduced by the combination of new theoretical calculations and experimental results like the boson p_T measurements and the parton distribution function constraints from W charge asymmetry measurements. A Tevatron Run 2A measurement with 25-MeV precision should be within reach.

It is worth noting that the presence of multiple interactions degrades the recoil energy resolution, and therefore the W transverse mass resolution, by a factor proportional to $\sqrt{\bar{N}}$. Thus the precision of the transverse mass fit does not improve as $1/\sqrt{N}$ when larger data samples are obtained by increasing the luminosity per bunch. The charged-lepton p_T fit, which is much less sensitive to multiple interactions, will become the most precise technique at very high luminosity. All fitting techniques will likely be used to check for consistency and to obtain a combined final result. Alternate methods using the ratio of the lepton p_T distributions from the W and the Z scaled for the different boson masses (Giele and Keller, 1996), or the ratio of the W and Z transverse masses (Rajagopalan and Rijssenbeek, 1996) have also been proposed for measuring the W mass with high luminosity.

Within the SM, $\Delta M_W \sim 25\,\mathrm{MeV}$ corresponds to $\Delta m_H/m_H \sim 40\%$, assuming all other inputs are precisely known. In this context, the current uncertainty of 5 GeV on the top-quark mass is equivalent to $\Delta M_W \sim 30\,\mathrm{MeV}$. Thus it is important to improve the top mass precision also in Run 2. With an expected precision of 2.0 GeV, the top mass uncertainty will not limit the Higgs mass constraint. The running electromagnetic coupling constant $\alpha(M_Z)$ causes an uncertainty equivalent to $\Delta M_W \sim 15\,\mathrm{MeV}$, due to the uncertainty in the hadronic contribution to its evolution. This is expected to decrease with new measurements from the BES Collaboration.

At present, the value of the Higgs mass that best fits all of the electroweak measurements performed by LEP, SLAC, and Tevatron experiments is $m_H^{SM} = 77^{+69}_{-39}\,\mathrm{GeV}$ (LEP Collaborations, 2000a),[5] i.e., m_H is currently constrained to within a factor of 2. After the Tevatron Run 2A, m_H should be constrained to within 50% (see Fig. 17).

The precise measurement of the *W* mass at the LHC presents some real challenges. Even at "low" luminosities, about 6×10^7 *W* events are expected per year, making the statistical uncertainties completely negligible. The dominant systematic uncertainty, coming from the knowledge of the lepton energy scale, will limit the overall precision to 15 MeV with the assumption that the lepton energy and momentum scales can be understood at the 0.02% level (ATLAS Collaboration, 1999).

The direct measurements of the *W* width from the tail of the m_T^W distribution, and its indirect extraction from the cross-section ratio $R = \sigma_W \cdot B(W \to l\nu)/\sigma_W \cdot B(Z \to l^+ l^-)$, provide an important SM consistency check. The Tevatron direct measurement of the *W* width is $\Gamma_W = 2.04 \pm 0.14\,\mathrm{GeV}$, to be compared with the combined LEP II measurement of $\Gamma_W = 2.19 \pm 0.15\,\mathrm{GeV}$ (LEP WW Working Group, 2000). With the statistics of the current Tevatron data samples, the indirect determination of the total *W* width from the partial leptonic cross sections (see Sec. V.C) is systematics dominated and significantly more precise than the direct measurement from the high-m_T tail of the m_T distribution. However, the latter makes fewer model-dependent assumptions and is likely to improve more rapidly with higher statistics because the precision on Γ_W from R will be limited by the theoretical error on the σ_W/σ_Z production cross-section ratio, currently around 1%. The projected Run 2 precision on the *W* width per experiment at the Tevatron, assuming integrated luminosities of 1(10) fb^{-1}, is 48(20) MeV from the *W* transverse mass fit in the $W \to e\nu$ channel alone. Combining the electron and muon channels for both experiments, a final overall precision of 10 MeV should be within reach.

B. *W* charge asymmetry and QCD studies

As discussed in Sec. V.D, the measurement of the *W* charge asymmetry provides a very powerful tool for discriminating among different sets of parton distribution functions at hadron collider experiments. The sensitivity to the parton distribution functions is greater in the region of $|\eta| > 2.0$. Therefore the improved rapidity coverage for tracking, calorimetry, and muon detection in both CDF II and DØ upgrades will be very important for making the best use of the discriminating power of the *W* charge asymmetry. The precision of the measurements is expected to be dominated by statistics for integrated luminosities up to 2 fb^{-1}.

The improved η coverage for jet reconstruction, together with the increased statistics available in Run 2, should also provide enough sensitivity to events with up to six jets produced in association with the *W* boson (see Fig. 24). As most of the inputs are determined from the data, we expect the p_T^W measurements to become more precise with larger data samples.

C. Rare *W* decays and heavy *W′* bosons

With the number of *W* decays produced with 10 fb^{-1}, one should be able to greatly improve the present Tevatron limits on $W \to \pi\gamma$ and $W \to D_s\gamma$ (see Sec. V.G) even though they will still be two orders of magnitude away from the branching ratios predicted by the SM. Their direct observation will also be out of reach at the high-luminosity LHC.

Helicity-independent searches for heavy charged-boson decays $W' \to l\nu$ at the Tevatron yielded the best Run 1 limit of $M_{W'} > 720\,\mathrm{GeV}$ at 95% C.L. assuming light, noninteracting, stable neutrinos and the suppression of the $W' \to WZ$ channel (see Sec. V.F.1). The limit is projected to improve to 990 GeV for a Run 2 integrated luminosity of 2 fb^{-1}. At LHC the sensitivity to a possible W' signal is predicted to extend out to masses of about 6 TeV (ATLAS Collaboration, 1999).

D. Anomalous vector-boson couplings

A DØ simultaneous fit (Abbott *et al.*, 1999g) of the most sensitive distributions to anomalous WWV couplings has resulted in the 68% C.L. limits of $\lambda_\gamma = 0.00^{+0.10}_{-0.09}$ and $\Delta\kappa_\gamma = -0.08^{+0.34}_{-0.34}$ under the HISZ (Hagiwara *et al.*, 1993) assumptions for $\Lambda = 2$ TeV. For comparison the current preliminary LEP II one-dimensional limits are $\lambda_\gamma = -0.016^{+0.026}_{-0.026}$ and $\Delta\kappa_\gamma = 0.021^{+0.063}_{-0.059}$ (LEP Electroweak TGC Working Group, 2000) and are expected to reach a precision level of 0.02 and 0.05, respectively, by the end of the LEP II program.

Since the sensitivity to anomalous production is limited by backgrounds, the measurements of the cross sections (which depend on the square of the couplings) improve in precision as $1/\sqrt{N}$. For Run 2, the substantial increase in statistics should provide an improvement of order 3(5) over the present coupling limits for integrated luminosities of 1(10) fb^{-1}. At LHC, with 30 fb^{-1} of data, one expects a precision level of 0.003 for λ_γ and 0.04 for $\Delta\kappa_\gamma$ for $\Lambda = 10\,\mathrm{TeV}$ (ATLAS Collaboration, 1999).

[5] This corresponds to $m_H < 215\,\mathrm{GeV}$ at 95% C.L. Limits from direct searches at LEP yield $m_H > 107.9\,\mathrm{GeV}$ at 95% C.L. (LEP Collaborations, 2000b).

The improved rapidity coverage for the Run 2 Tevatron detectors is also expected to improve the sensitivity to the amplitude zero effect in $p\bar{p} \to W\gamma$ production. Simulation studies indicate that with 1 fb^{-1} of data one should be able to establish the presence of a dip if both central and plug leptons can be used. It should be noted that the Tevatron might offer the only realistic chance of proving this SM prediction because the sensitivity to the amplitude zero effect at LHC is substantially reduced by large QCD corrections, such as W production by $qg \to Wq'$.

VII. CONCLUSIONS

The production of high-statistics W samples at the Tevatron has resulted in precision measurements of the properties of the W boson. The current world average of the direct measurements of the W mass is $M_W = 80.420 \pm 0.038$ GeV, corresponding to a precision of 0.05%. The measurements of the W width, the production cross section, and the event kinematics are consistent with the SM prediction. A precise measurement of the W charge asymmetry has provided an additional handle on reducing the W mass uncertainty as well as challenging the theory to devise a more accurate description of the data with new sets of parton distribution functions. New limits have been set for the branching ratio into rare decay modes and the masses of a heavy W' and right-handed W boson. Studies of trilinear gauge boson couplings have shown that the production of $W\gamma$, WW, and WZ events is in agreement with the prediction of the SM, within the experimental sensitivity.

The upgraded Tevatron and the DØ and CDF detectors will begin running in the year 2001, followed by the LHC, ATLAS, and CMS detectors within this decade. Improvements in the precision measurements of W properties, coupled with improved measurement of the top-quark mass, will yield predictions for the Higgs mass and provide crucial tests of the self-consistency of the SM.

ACKNOWLEDGMENTS

We wish to thank our CDF and DØ colleagues for producing such fruitful results over the last decade. We also wish to express our thanks to F. Bedeschi, M. Campbell, and A. Goshaw for encouraging us to write this review. We thank W. Carithers, T. Diehl, J. Ellison, P. Grannis, U. Heintz, H. Montgomery, L. Nodulman, and M. Strovink for useful discussions, and W. Ashmanskas, J. Dittman, J. Ellison, C. Gerber, Y. Kim, and W. Robertson for their assistance with the figures.

REFERENCES

Abachi, S., *et al.*, 1994, Nucl. Instrum. Methods Phys. Res. A **338**, 185.
Abachi, S., *et al.*, 1995a, Phys. Lett. B **358**, 405.
Abachi, S., *et al.*, 1995b, Phys. Rev. Lett. **75**, 1023.
Abachi, S., *et al.*, 1995c, Phys. Rev. Lett. **75**, 1456.
Abachi, S., *et al.*, 1995d, Phys. Rev. Lett. **75**, 3226.
Abachi, S., *et al.*, 1996a, Phys. Rev. Lett. **76**, 3271.
Abachi, S., *et al.*, 1996b, Phys. Rev. Lett. **77**, 3309.
Abachi, S., *et al.*, 1997a, Phys. Rev. Lett. **78**, 3634.
Abachi, S., *et al.*, 1997b, Phys. Rev. Lett. **79**, 1441.
Abbott, B., *et al.*, 1998a, Phys. Rev. D **58**, 012002.
Abbott, B., *et al.*, 1998b, Phys. Rev. D **58**, 051101.
Abbott, B., *et al.*, 1998c, Phys. Rev. D **58**, 092003.
Abbott, B., *et al.*, 1998d, Phys. Rev. Lett. **80**, 3008.
Abbott, B., *et al.*, 1998e, Phys. Rev. Lett. **80**, 5498.
Abbott, B., *et al.*, 1999a, FERMILAB-CONF-99/201-E, hep-ex/9907022.
Abbott, B., *et al.*, 1999b, FERMILAB-PUB-99/237-E, Phys. Rev. D (in press).
Abbott, B., *et al.*, 1999c, Nucl. Instrum. Methods Phys. Res. A **424**, 352.
Abbott, B., *et al.*, 1999d, Phys. Lett. B **464**, 145.
Abbott, B., *et al.*, 1999e, Phys. Rev. D **60**, 052001.
Abbott, B., *et al.*, 1999f, Phys. Rev. D **60**, 052003.
Abbott, B., *et al.*, 1999g, Phys. Rev. D **60**, 072002.
Abbott, B., *et al.*, 2000a, Phys. Rev. D **61**, 032004.
Abbott, B., *et al.*, 2000b, Phys. Rev. D **61**, 072001.
Abbott, B., *et al.*, 2000c, Phys. Rev. Lett. **84**, 222.
Abbott, B., *et al.*, 2000d, Phys. Rev. Lett. **84**, 2792.
Abbott, B., *et al.*, 2000e, Phys. Rev. Lett. **84**, 5710.
Abe, F., *et al.*, 1988, Nucl. Instrum. Methods Phys. Res. A **271**, 387.
Abe, F., *et al.*, 1989, Phys. Rev. Lett. **62**, 1005.
Abe, F., *et al.*, 1990a, Phys. Rev. D **41**, 2330.
Abe, F., *et al.*, 1990b, Phys. Rev. Lett. **65**, 2243.
Abe, F., *et al.*, 1991a, Phys. Rev. D **43**, 2070.
Abe, F., *et al.*, 1991b, Phys. Rev. Lett. **66**, 2951.
Abe, F., *et al.*, 1991c, Phys. Rev. Lett. **67**, 2609.
Abe, F., *et al.*, 1992a, Phys. Rev. Lett. **68**, 1458.
Abe, F., *et al.*, 1992b, Phys. Rev. Lett. **68**, 3398.
Abe, F., *et al.*, 1992c, Phys. Rev. Lett. **69**, 2160.
Abe, F., *et al.*, 1993, Phys. Rev. D **47**, 4857.
Abe, F., *et al.*, 1994, Phys. Rev. Lett. **73**, 2296.
Abe, F., *et al.*, 1995a, Phys. Rev. D **52**, 2624.
Abe, F., *et al.*, 1995b, Phys. Rev. D **52**, 4784.
Abe, F., *et al.*, 1995c, Phys. Rev. Lett. **74**, 341.
Abe, F., *et al.*, 1995d, Phys. Rev. Lett. **74**, 850.
Abe, F., *et al.*, 1995e, Phys. Rev. Lett. **74**, 1936.
Abe, F., *et al.*, 1995f, Phys. Rev. Lett. **74**, 2900.
Abe, F., *et al.*, 1995g, Phys. Rev. Lett. **75**, 11.
Abe, F., *et al.*, 1995h, Phys. Rev. Lett. **75**, 1017.
Abe, F., *et al.*, 1996a, Phys. Rev. Lett. **76**, 2852.
Abe, F., *et al.*, 1996b, Phys. Rev. Lett. **76**, 3070.
Abe, F., *et al.*, 1997a, Phys. Rev. Lett. **78**, 4536.
Abe, F., *et al.*, 1997b, Phys. Rev. Lett. **79**, 4760.
Abe, F., *et al.*, 1998a, Phys. Rev. D **58**, 031101.
Abe, F., *et al.*, 1998b, Phys. Rev. D **58**, 091101.
Abe, F., *et al.*, 1998c, Phys. Rev. Lett. **81**, 5754.
Abe, F., *et al.*, 1999a, FERMILAB-PUB-99/249-E.
Abe, F., *et al.*, 1999b, Phys. Rev. D **59**, 092001.
Abe, F., *et al.*, 1999c, Phys. Rev. D **59**, 052002.
Abe, F., *et al.*, 1999d, Phys. Rev. Lett. **82**, 271.
Affolder, T., *et al.*, 2000a, FERMILAB-PUB-00/085-E, Phys. Rev. Lett., in press.
Affolder, T., *et al.*, 2000b, FERMILAB-PUB-00/158-E, Phys. Rev. D, in press.
Affolder, T., *et al.*, 2000c, Phys. Rev. Lett. **84**, 845.
Albajar, C., *et al.*, 1987, Phys. Lett. B **185**, 233.

Albajar, C., *et al.*, 1989, Z. Phys. C **44**, 15.
Albajar, C., *et al.*, 1990, Phys. Lett. B **241**, 283.
Albajar, C., *et al.*, 1991, Phys. Lett. B **253**, 503.
Alitti, J., *et al.*, 1990, Phys. Lett. B **241**, 150.
Alitti, J., *et al.*, 1991, Z. Phys. C **49**, 17.
Alitti, J., *et al.*, 1992a, Phys. Lett. B **276**, 354.
Alitti, J., *et al.*, 1992b, Phys. Lett. B **276**, 365.
Alitti, J., *et al.*, 1992c, Phys. Lett. B **277**, 203.
Alitti, J., *et al.*, 1992d, Phys. Lett. B **280**, 137.
Alitti, J., *et al.*, 1993, Nucl. Phys. B **400**, 3.
Altarelli, G., and G. Parisi, 1977, Nucl. Phys. B **126**, 298.
Altarelli, G., R. K. Ellis, M. Greco, and G. Martinelli, 1984, Nucl. Phys. B **246**, 12.
Amidei, D., *et al.*, 1996, "Report of the Tev-2000 Study Group," FNAL-Pub-96/082.
Ansari, R., *et al.*, 1987a, Phys. Lett. B **186**, 440.
Ansari, R., *et al.*, 1987b, Phys. Lett. B **186**, 452.
Appel, J., *et al.*, 1986, Z. Phys. C **30**, 1.
Arnellos, L., W. Marciano, and Z. Parsa, 1982, Nucl. Phys. B **196**, 378.
Arneodo, M., *et al.*, 1997, Nucl. Phys. B **487**, 3.
Arnison, G., *et al.*, 1983a, Phys. Lett. **122B**, 103.
Arnison, G., *et al.*, 1983b, Phys. Lett. **126B**, 398.
Arnison, G., *et al.*, 1985, Nuovo Cimento **44**, 1.
Arnison, G., *et al.*, 1986, Phys. Lett. **166B**, 484.
Arnold, P., and M. Reno, 1989, Nucl. Phys. B **319**, 37.
ATLAS Collaboration, 1994, "ATLAS Technical Proposal," CERN/LHCC/94-43.
ATLAS Collaboration, 1999, "ATLAS: Detector and Physics Performance Technical Design Report," CERN/LHCC/94-14 (Vol. I); CERN/LHCC/99-15 (Vol. II).
Bagnaia, P., *et al.*, 1983, Phys. Lett. **129B**, 130.
Balazs, C., and C. Yuan, 1997, Phys. Rev. D **56**, 5558.
Banner, M., *et al.*, 1983, Phys. Lett. **122B**, 476.
Barberio, E., and Z. Was, 1994, Comput. Phys. Commun. **79**, 291.
Barbieri, R., and R. N. Mohapatra, 1989, Phys. Rev. D **39**, 1229.
Baur, U., and E. Berger, 1990, Phys. Rev. D **41**, 1476.
Baur, U., T. Han, and J. Ohnemus, 1993, Phys. Rev. D **48**, 5140.
Baur, U., T. Han, and J. Ohnemus, 1995, Phys. Rev. D **51**, 3381.
Baur, U., T. Han, and J. Ohnemus, 1996, Phys. Rev. D **53**, 1098.
Baur, U., S. Keller, and D. Wackeroth, 1999, Phys. Rev. D **59**, 013002.
Benjamin, D., 1996, in *$W\gamma$ and $Z\gamma$ Production at the Tevatron*, edited by R. Raja and J. Yoh, AIP Conf. Proc. No. 357 (AIP, Melville, NY), p. 370.
Berends, F., and R. Kleiss, 1985, Z. Phys. C **27**, 365.
Berends, F. A., H. Kuijf, B. Taksk, and W. T. Giele, 1991, Nucl. Phys. B **357**, 32.
Berger, E. L., F. Halzen, C. S. Kim, and S. Willenbrock, 1989, Phys. Rev. D **40**, 83; **40**, 3789(E).
Brun, R., *et al.*, 1978, CERN-DD-78-2-Rev.
CDF Collaboration, 1996, "CDF II Detector Technical Design Report," FNAL-Pub-96/390-E.
Chankowski, P., A. Dabelstein, W. Hollik, W. M. Mosle, S. Pokorski, and J. Rosiek, 1994, Nucl. Phys. B **417**, 101.
CMS Collaboration, 1994, "CMS Technical Proposal," CERN/LHCC/94-38.
Collins, J., and D. Soper, 1981, Nucl. Phys. B **193**, 381.
Collins, J., D. Soper, and G. Sterman, 1985, Nucl. Phys. B **250**, 199.
DØ Collaboration, 1996, "The DØ Upgrade—The Detector and Its Physics," FNAL-Pub-96/357-E.
Dabelstein, A., W. Hollik, and W. Mosle, 1995, in *Perspective for Electroweak Interactions in e^+e^- Collisions*, edited by B. Kniehl (World Scientific, Singapore), p. 345.
Degrassi, G., P. Gambino, and A. Sirlin, 1997, Phys. Lett. B **394**, 188.
Degrassi, G., P. Gambino, M. Passera, and A. Sirlin, 1998, Phys. Lett. B **418**, 209.
Drell, P., 1997, in *Lepton-Photon Interaction*: LP97 Proceedings, edited by A. De Roech and A. Wagner (World Scientific, Singapore), p. 347.
Drell, S., and T. Yan, 1970, Phys. Rev. Lett. **25**, 316.
Ellis, R., and S. Veseli, 1998, Nucl. Phys. B **511**, 649.
Ellison, J., and J. Wudka, 1998, Annu. Rev. Nucl. Sci. **48**, 33.
Garcia, D., and J. Sola, 1994, Mod. Phys. Lett. A **9**, 211.
Giele, W., E. Glover, and D. Kosower, 1993, Nucl. Phys. B **403**, 633.
Giele, W., and S. Keller, 1996, FERMILAB-CONF-96/307-T, hep-ph/9609382.
Giele, W., and S. Keller, 1998, Phys. Rev. D **57**, 4433.
Glashow, S., 1961, Nucl. Phys. **22**, 579.
Gonsalves, R. J., J. Pawlowski, and C.-F. Wai, 1990, Phys. Lett. B **252**, 663.
Grünewald, M. W., 1999, Phys. Rep. **322**, 125.
Hagiwara, K., S. Ishihara, R. Szalapski, and D. Zeppenfeld, 1993, Phys. Rev. D **48**, 2182.
Hasert, F. J., *et al.*, 1973, Phys. Lett. **46B**, 138.
Higgs, P. W., 1966, Phys. Rev. **145**, 1156.
Ladinsky, G., and C. Yuan, 1994, Phys. Rev. D **50**, 4239.
Lai, H., 1995, Phys. Rev. D **51**, 4763.
Lai, H., 1997, Phys. Rev. D **55**, 1280.
Langacker, P., 1989, Phys. Rev. D **40**, 1229.
LEP Collaborations, 2000a, LEP Electroweak Working Group, and SLD Heavy Flavour and Electroweak Group, CERN-EP-2000-016.
LEP Collaborations, 2000b, LEP Working Group for Higgs Boson Searches, CERN-EP-2000-055.
LEP Electroweak TGC Working Group, 2000, LEPEWWG/TGC/2000-01.
LEP WW Working Group, 2000, LEPEWWG/WW/00-01.
Llewellyn Smith, C., and J. Wheater, 1981, Phys. Lett. **105B**, 486.
Marchesini, G., and B. Webber, 1988, Nucl. Phys. B **310**, 461.
Marciano, W., and A. Sirlin, 1980, Phys. Rev. D **22**, 2695; **31**, 213(E).
Martin, A. D., R. G. Roberts, and W. J. Stirling, 1989, Mod. Phys. Lett. A **4**, 1135.
Martin, A. D., W. J. Stirling, and R. G. Roberts, 1993, Phys. Lett. B **306**, 145.
Martin, A. D., R. G. Roberts, and W. J. Stirling, 1996, Phys. Lett. B **387**, 419.
Martin, A. D., R. G. Roberts, W. J. Stirling, and R. S. Thorne, 1998, Eur. Phys. J. C **4**, 463.
Mirkes, E., 1992, Nucl. Phys. B **387**, 3.
Mohapatra, R., 1992, *Unification and Supersymmetry* (Springer-Verlag, New York).
Montgomery, H., 1999, "Physics with the Main Injector," FERMILAB-CONF-99-057.

Nodulman, L., 1996, in *Proceedings of International Conference on High Energy Physics '96*, Warsaw, Poland, edited by Z. Ajduk and A. K. Wroblewski (World Scientific, River Edge, NJ). Also available as Fermilab-conf-96/164-E.
Ohnemus, J., 1991a, Phys. Rev. D **44**, 1403.
Ohnemus, J., 1991b, Phys. Rev. D **44**, 3477.
Ohnemus, J., 1993, Phys. Rev. D **47**, 940.
Ohnemus, J., and W. Stirling, 1993, Phys. Lett. B **298**, 230.
Olive, K. A., D. N. Schramm, and G. Steigman, 1981, Nucl. Phys. B **180**, 497.
Paige, F., and S. Protopopescu, 1986, BNL Report, BNL38034.
Particle Data Group, 1998, Eur. Phys. J. C **3**, 1.
Pierce, D. M., J. A. Bagger, K. T. Matchev, and R.-J. Zhang, 1997, Nucl. Phys. B **491**, 3.
Raffelt, G., and D. Seckel, 1988, Phys. Rev. Lett. **60**, 1793.
Rajagopalan, S., and M. Rijssenbeek, 1996, in *Proceedings of the DPF/DPB Summer Study on New Directions for High-Energy Physics*, Snowmass, CO, Fermilab-Conf-96-452-E.
Ramond, P., 1983, Annu. Rev. Nucl. Sci. **33**, 31.
Salam, A., 1969, in *Elementary Particle Theory*, edited by N. Svartholm (Almquist and Wiksells, Stockholm), p. 467.
Sirlin, A., 1980, Phys. Rev. D **22**, 971.
Sjostrand, T., 1985, Phys. Lett. **157B**, 321.
Sjostrand, T., and M. van Zijl, 1987, Phys. Rev. D **36**, 2019.
't Hooft, G., 1971a, Nucl. Phys. B **33**, 173.
't Hooft, G., 1971b, Nucl. Phys. B **35**, 167.
Weinberg, S., 1967, Phys. Lett. **19**, 1264.
Yang, U., A. Bodek, and Q. Fan, 1998, preprint hep-ph/9806457.